



National Library
of Canada

Bibliothèque nationale
du Canada

Canadian Theses Service

Service des thèses canadiennes

Ottawa, Canada
K1A 0N4

NOTICE

The quality of this microform is heavily dependent upon the quality of the original thesis submitted for microfilming. Every effort has been made to ensure the highest quality of reproduction possible.

If pages are missing, contact the university which granted the degree.

Some pages may have indistinct print especially if the original pages were typed with a poor typewriter ribbon or if the university sent us an inferior photocopy.

Reproduction in full or in part of this microform is governed by the Canadian Copyright Act, R.S.C. 1970, c. C-30, and subsequent amendments.

AVIS

La qualité de cette microforme dépend grandement de la qualité de la thèse soumise au microfilmage. Nous avons tout fait pour assurer une qualité supérieure de reproduction.

S'il manque des pages, veuillez communiquer avec l'université qui a conféré le grade.

La qualité d'impression de certaines pages peut laisser à désirer, surtout si les pages originales ont été dactylographiées à l'aide d'un ruban usé ou si l'université nous a fait parvenir une photocopie de qualité inférieure.

La reproduction, même partielle, de cette microforme est soumise à la Loi canadienne sur le droit d'auteur, SRC 1970, c. C-30, et ses amendements subséquents.

Numerical Modelling of EC-130 Airframe
and Antenna Installation for
Prediction of Radiation Characteristics
Over the HF Band

Benita Randi Rosenzweig

A Thesis
in
The Department
of
Electrical Engineering

Presented in Partial Fulfillment of the Requirements
for the Degree of Master of Engineering at
Concordia University
Montreal, Quebec, Canada

March 1991

© Benita Randi Rosenzweig, 1991



National Library
of Canada

Bibliothèque nationale
du Canada

Canadian Theses Service Service des thèses canadiennes

Ottawa, Canada
K1A 0N4

The author has granted an irrevocable non-exclusive licence allowing the National Library of Canada to reproduce, loan, distribute or sell copies of his/her thesis by any means and in any form or format, making this thesis available to interested persons.

The author retains ownership of the copyright in his/her thesis. Neither the thesis nor substantial extracts from it may be printed or otherwise reproduced without his/her permission.

L'auteur a accordé une licence irrévocable et non exclusive permettant à la Bibliothèque nationale du Canada de reproduire, prêter, distribuer ou vendre des copies de sa thèse de quelque manière et sous quelque forme que ce soit pour mettre des exemplaires de cette thèse à la disposition des personnes intéressées.

L'auteur conserve la propriété du droit d'auteur qui protège sa thèse. Ni la thèse ni des extraits substantiels de celle-ci ne doivent être imprimés ou autrement reproduits sans son autorisation.

ISBN 0-315-64753-1

Canada

ABSTRACT

Numerical Modelling of EC130 Airframe and Antenna Installation for Prediction of Radiation Characteristics Over HF Band

Benita Randi Rosenzweig

The input impedance and radiation characteristics of HF antennas mounted on aircraft can be derived by theoretical-numerical techniques. The Numerical Electromagnetic Code utilizes the Moment Method with wire grid modelling to solve integral equations for the currents induced on a structure by a known incident field. The computed electromagnetic response of the HF antenna/airframe system is used to verify and complete experimental measurements.

The EC130 HF antenna installation consists of five external wire antennas extending along the upper portion of the fuselage and terminating at various points near the vertical stabilizer. Antenna radiation patterns have been measured on a scale model of the EC130 aircraft. In addition, the Naval Air Test Center had conducted full scale airborne testing of the HF antenna complement. Discrepancies between the full scale and scale model measurements led to the development of a computer model. Several wire grid model configurations were developed to qualify the experimental data.

ACKNOWLEDGEMENTS

I wish to express my sincerest thanks to Dr. S.J. Kubina for his guidance and encouragement throughout my years at the Electromagnetic Compatibility Laboratory of Concordia University. The knowledge and practical approach to problem solving that he passed on will serve me well in the future.

I wish to thank the Naval Air Test Centre for funding the research described in this thesis. A special thanks to Mr. Denis DeCarlo of the NATC for his clear and immediate responses to all queries concerning this project.

I want to express my gratitude to Dr. C.W. Trueman for his direction through the theoretical intricacies of electromagnetics. Many thanks to Mr. Mike Marak and Mr. David Gaudine for maintaining a 'well oiled machine' thereby smoothing the thesis process.

Finally, I wish to express my deepest gratitude to my family, whose confidence in my ability enabled me to complete a task of this magnitude. A special thanks to my Mother, who patiently listened to every detail of this work and enthusiastically encouraged my academic pursuits.

TABLE OF CONTENTS

| | PAGE |
|---|------|
| GLOSSARY OF TERMS..... | viii |
| CHAPTER 1 INTRODUCTION..... | 1 |
| 1.1 Full Scale Measurements..... | 2 |
| 1.2 Scale Model Measurements..... | 3 |
| 1.3 Numerical Model..... | 5 |
| 1.4 Validation..... | 6 |
| 1.5 Objective..... | 7 |
| CHAPTER 2 Numerical Electromagnetics Code (NEC)..... | 9 |
| 2.1 NEC Input Format..... | 9 |
| 2.2 Pocklington's Integral Equation. | 13 |
| 2.2.1 Thin Wire Analysis..... | 15 |
| 2.2.2 Extended Thin Wire Kernel | 18 |
| 2.2.3 Boundary Conditions..... | 21 |
| 2.3 Method of Moments..... | 23 |
| 2.4 Current Expansion on Wires..... | 24 |
| 2.4.1 Free End..... | 26 |
| 2.4.2 Junction..... | 26 |
| 2.5 Calculation of Structure Matrix. | 31 |
| 2.6 Far Field Calculations..... | 33 |
| 2.7 The Effect of a Ground Plane.... | 36 |
| 2.8 NEC Solution File..... | 38 |
| CHAPTER 3 WIRE GRID MODEL DEVELOPMENT..... | 39 |
| 3.1 Modelling Guidelines..... | 39 |

| | | | |
|---------|---------|---|-----|
| | 3.2 | Software Modules for Model Development..... | 44 |
| | 3.2.1 | DIDEC..... | 44 |
| | 3.2.2 | Program Radius..... | 45 |
| | 3.2.3 | Program Check..... | 46 |
| | 3.2.4 | Program Clean..... | 47 |
| CHAPTER | 4 | MODEL VALIDATION..... | 51 |
| | 4.1 | Current Distribution Display.... | 51 |
| | 4.2 | Radiation Pattern Plots..... | 52 |
| | 4.3 | Radiated Power and Isotropic Level..... | 54 |
| CHAPTER | 5 | EC-130 HF ANTENNA INSTALLATION.. | 59 |
| | 5.1 | Measurements..... | 62 |
| | 5.1.1 | Scale Model..... | 62 |
| | 5.1.2 | Full Scale..... | 63 |
| | 5.2 | Wire Grid Model Generation -Base Model..... | 65 |
| | 5.2.1 | Current Distribution..... | 70 |
| | 5.2.2 | Radiation Patterns..... | 74 |
| | 5.2.2.1 | Computed vs.Scale Model..... | 74 |
| | 5.2.2.2 | Computed vs. Full Scale..... | 76 |
| | 5.3 | Geometrical Perturbations..... | 89 |
| | 5.3.1 | Segmentation..... | 89 |
| | 5.3.1.1 | Wire Grid G..... | 92 |
| | 5.3.1.2 | Wire Grid Models H and I..... | 95 |
| | 5.3.1.3 | Triangulated Model P..... | 98 |
| | 5.3.2 | Radius..... | 104 |
| | 5.3.2.1 | Wire Grid J..... | 105 |
| | 5.3.2.2 | Wire Grid K..... | 106 |

| | | |
|-----------------|-----------------|-----|
| CHAPTER 6 | CONCLUSION..... | 124 |
| APPENDIX A..... | | 129 |
| APPENDIX B..... | | 135 |
| APPENDIX C..... | | 146 |
| REFERENCES..... | | 157 |

GLOSSARY OF SYMBOLS AND TERMS

| | |
|------------------|---|
| η | Intrinsic Impedance |
| η_e | Radiation Pattern Efficiency |
| λ | Wavelength |
| a | Wire Radius |
| L | Wire Length |
| Δ | Segment Length |
| β | Phase constant or Wave Number |
| γ | Euler's Constant |
| N | Number of Segments |
| E_θ | Vertical Component of Radiated Field |
| E_ϕ | Horizontal Component of Radiated Field |
| $\%E_\theta$ | Percentage of E_θ Power |
| sub $\%E_\theta$ | Percentage of useful E_θ Power |
| ATLAS | Antenna Testing Laboratory Automated System |
| AUT | Antenna Under Test |
| EMC | Electromagnetic Compatibility |
| NATC | Naval Air Test Center |
| NEC | Numerical Electromagnetic Code |
| RAD | Wire Radius |
| SEG | Segment Length |
| WAV | Wavelength |

CHAPTER 1

INTRODUCTION

HF aircraft antennas must radiate electric field patterns of sufficient gain in directions significant to communications. In addition, a suitable input impedance for acceptable power transfer efficiency between the transmitter and the radiated field is required (Jasik).

In the 2-30 MegaHertz (MHz) frequency range, the principal dimensions of an airframe are comparable to a wavelength. Whenever the major dimensions are of the order of a wavelength, the airborne antenna induces RF currents on the conducting airframe surface which significantly affect the antenna impedance and pattern behavior. Consequently, the evaluation of radiation characteristics of aircraft antennas in the HF band must include the airframe current contribution.

The radiation patterns in this range may be explained by considering the fuselage, wings and horizontal and vertical stabilizers as current filaments with appropriate relative amplitudes and phases (Granger). Then, the total electric field is readily computed by summing the radiation from different portions of the airframe and the antenna

installation. Methods to evaluate aircraft antenna radiation patterns include full scale airborne testing, scale model measurement and numerical model computation.

1.1. Full Scale Measurements

Full scale pattern measurements provide a means of verifying scale and computer model calculations. One example of an in-flight test facility for investigating antenna performance is the Antenna Testing Laboratory Automated System (ATLAS) in Chesapeake Bay.

ATLAS is designed to evaluate antenna systems operating in the 2 MHz to 18 GHz range. The topography of the site, comprising of the calm waters of Chesapeake Bay and surrounding low level land masses, present an unobstructed field-of-view in an area free of electromagnetic interference sources (ATLAS Report SY-81).

During the testing procedure, the aircraft transmits a specified signal through the antenna under test (AUT). The ground system antennas receive and, subsequently, process the signal for antenna performance assessment (figure 1).

Although full scale airborne testing is a realistic approach in aircraft antenna pattern

evaluations, the immense amount of time and cost involved make it an impractical method of measurement.

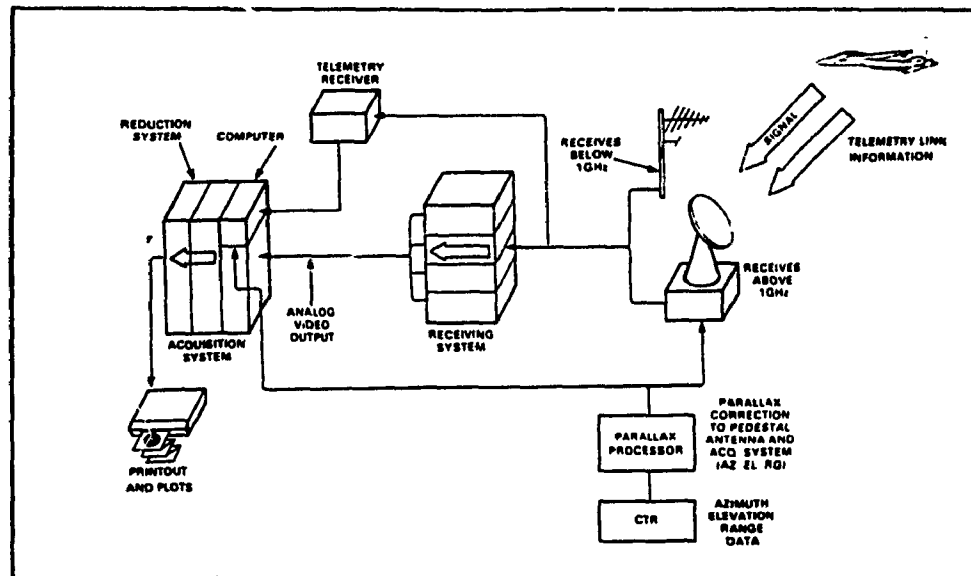


Figure 1 Full Scale Measurements (ATLAS)

1.2. Scale Model Measurements

Scale modelling is one alternative for investigating aircraft antenna patterns. The requirements for simulation by the model are

1. all dimensions of the model are $1/n$ times those of the full scale prototype.
2. operating frequency and conductivity of the model are 'n' times those of the

prototype

3. dielectric constant and permeability of the model are the same as those of the full scale prototype

where 'n' is an arbitrary scale factor (Sinclair).

As a result of the reciprocity theorem, measurement of antenna patterns may be made under either transmitting or receiving conditions. In the transmitting mode, a battery-operated oscillator, inserted in the scale model, excites the antenna under test. The radiated field is detected by a probe antenna oriented to measure the desired polarization.

Figure 2 illustrates a typical set-up for determining the electric field of model antennas in the receiving mode. The pattern of an antenna when receiving plane waves from the horn type radiator, may be determined by connecting a receiver to the AUT and measuring the receiver output as the direction of the incident wave is varied (Sinclair).

Inaccuracies in field measurements are likely caused by cables connected to the scale model which perturb the patterns. In addition, particular attention must be paid to reflections from the model supporting structure.

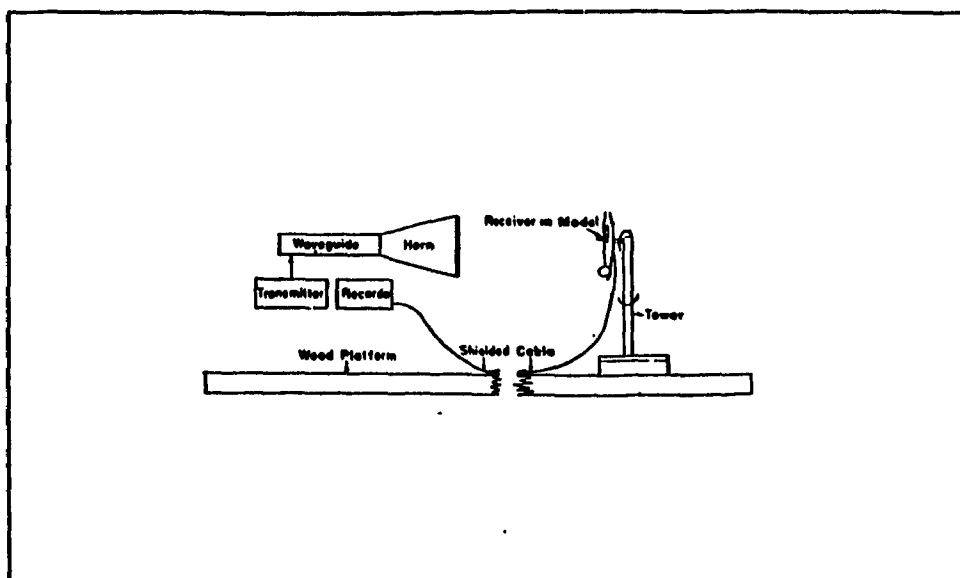


Figure 2 Scale Model Measurement (Sinclair)

1.3. Numerical Model Computation

Full scale and scale model measurements are hampered by cost and time factors and are advantageously replaced by computer simulation techniques. Computer modelling yields numerical solutions to electromagnetic problems with an accuracy and completeness unobtainable by experimental measurements (Tanner). The numerical model readily reveals the current density distribution and this provides additional insight into input impedance and radiation characteristics of the airframe-antenna system.

A computer model is composed of wire segments which electromagnetically approximate a continuous surface i.e. the wire grid mesh current simulates the

local variations in surface current density.

The Integral Equation approach is used to determine the current distribution. In this method, the Electric Field Integral Equation (EFIE) relates the unknown current on the wires to the known applied electric field.

The Integral Equation is then solved for the currents by the Moment Method. Once the current distribution has been found, the radiation pattern may be computed from the radiation integral.

1.4. Model Validation

In order to validate the numerical model, the computed results are compared to full scale and scale model measurements. Thus experimental measurements are still required, however, a validated computer model serves to fill the gaps in the measurement data. Furthermore, a sound computer model can provide information such as induced RF currents and input impedance, which are generally difficult to obtain by direct measurement.

Full scale and scale model measurements are used to verify the credibility of a computer model. Conversely, a numerical model may be employed to confirm the validity of the experimental measurements.

1.5. Objective

The objective of this thesis is to develop a valid computer model of the EC-130 Tacamo for radiation pattern analysis of its HF antenna system. The numerical model will further serve to qualify prior full scale and scale model measurements provided by the United States Naval Air Test Center.

The EC-130 HF antenna installation consists of five long wire antennas. A top view of the aircraft with all five high frequency antennas is shown in figure 3.

The Tacamo computer model was developed to clarify the discrepancies between the full scale and scale model radiation patterns. Reliable measurement data was unavailable for numerical model validation purposes. Consequently, only incremental variations in wire mesh topology were effectuated. This approach increased confidence in model credibility as well as offered new insight into the wire grid modelling methodology.

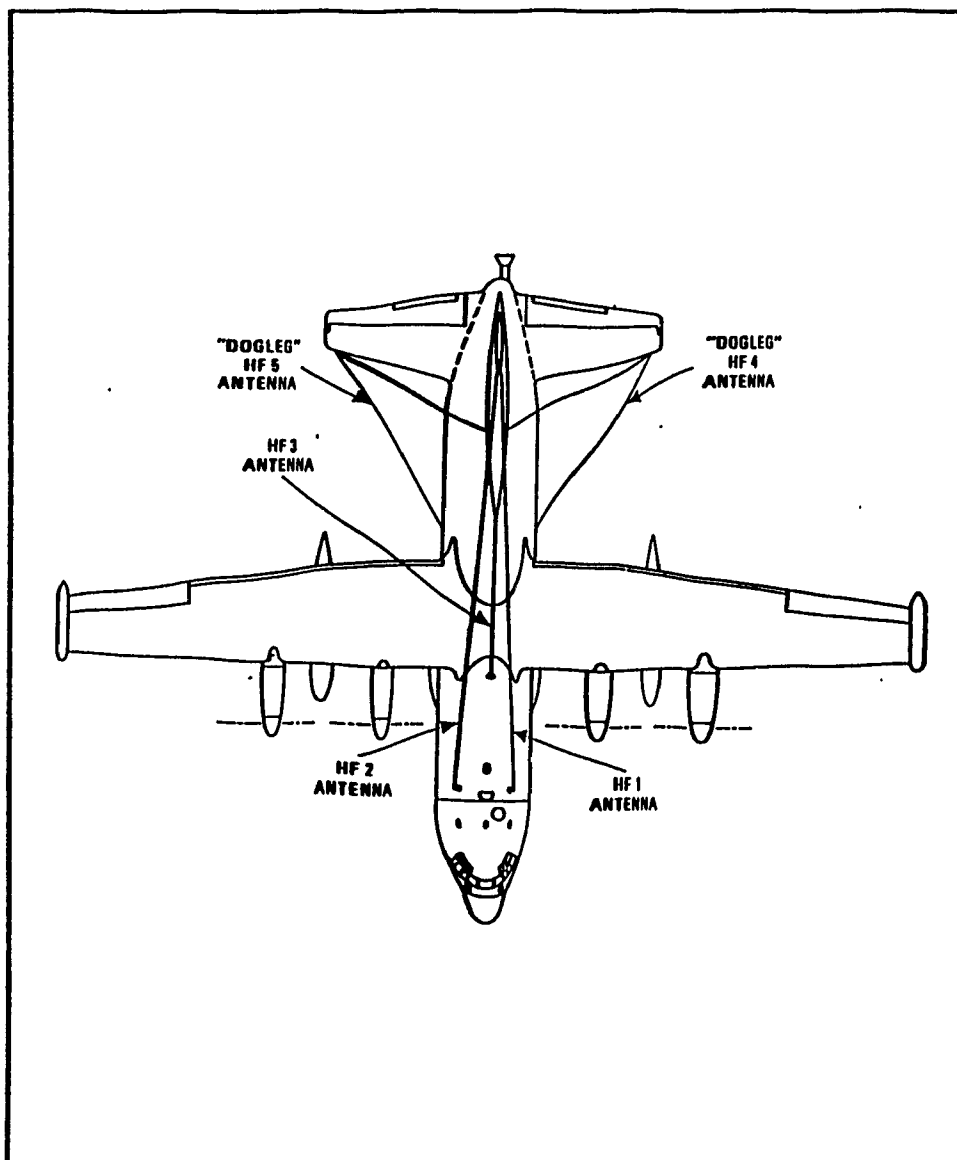


Figure 3 EC-130 HF Antenna Installation

Chapter 2

NUMERICAL ELECTROMAGNETICS CODE

The Numerical Electromagnetics Code (NEC) is a computer code for the analysis of electromagnetic radiating and scattering structures. A numerical model of the structure consists of conducting wires. The excitation can be either a voltage source or an incident plane wave, and the output includes induced currents and radiated fields.

2.1 . Numerical Electromagnetics Code Input Format

The NEC input (NECIN) data describes the antenna and its environment, and requests computation of antenna characteristics (Burke and Poggio). The NECIN file is divided into three sections: comment lines, structure geometry input, and program control directives. A two-letter alphabetic mnemonic serves to identify each program line function (figure 4).

The input file begins with one or more comment lines (CM) which may contain a brief description and structure parameters identifying the run. A CE card indicates the end of the comment field.

The geometry of the wire-grid model is detailed in the structure geometry section of the NECIN file. GW lines specify the following wire parameters in

order: tag number, number of segments, end one coordinates (x,y,z), end two coordinates (x,y,z) and radius, all in meters.

The GM geometry opcode enables the translation of a structure with respect to the coordinate system. For example, the GM feature may be used to shift a structure a specified distance above a ground plane. A GE line signals the end of the geometry field.

Program control lines set electrical parameters for the model, select options for the solution procedure, and request data computation (Burke and Poggio).

The electrical properties of the wire-grid model are specified in the EK, FR, LD and GN lines. The EK option involves the extended thin wire kernel approximation in the solution procedure of NEC. This results in greater accuracy in evaluating the near fields of thick wires.

The frequency of operation is found in the FR line of the input file. The units are in megahertz.

The type of impedance loading on a segment is identified by the LD line of the NECIN file. Series and parallel RLC networks can be generated. In addition, impedance (resistance and reactance) and wire conductivity (mhos/meter) can be specified.

A GN mnemonic indicates the presence of a ground

plane. The ground may be perfect i.e. infinite in extent and perfectly conducting, or lossy for which the relative dielectric constant and conductivity are required.

The mnemonic EX specifies the excitation of the structure. The types of excitation include a voltage source on an antenna, or an arbitrarily polarized plane-wave incident on the structure.

Program control line WG and geometry structure mnemonic GF signal the Numerical Green Function (NGF) option in NEC. With the NGF function, a fixed structure and its environment may be modelled and the associated NEC computations are saved on a file. Part of the model may then be modified in subsequent computer runs and the complete solution obtained without repeating calculations for the data on the file (Burke and Poggio). The WG line causes the NGF information to be written to a file and the GF line prompts the program to read the file. The Numerical Green Function significantly reduces the amount of CPU time of a NEC execution by avoiding unnecessary repetition of calculations.

The RP line causes the wire currents to be calculated, and requests radiation pattern computation. Theta and phi angles are provided to define the far field point.

```

CM      EC-130 AIRCRAFT
CM
CM      BASE MODEL F
CM
CM      EXCITATION - HFI
CM
CM      COMPUTED
CM
CZ
GV 1 1 -4.010 -1.563 3.317 -4.010 -2.139 1.000 0.424
GV 2 1 -4.010 -2.139 1.000 -4.010 -1.563 0.394 0.423
GV 3 1 -4.010 -1.563 0.394 -4.010 0.000 0.000 0.407
GV 4 1 -3.209 0.000 3.033 -3.209 -1.189 3.100 0.300
GV 5 1 -3.209 -1.189 3.100 -3.209 -1.703 1.000 0.347
GV 6 1 -3.209 -1.703 1.000 -3.209 -1.189 0.324 0.341
GV 7 1 -3.209 -1.189 0.324 -3.209 0.000 0.123 0.373
GV 8 1 -1.590 -0.914 1.753 -1.590 -0.777 0.945 0.265
.
.
.
GV367 1 -23.583 -0.054 0.374 -23.244 -0.004 9.107 0.010
GV368 1 -4.010 0.000 4.039 -4.010 -0.940 3.605 0.004
GV369 1 -4.010 -0.940 3.605 -4.010 -1.563 3.317 0.123
GV370 1 -4.010 0.000 4.039 -4.010 1.160 3.500 0.004
GV371 1 -4.010 1.160 3.500 -4.010 1.563 3.317 0.123
GV372 1 -11.243 0.000 4.039 -11.243 -0.354 3.922 0.067
GV373 1 -11.243 -0.354 3.922 -11.243 -1.563 3.317 0.123
CE
EX
EX 0 335 1 1.0
FR 0 0 4.04
RP 0 1 73 0 0 0 5
RP 0 1 73 25. 0. 0. 5.
RP 0 1 73 37 0 0 5.
RP 0 1 73 45. 0 0. 5.
RP 0 1 73 53 0. 0. 5.
RP 0 1 73 60 0. 0. 5.
RP 0 1 73 66 0 0. 5.
RP 0 1 73 72 0. 0. 5.
RP 0 1 73 78 0 0. 5.
RP 0 1 73 84. 0. 0. 5.
RP 0 1 73 90 0. 0. 5.
RP 0 1 73 96. 0 0. 5.
RP 0 1 73 102. 0 0. 5.
RP 0 1 73 108 0. 0. 5.
RP 0 1 73 114 0. 0. 5.
RP 0 1 73 120. 0. 0. 5.
RP 0 1 73 127 0. 0. 5.
RP 0 1 73 135. 0. 0. 5.
RP 0 1 73 143. 0. 0. 5.
RP 0 1 73 155. 0. 0. 5.
RP 0 1 73 160 0 0. 5.
RP 0 73 1 0 0. 5. 0.
RP 0 73 1 0 90 5 0
EN

```

Figure 4 Sample NEC Input File

The EN line indicates the end of all program execution.

2.2. Pocklington's Integral Equation

The Numerical Electromagnetic Code (NEC) analyzes the electromagnetic response of arbitrary configurations consisting of wires in free space or over a ground plane (Burke and Poggio). The program invokes the Method of Moments to solve the Electric Field Integral Equation (EFIE) for currents induced on the structure by sources or incident fields. Once the current density is found, the scattered fields are readily determined by traditional radiation integrals.

An integral representation for the electric field of a current distribution with boundary conditions form the basis of Pocklington's Integral Equation. By satisfying the boundary conditions on the surface of a perfectly conducting wire, Pocklington expresses the unknown current on the wire in terms of the known incident field illuminating the wire antenna or scatterer.

Consider a wire segment of length, L , and radius, a , located on the axis of a 'local' coordinate system (figure 5).

The incident field that impinges on the surface of the wire induces on it an electric current density $\vec{J}(\vec{r}')$, which in turn radiates the scattered field $\vec{E}^s(\vec{r})$.

The wire segment is a perfect conductor and,

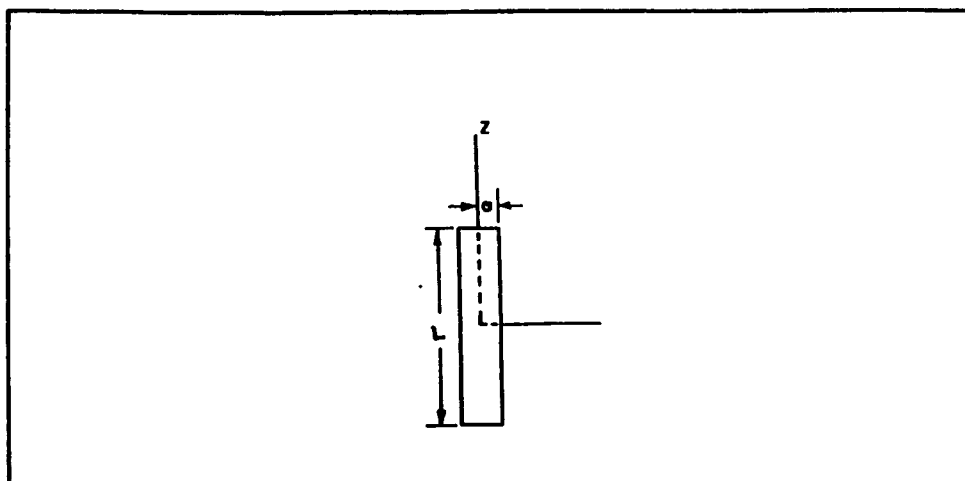


Figure 5 Wire in local coordinate system

thus, can be represented by a tube of surface current density such that

$$\vec{J}(\vec{r}) = \vec{J}_s(\phi', z') ; \rho' = a.$$

The scattered field due to the surface current is

$$\vec{E}^s(\rho, \phi, z) = -j\omega\mu\vec{A}(\rho, \phi, z) + \frac{1}{j\omega\epsilon} [\nabla \cdot (\nabla \vec{A}(\rho, \phi, z))]$$

where the magnetic vector potential,

$$\vec{A}(\rho, \phi, z) = \frac{1}{4\pi} \iint_{s'} \vec{J}_s(\phi', z') \frac{\exp(-j\beta R)}{R} ds'.$$

The magnitude, R , is the distance between the source point on the current cylinder to an arbitrary field point, P .

2.2.1. Thin Wire Analysis

When the wire is sufficiently thin ($a \ll \lambda$), the following thin wire approximations are applied:

- i. transverse currents can be neglected relative to axial currents on the wire
- ii. the circumferential variation in the axial current can be neglected.

Consequently, the surface current can be replaced by a simple axial current

$$I(z') \hat{z}' = 2\pi a \vec{J}_s(z')$$

where $I(z')$ is assumed to be an equivalent filament line source current induced on the wire axis (figure 6).

The vector potential is expressed as

$$\vec{A}(\vec{r}) = A_z(\rho, \phi, z) \hat{z}' = \frac{1}{4\pi} \hat{z}' \int_{\phi'=0}^{2\pi} \int_{z'=-L/2}^{L/2} \frac{I(z')}{2\pi a} \frac{\exp(-jkR)}{R} a d\phi' dz'.$$

The distance, R , between the source point on the wire axis at

$$\vec{r}' = z' \hat{z}'$$

and the field point, P , at

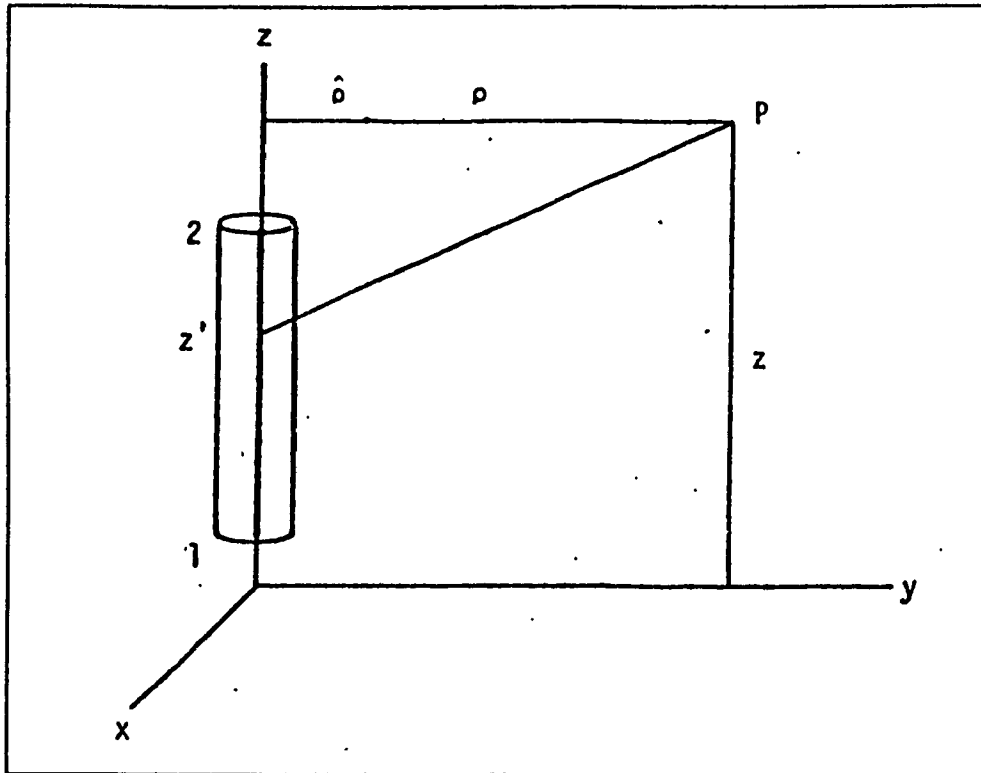


Figure 6 Thin Wire Analysis

$$\vec{r} = (\rho \cos \phi) \hat{x} + (\rho \sin \phi) \hat{y} + (z) \hat{z}$$

is given by

$$R = |\vec{r} - \vec{r}'| = \sqrt{\rho^2 \cos^2 \phi + \rho^2 \sin^2 \phi + (z - z')^2} = \sqrt{\rho^2 + (z - z')^2}.$$

Thus the vector potential for a current filament of strength $I(z')$ located on the wire axis reduces to

$$A_z \hat{z} = \hat{z} \frac{1}{4\pi} \int_{z'=-L/2}^{L/2} I(z') \frac{\exp(-jk\sqrt{\rho^2 + (z - z')^2})}{\sqrt{\rho^2 + (z - z')^2}} dz'$$

The scattered electric field due to the current line

source can be found from the following equation

$$\vec{E}^s = -j\omega\mu\vec{A} + \frac{1}{j\omega\epsilon}\nabla(\nabla\cdot\vec{A}).$$

The component of the electric field in the direction of the unit vector \hat{z} at the observation point

$$\vec{E}_z^s = \vec{E}^s \cdot \hat{z} = -j\omega\mu\vec{A} \cdot \hat{z} + \frac{1}{j\omega\epsilon} [\nabla(\nabla\cdot\vec{A}) \cdot \hat{z}]$$

$$E_z^s = -j\omega\mu A_z(\hat{z} \cdot \hat{z}) + \frac{1}{j\omega\epsilon} [\nabla(\frac{\partial A_z}{\partial z}) \cdot \hat{z}].$$

The second dot product on the right side of the field equation is the directional derivative in the direction \hat{z} (Trueman). Thus,

$$E_z^s = -j\omega\mu(\hat{z} \cdot \hat{z}) \left[\frac{1}{4\pi} \int_{z'=-L/2}^{L/2} I(z') G(\rho, z, z') dz' \right] \\ - \frac{j}{\omega\epsilon} \frac{d}{dz} \left[\frac{1}{4\pi} \int_{z'=-L/2}^{L/2} I(z') \frac{\partial G(\rho, z, z')}{\partial z} dz' \right].$$

It is readily shown by differentiating the thin wire kernel that

$$\frac{\partial G}{\partial z} = -\frac{\partial G}{\partial z'}.$$

Thus,

$$E_z^s = -j\omega\mu(\hat{z} \cdot \hat{z}) \left[\frac{1}{4\pi} \int_{z'=-L/2}^{L/2} I(z') G(\rho, z, z') dz' \right] \\ + \frac{j}{\omega\epsilon} \frac{d}{dz} \left[\frac{1}{4\pi} \int_{z'=-L/2}^{L/2} I(z') \frac{\partial G(\rho, z, z')}{\partial z'} dz' \right].$$

The z-component of the scattered field at the observation point

$$E_z^s = \frac{-j\eta}{4\pi k} \int_{z'=-L/2}^{L/2} I(z') \left[k^2 (\hat{z} \cdot \hat{z}') - \frac{\partial^2}{\partial z \partial z'} \right] G(\rho, z, z') dz'$$

where the wave number

$$k = \omega \sqrt{\mu \epsilon}$$

and the intrinsic impedance

$$\eta = \sqrt{\frac{\mu}{\epsilon}}.$$

2.2.2. Extended Thin Wire Kernel

The Numerical Electromagnetics Code implements the extended thin wire approximation for wire radii that are too thick for the thin wire approximation. The EK option assumes that the current is uniformly distributed around the circumference of the wire.

The derivation of the extended thin wire kernel begins with the current on the surface of the source segment with surface density

$$J(z') = \frac{I(z')}{2\pi a}$$

A current filament of strength

$$\frac{Id\phi'}{2\pi}$$

is integrated over ϕ' with

$$R = |\vec{r} - \vec{r}'| = |[\rho \cos \phi \hat{x} + \rho \sin \phi \hat{y} + z \hat{z}] - [a \cos \phi' \hat{x} + a \sin \phi' \hat{y} + z' \hat{z}]|$$

$$R = \sqrt{\rho^2 + a^2 - 2ap \cos(\phi - \phi') + (z - z')^2}$$

(figure 7). Because of the symmetry of the scatterer, the electric field does not vary with ϕ . For simplicity, let $\phi = 0$, then

$$R = \sqrt{\rho^2 + a^2 - 2ap \cos \phi' + (z - z')^2}.$$

The magnetic vector potential

$$\vec{A}(\vec{r}) = A_z(\rho, z) \hat{z} = \hat{z} \frac{1}{4\pi} \int_{z'=-L/2}^{L/2} I(z') G_{EK} dz'$$

where the full kernel

$$G_{EK} = \frac{1}{2\pi} \int_{\phi'=0}^{2\pi} \frac{\exp(-jk\sqrt{\rho^2 + a^2 - 2ap \cos \phi' + (z - z')^2})}{\sqrt{\rho^2 + a^2 - 2ap \cos \phi' + (z - z')^2}} d\phi'.$$

The full kernel integral over cannot be evaluated in closed form. However a numerical method of approximation may be used to evaluate the full kernel, G. NEC expands

$$\frac{\exp(-jkR)}{R}$$

as a series in powers of a . Let the function f , be

$$f = \frac{\exp(-jk\sqrt{\rho^2 + (z-z')^2 + a^2 - 2ap\cos\phi'})}{\sqrt{\rho^2 + (z-z')^2 + a^2 - 2ap\cos\phi'}}.$$

Then f can be expanded in a MacLaurin series about $a=0$ with terms of order a^4 neglected (Harrington). The kernel is evaluated by integrating, over ϕ' , the series representation of f resulting in

$$G_{EK} = \frac{e^{D^{1/2}}}{D^{1/2}} \left[1 + \frac{a^2}{2D} (1+jkD)^{1/2} + \frac{\rho^2 a^2}{2D} (-k^2 D + 3(1+jkD)^{1/2}) \right]$$

where,

$$D = \sqrt{\rho^2 + (z-z')^2}.$$

The first term in the series representation of the full kernel is recognized as the reduced thin wire kernel, G .

The series approximation of the full kernel results in the reduction of the surface integral vector potential to a line integral representation

$$A_z(\rho, z) \hat{z}' = \frac{1}{4\pi} \hat{z}' \int_{z'=-L/2}^{L/2} I(z') G_{EK}(\rho, z, z') dz'.$$

The tangential z -component of the scattered field at

the observation point is

$$E_z^s = \frac{-j\eta}{4\pi k} \int_{z'=-L/2}^{L/2} I(z') \left[k^2 (z-z') - \frac{\partial^2}{\partial z \partial z'} \right] G_{EK}(\rho, z, z') dz'$$

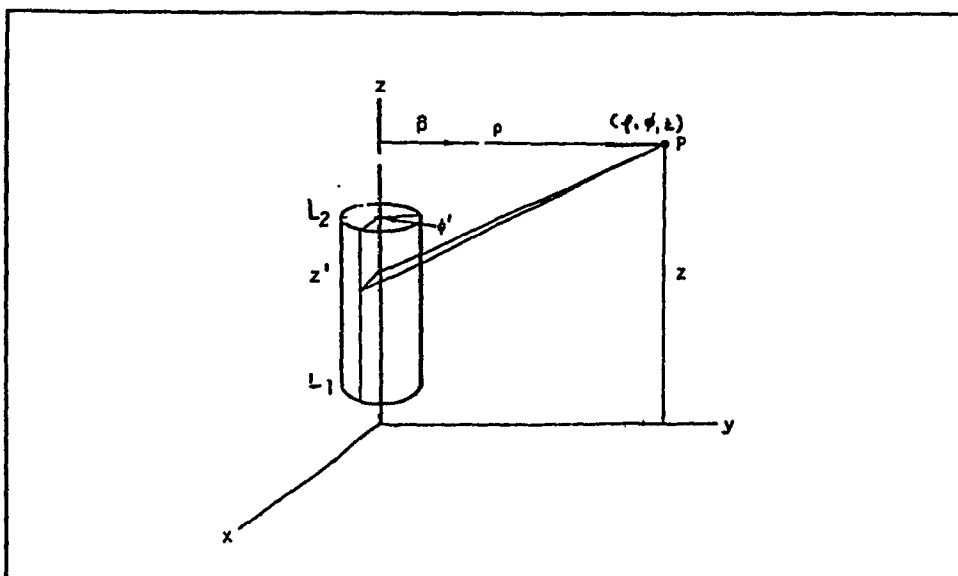


Figure 7 Extended Thin Wire Kernel

2.2.3. Boundary Conditions

The boundary conditions state that the tangential component of the total electric field at the surface of a perfect conductor is zero. The total field is the vectorial sum of the incident and scattered fields

$$\vec{E}^{TOT} = \vec{E}^i + \vec{E}^s$$

where,

E^i = incident field evaluated at the observation point
and

E^s = scattered field evaluated at the observation

point.

Enforcing the boundary conditions at any point on the surface of a wire in the axial direction

$$\vec{E}^{TOT} \cdot \hat{z} = 0$$

$$-\vec{E}^I \cdot \hat{z} = \vec{E}^S \cdot \hat{z}$$

where,

\hat{z} = unit vector tangent to the wire axis.

Pocklington's Integral Equation is obtained for a perfectly conducting wire by combining the integral representation for the electric field of wire current with boundary conditions to form:

$$\frac{-j\eta}{4\pi k} \int_{z'=-L/2}^{L/2} I(z') \left[k^2(z-z') - \frac{\partial^2}{\partial z \partial z'} \right] G(\rho, z, z') dz' = -\vec{E}^I \cdot \hat{z}$$

where z' is a point on the source wire and z is a point on the wire surface.

2.3. Method of Moments

Pocklington's Integral Equation is numerically evaluated in NEC by the Method of Moments. The Moment technique reduces the integral equation

$$\frac{-j\eta}{4\pi k} \int_{z'=-L/2}^{L/2} I(z') \left[k^2 (\hat{z} \cdot \hat{z}') - \frac{\partial^2}{\partial z \partial z'} \right] G dz' = -\vec{E}^i \cdot \hat{z}$$

to a matrix equation in terms of the unknown current, $I(z')$.

The matrix method represents the integral equation in a linear operator format such that

$$\mathcal{Q}[I(z')] = -E_z^i$$

where \mathcal{Q} denotes the integral operator, $-E_z^i$ is the known axial component of the incident field at the surface of a wire and $I(z')$ is the unknown current flowing in the wire (Harrington).

To obtain the numerical solution of the above equation, $I(z')$ is approximated by the sum of N linearly independent current basis functions defined over the wire. Symbolically,

$$I(z') = \sum_{n=1}^N H_n F_n(z')$$

where H_n are the unknown complex current coefficients to be determined.

Substituting the equation for the current summation into the linear operator electric field equation and using the linear property of the operator results in

$$\sum_{n=1}^N H_n \mathcal{Q}[F_n(z')] = -E_z^i$$

The N current coefficients are solved for by enforcing the integral equation at N distinct observation points on the wire boundary. This procedure is known as the collocation method or point matching and is equivalent to weighting the integral equation with a Dirac (impulse) delta function, located at each match point.

Sampling of the function being integrated at N discrete points will generate a system of N linear equations in N unknowns. The current coefficients can then be found by simple matrix factorization.

2.4. Current Expansion on Wires

For an arbitrary wire configuration, it is difficult to find basis functions that are well defined over the entire domain of interest. Consequently, the unknown current, $I(z')$, is approximated by basis functions which exist only over segments of the wire. Then each current coefficient, H_n , in the current basis function expansion effects

the approximation of $I(z')$ only over a subsection of the region of interest (Harrington). This method is aptly entitled the principle of subsectional bases (Ney).

In the Numerical Electromagnetic Code, the current on a segment is represented by a three-term sinusoidal subdomain basis which is thought to closely resemble the actual current distribution. Specifically, the current on segment i has the form

$$I_i(z') = H_i F_i(z) = A_i + B_i \sin k(z' - z_i) + C_i \cos k(z' - z_i)$$

$$|z - z'| < \frac{\Delta_i}{2}$$

where,

z' = distance parameter along the wire

z_i = value of z' at the center of segment i

and,

Δ_i = length of wire segment i .

Two of the three function coefficients are found by imposing current and charge continuity conditions at the segment ends. The remaining constant is proportional to the unknown current amplitude to be determined by the matrix equation.

The physical constraints at the wire ends are applied to the current, I , and to the linear charge density, q , which are related by the continuity

equation

$$\frac{\partial I(z')}{\partial z'} = -j\omega q$$

There are two possible segment end configurations to be considered - free end and junction.

2.4.1. Free End

At a free end, the current can flow onto the end cap as illustrated in figure 8. Poggio derived an equation relating the current at the free wire end to its derivative

$$I(z')|_{z'=free\ end} = -\frac{\hat{z}' \cdot \hat{n}_c}{k} \frac{J_1(ka)}{J_0(ka)} \frac{\partial I(z')}{\partial z'}|_{z'=free\ end}$$

where J_0 and J_1 are Bessel functions of order 0 and 1, respectively. The unit vector \hat{n}_c is normal to the end cap and \hat{z}' is the unit vector along the wire oriented from the entrance to the exit node.

2.4.2 Junction

In the treatment of wire junction, T.T. Wu and R.W.P. King have derived the following condition

$$\frac{\partial I(z')}{\partial z'}|_{z'=junction} = \frac{Q}{\Psi}$$

The constant, Q , is related to the total change in the area of the junction and Ψ is a radius dependant

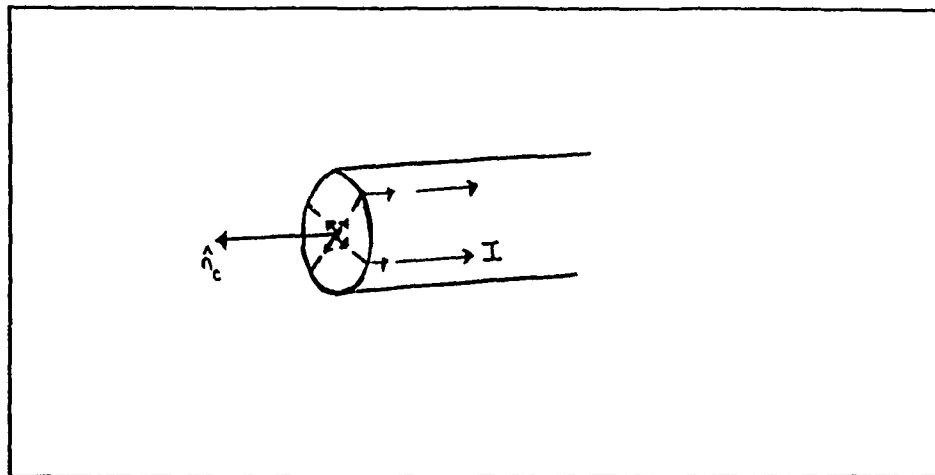


Figure 8 Free End

scale factor given by

$$\Psi = \ln\left(\frac{2}{ka} - \gamma\right)$$

where ,

a = segment radius

and

γ = Euler's constant (0.5722).

The continuity of current at the segment boundary is assured by Kirchoff's current law which states that the sum of the currents entering a junction equals the sum of the currents leaving the junction. Furthermore, the Wu-King constraint insures that the current derivative, or equivalently the charge density, is continuous across the junction and has the

form

$$\Psi \frac{\partial I_1(z')}{\partial z'} = \Psi \frac{\partial I_2(z')}{\partial z'} = \dots = \Psi \frac{\partial I_n(z')}{\partial z'}$$

or

$$\Psi_1 q_1 = \Psi_2 q_2 = \dots = \Psi_n q_n.$$

Consider the segment i illustrated in figure 9,
below

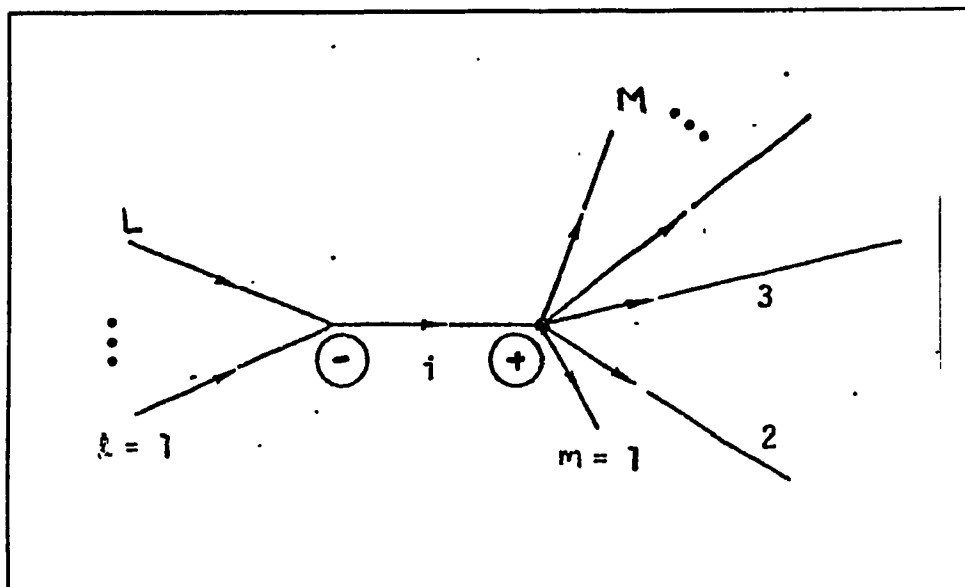


Figure 9 NEC Current Expansion

The i^{th} current basis function flows through the segment i and extends onto every segment connected to i , going to zero with zero derivative at the outer end of the connected segments (Burke and Poggio).

The portion of the i^{th} current basis function on segment i is given by

$$I_{i_0}(z') = A_{i_0} + B_{i_0} \text{sink}(z' - z_i) + C_{i_0} \text{cosk}(z' - z_i).$$

The end conditions at the entrance (-) and exit (+) nodes, respectively, are given by

$$I_{i_0}(z' = z_i \mp \frac{\Delta_i}{2}) = \pm \frac{1}{k} \frac{J_1(ka_i)}{J_0(ka_i)} I_{i_0}'(z') \Big|_{z' = z_i \mp \frac{\Delta_i}{2}} \quad \text{free end}$$

$$= \frac{Q_i^*}{\Psi_i}, \quad \text{Wu-King junction}$$

The portion of the i^{th} basis function which extends onto the segments connected at the entrance node

$$I_{i_l} = A_{i_l} + B_{i_l} \text{sink}(z' - z_l) + C_{i_l} \text{cosk}(z' - z_l) \quad l = 1, 2, \dots, L.$$

The end conditions are

$$I_{i_1}(z' = s_1 - \frac{\Delta_1}{2}) = 0$$

$$\frac{dI_{i_1}(z' = z_1 - \frac{\Delta_1}{2})}{dz'} = 0$$

$$\frac{dI_{i_1}(z' = z_1 + \frac{\Delta_1}{2})}{dz'} = \frac{Q_1^*}{\Psi_1}.$$

Since the charge is continuous across the junction, $Q_i^+ = Q_i^-$ and this may be substituted into the end condition

$$\frac{dI_{i_1}(z'=z_1+\frac{\Delta_1}{2})}{dz'} = \frac{Q_i^-}{\Psi_1}.$$

Similarly, the portion of the i^{th} basis function which extends onto the segments at the exit node

$$I_{i_m} = A_{i_m} + B_{i_m} \text{sink}(z' - z_m) + C_{i_m} \text{cosk}(z' - z_m) \quad m=1, 2, \dots, M.$$

The end conditions

$$I_{i_m}(z'=z_m+\frac{\Delta_m}{2})=0$$

$$\frac{dI_{i_m}(z'=z_m+\frac{\Delta_m}{2})}{dz'}=0$$

$$\frac{dI_{i_m}(z'=z_m-\frac{\Delta_m}{2})}{dz'} = \frac{Q_i^+}{\Psi_m}.$$

The complete current basis function on segment i , defined by equations I_{i_0} , I_{i_1} , and I_{i_m} , involves $3(1+m+n)$ unknowns. The value of $(2+3L+3M)$ current coefficients are found in terms of Q_i^+ and Q_i^- by enforcing end conditions. The charge densities are

then solved for by applying Kirchoff's current law at the segment ends such that

$$\sum_{l=1}^L I_{i_l} (z' = z_l + \frac{\Delta_l}{2}) = I_{i_0} (z' = z_l - \frac{\Delta_l}{2})$$

$$\sum_{m=1}^M I_{i_m} (z' = z_m - \frac{\Delta_m}{2}) = I_{i_0} (z' = z_l + \frac{\Delta_l}{2})$$

The complete i^{th} current basis function, $I_i = H_i F_i(z')$, has now been defined leaving one amplitude constant, related to the current expansion coefficient, H_i , to be solved by the method of moments.

2.5. Calculation of Structure Matrix

The method of subsectional collocation involves dividing a wire structure into N segments with the current amplitude being an unknown over each segment. At the center of the m^{th} segment, the electric field boundary conditions are enforced. Hence, the sum of the tangential components of the scattered fields due to the N current basis functions along the N segments is set equal to the negative of the axial incident field at the observation point z_m :

$$\sum_{n=1}^N H_n \mathcal{Q}[F_n(z')] = -E^i(z_m)$$

Thus far only one equation in N unknown has been derived. The remaining $(N-1)$ equations are generated

by evaluating the above expression at (N-1) discrete points along the wire:

$$\sum_{n=1}^N H_n \mathcal{G}[F_n(z')] = -E^i(z_m) \dots m=1, 2, \dots, N.$$

This equation can be written in matrix notation as

$$[G] [H] = [E]$$

where,

$$G_{mn} = \mathcal{G}[F_n(z')] |_{z=z_m}$$

$$E_m = -E^i(z_m)$$

and

$$H_n = \text{current amplitude on segment } n.$$

Each element, G_{mn} , in the generalized impedance matrix $[G]$ represents the tangential electric field at observation point z_m produced by the normalized current basis function on segment n . In particular, the diagonal elements, G_{nn} , are the self field terms.

The matrix $[E]$ is related to the electromagnetic excitation. For the transmitting case, the excitation is a voltage source of strength V , on segment m .

This results in the applied electric field entry

$$E = \frac{V}{\Delta_m}$$

where Δ_m is the length of segment m .

The generalized current matrix $[H]$ contains the unknown current weighting functions, H_n , to be determined by matrix algebra.

The matrix equation $[G][H] = [E]$ is solved by the Gauss-Doolittle technique. This method involves the factorization of $[G]$ into the product of a lower triangle $[L]$ and an upper triangle $[U]$, yielding $[L][U] = [E]$. The generalized current matrix is determined by a two step solution procedure: the expression $[L][F] = [E]$ is first solved for $[F]$ by forward substitution and then the equation $[U][H] = [F]$ is solved for $[H]$ by backward substitution.

2.6. Far Field Calculations

Once the current distribution over the wire structure is obtained, the radiated field can be computed. In the far field, the parallel ray approximation serves to simplify the radiation integral. The radiated field due to the n^{th} segment is evaluated as follows (figure 10):

the vector potential

$$\vec{A}_n = \int_L \vec{I}_n(z') \frac{\exp(-jkR)}{4\pi R} dz'$$

where,

$$R = r - r' \cos \alpha,$$

The term $r' \cos \alpha$ is recognized as the projection of \vec{r}' on \vec{r} and, by definition of the dot product, can be represented as

$$R = r - \hat{k} \cdot \vec{r}'$$

where,

$$\hat{k} = \frac{\vec{r}}{|\vec{r}|}.$$

At large distances, the field has a magnitude dependence of $1/r$ so that the integral denominator

$$R \approx r.$$

The vector potential becomes

$$\vec{A}_n = \int_L \vec{I}_n(z') \frac{\exp(-jk(r - \hat{k} \cdot \vec{r}'))}{4\pi r} dz'$$

$$\vec{A}_n = \frac{\exp(-jkr)}{4\pi r} \int_L \vec{I}_n(z') \exp(j\vec{k} \cdot \vec{r}') dz'.$$

The electric far field produced by the current on segment n is derived below:

$$\vec{E}_n = -j\omega\mu\vec{A}_n - (-j\omega\mu\vec{A}_n \cdot \hat{K}) \hat{K}$$

$$\vec{E}_n = jk\eta [(\vec{A}_n \cdot \hat{K}) \hat{K} - \vec{A}_n]$$

$$\vec{E}_n = \frac{jk\eta}{4\pi} \frac{\exp(-jkr)}{r} \int_L [(\vec{I}_n(z') \cdot \hat{K}) \hat{K} - \vec{I}_n(z')] \exp(j\vec{k} \cdot \vec{r}') dz'$$

The integral can be evaluated for each wire segment. The radiation field at observation point P is found by the superposition of the fields due to each segment n

$$\vec{E} = \sum_{n=1}^N \frac{jk\eta}{4\pi} \frac{\exp(-jkr)}{r} \int_{L_n} [(\vec{I}_n(z') \cdot \hat{K}) \hat{K} - \vec{I}_n(z')] \exp(j\vec{k} \cdot \vec{r}') dz'$$

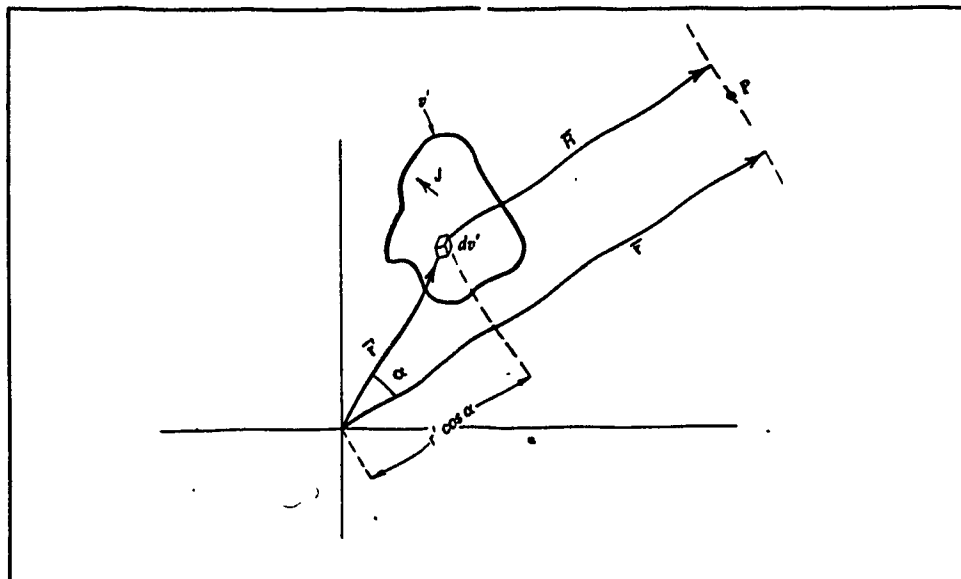


Figure 10 Parallel Ray Approximation for Far Field

2.7. The Effect of a Ground Plane

The far field patterns of antennas above ground are calculated by means of the specular ray approximation and Fresnel reflection coefficients. Reflection coefficient analysis is performed by simply adding a direct wave with a ground reflected wave of appropriate magnitude and phase.

For perfectly conducting half-space below the boundary, the incident wave is completely reflected with zero fields below the interface. The reflected field is assumed to originate from a mirror image of the source in the ground plane. The radiated field is then the sum of the direct field of the primary source and the image source field (figure 11).

The image principle can be easily extended to

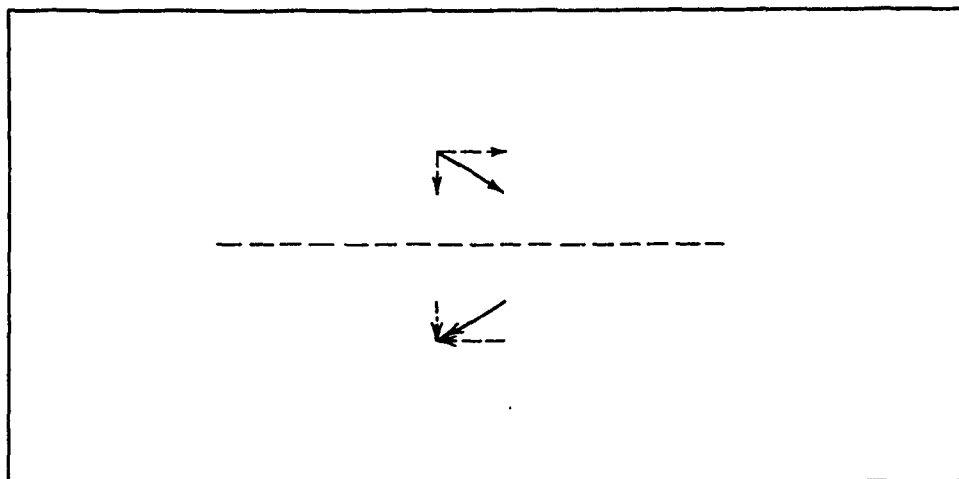


Figure 11 A Source and its Image

account for the effect of finitely conducting half space on the fields of radiating structures. As in the case of perfect ground, the total far field is the vector sum of the direct and ground reflected fields. The reflected electric field is simply the product of the perfect ground image field and the Fresnel reflection coefficient. The reflection coefficient is a function of the ground conductivity and dielectric constant, the angle of incidence and the polarization of the incident wave.

Using reflection coefficient rather than the method of moments reduces the time required for the analysis of antenna-ground interaction problems.

2.8. NEC Solution File

The compressed NEC solution file consists of the NEC input data file, the frequency in MHz, the complex input impedance, the currents at segment match points in absolute segment order, and the electric fields in the selected cuts.

It should be noted that in NEC, the total current at the center of a segment is composed of the basis function associated with said segment as well as the contributions of all the basis functions extending onto the segment. The current in the solution file is written in terms of magnitude and phase.

The electric field includes both E-theta and E-phi polarizations (magnitude and phase). NEC computes the radiated field by omitting the factor e^{-jkr}/r from the far field expression.

The last line of the solution file indicates the total computer time consumed in CPU seconds.

CHAPTER 3

WIRE GRID MODEL DEVELOPMENT

Computer models are used to study properties of antennas. An accurate numerical representation of the physical reality requires a suitable model. A credible model will support a similar current distribution to that which exists on the actual structure surface. In this chapter, several guidelines for effective modelling of a structure are outlined.

3.1. Guidelines

Continuous, metallic surfaces are numerically modelled as a network of intersecting wires. Conducting wire-grids electromagnetically approximate solid surfaces, provided that the mesh size is small compared to a wavelength.

In NEC, wires are composed of linear segments. The number of segments in a general N -segment structure should be the minimum required for accuracy since the CPU time consumed varies as N^2 for the calculation of the impedance matrix, and as N^3 for the subsequent computation of the admittance matrix.

Both geometrical and electrical factors must be considered when developing a wire-grid model.

Geometrically, the segments should follow the paths of conductors as closely as possible, using a piecewise linear fit on curves (Burke and Poggio). Adjacent segments must have coincident end points because the current expansion is determined by satisfying current and charge density conditions at segment junctions.

The density of segmentation should be sufficient to represent the local variations in both surface geometry and current density. In addition, Miller and Burke have found that maximum solution accuracy is obtained when using segments of nearly equal length.

The main electrical consideration is segment length, Δ , relative to wavelength, λ . When applying the collocation method with sinusoidal current interpolation, ten current samples per wavelength should be used to obtain reliable far field results (Miller). Thus the segment length is less than about 0.1λ at the desired frequency. Somewhat longer segments are acceptable on wires with no abrupt changes.

The wire radius is selected for impedance equivalence of the closed surface and the corresponding wire grid model. Lee, Marin and Castillo have derived the following expression for the difference in inductance, ΔL , between the solid surface and its wire mesh approximation:

$$\Delta L = \frac{\mu d}{2\pi} \ln\left(\frac{d}{2\pi a}\right)$$

where a is the wire radius and d is the axial separation of parallel wire. The inductance error (ΔL) should be minimal if the current generated on the wire grid is to be a good approximation to that on the actual surface. From the inductance equation, a negligible inductance difference requires wires of circumference approximately equal to the spacing between them (Moore and Pizer). Hence, for a square wire grid, the total surface area of the wires is twice the area of the solid surface. This is known as the 'same surface area' principle.

Wire radius is limited by the thin wire approximations used in the electric field integral equation. The first approximation assumes that the total current flowing in a wire can be accounted for by the axial current alone. The accuracy of the numerical solution for the dominant, axial current is dependent on Δ/a . Miller and Deadrick have shown that segments whose lengths are shorter than several wire diameters exhibit non-physical current oscillations near wire ends and source regions. In order to compute reliable electric field values, the ratio of segment length to radius must be greater than 8. Use

of the extended thin wire kernel extends the lower limit for Δ/a to 2. Small Δ/a produce greater error in the field solution than in the current solution. Reasonable currents have been obtained for Δ/a down to about 2 and with the EK option for Δ/a as low as 0.5.

The wire diameter is further limited by the thin wire condition of 'circumferentially independent', axial currents. When the wire radius is very small relative to the wavelength, the azimuthal variation of the current can be neglected. The validity of this thin wire approximation is insured by enforcing the following constraint

$$2\pi a < \lambda.$$

The diameter of connected segments should be sufficiently uniform to accurately model the local behavior of physical currents. Large radius changes between adjacent segments decrease solution reliability. This problem may be alleviated by gradually varying the radius in steps over several segments.

Physical currents flowing through wire bends tend to 'hug the curve'. Conversely, the piecewise current approximation in NEC maintains a uniform distribution in and around the intersection (figure 12). In order to obtain reliable numerical results, the acute angle

of adjacent segments must be large enough to 'blur' the difference between the physical currents and its numerical representation. As a minimum, the angle of intersection is selected so that the center of one segment does not fall within the radius of another (figure 13).

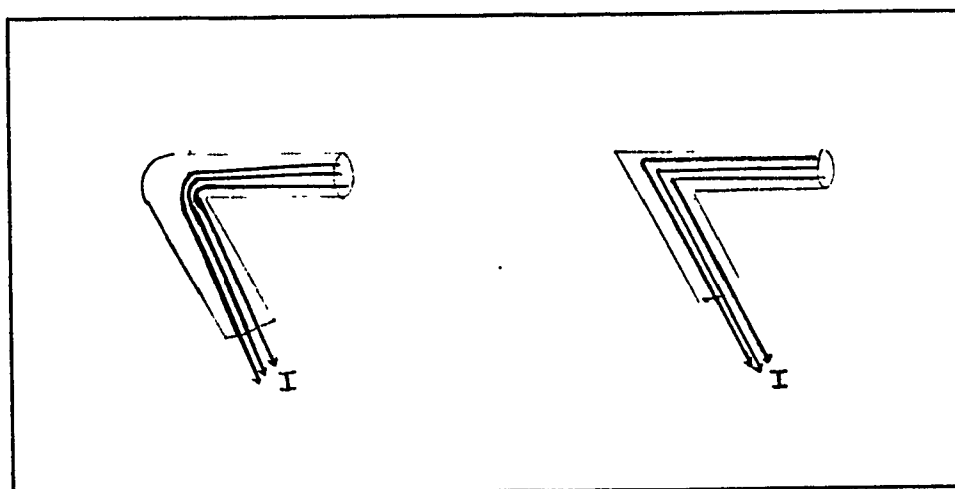


Figure 12 Physical Current and NEC Current

Currents are physically continuous at an intersection of two or more segments with unequal radii and at wire bends. For thin wire kernel analysis, this local behavior is adequately modelled by a current filament on the wire axis. However, the current tube assumed for the extended thin-wire kernel

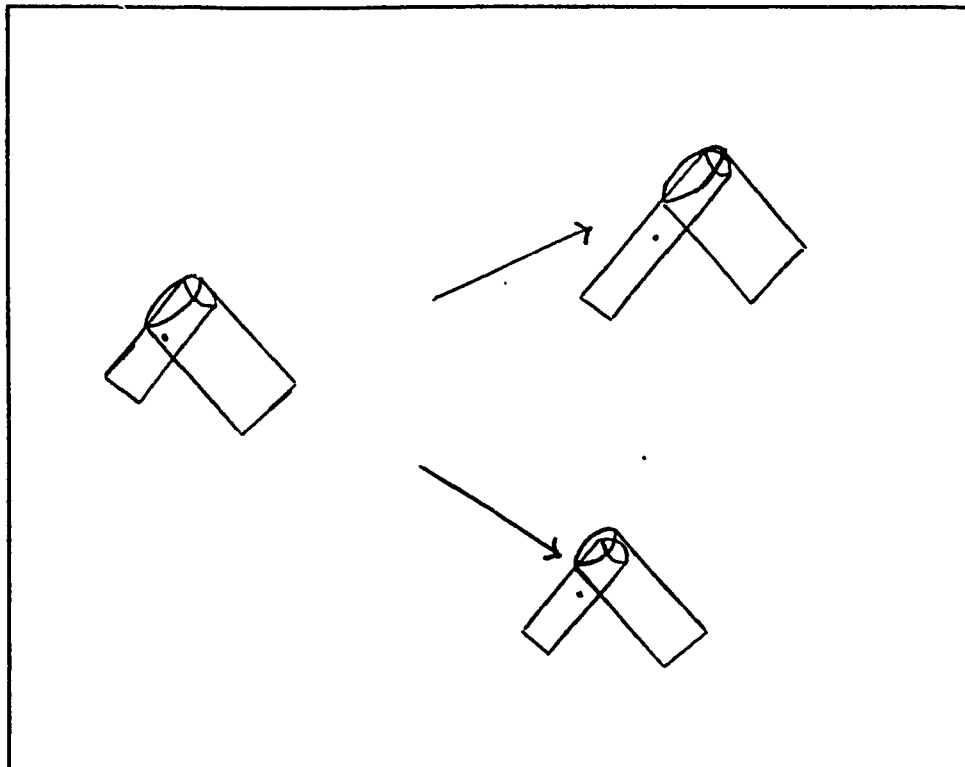


Figure 13 Junction Compatibility Requirements

cannot be continuous around its complete circumference at a bend or change in radius (Burke and Poggio). Consequently, the extended thin wire kernel is used only when two parallel, uniform segments join and at free ends. Alternatively, NEC always uses the thin wire kernel at wire bends and changes in segment diameters.

3.2. Software Modules for Model Development

3.2.1. DIDEK

The DIDEK program (Gaudine) enables computer entry of structure geometry for wire-grid model creation. DIDEK is an acronym for digitize, display, creation.

edit and convert.

A numerical model is composed of wire elements identified by their end point vertices. The vertex coordinates are derived by drafting a layout of the wire grid on a 2-dimensional projection of the structure. The x,y, and z endpoints are subsequently entered into the computer memory via digitization or keyboard entry.

Segment editing involves joining specified vertices to form the 3-dimensional wire grid model. DIDEK commands as JOIN, CHAIN, POLYGON and CUT are used for wire manipulation purposes.

Front, side, top and 3-D views of the computer model can be displayed in DIDEK. In addition, a section of the display may be 'blown' to magnify model details.

Finally, the DIDEK geometry data file is converted into a format suitable for NEC execution.

3.2.2. Program Radius

Wire radii are determined by invoking the 'same surface' rule of thumb where the surface area of the wires parallel to one linear polarization is made equal to the surface area of the solid surface being modelled (Ludwig). For a square grid, suitable for any polarization, the total surface area of the wire

should be twice the external surface area of the corresponding square patch.

Program Radius (Nguyen) uses the 'twice surface area' principle to compute radii for a wire grid model. The program then enters the new wire radii into the geometry section of the NEC input file.

3.2.3. Program CHECK

When developing a wire grid model, the wire radii is limited by the thin wire approximations of the computer code. In addition, the segmentation of the wire grid must be compatible with the basis and weighting functions used in the numerical implementation of the Method of Moments.

To obtain a sound numerical representation of a physical structure, the geometrical parameters are constrained by the computer program to be used for the modelling computations. A set of grid guidelines for NEC is outlined in table I.

Program Check (Trueman) is implemented to systematically 'check' wire grid models against the above criteria and report any incompatibilities. If wire parameters exceed the set limits, the degree of discrepancy is identified by a (N)ote, (W)arning or (E)rror message, error being the greatest deviation.

In the individual incompatibility section of the

check output file, wires are tested for finite length i.e. wire length > 0.01 meters. Additionally, the Δ/λ , Δ/a , and λ/a ratios are evaluated for every segment on the model to verify that the NEC constraints are satisfied.

Junction incompatibilities include overlapping or coincident wires. This error will occur if a given wire is inadvertently repeated in the NEC geometry file. The seg/seg ratio signals abrupt changes in length of adjacent segments on the structure. Similarly, sharp differences in the radii of two connected wires are reported in the rad/rad column of the check output. In order to accurately represent the flow of physical currents around wire bends, the acute angle between segments must be sufficiently large. An error in the angle is indicated if the center of one segment falls within the radius of the other (seg/rad). The Check constraints are outlined in table II.

3.2.4. Program CLEAN

Clean (Tarantino) is a Fortran program which corrects the individual and junction incompatibilities detected by program Check. The desired level of error removal (note, warning, or error) is specified by the user. The output is a 'clean' NEC input geometry file ready for execution.

| Modelling Parameter | Nominal Range or Value | Typical Reason |
|------------------------------------|---|---|
| Segment Length, Δ | $10^{-3} < \Delta < 0.1\lambda$ (at 15 MHz) | Minimum: the similarity of the constant and cos of the current expansion leads to numerical inaccuracy. Maximum: Sufficient sampling density |
| Δ as related to radius, a | $2 < \Delta/a$ (no EK option) | to avoid extraneous oscillations in computed currents near free wire ends (Burke and Poggio). |
| | $0.5 < \Delta/a$ (EK option) | |
| Radius to wavelength | $2\pi a/\lambda < 1$ | Neglect of circumferential effects |
| Radius | Same surface area rule of thumb | For impedance equivalence of closed surface and corresponding wire grid (Lee, Castillo and Marin) |
| Δ_i / Δ_j junction | $\Delta_i / \Delta_j < 5$, $\Delta_i > \Delta_j$ | To obtain maximum solution efficiency and accuracy (Miller). |

Table I: Guidelines for Wire Grid Model Development

| Modelling Parameters | Nominal Range or Value | Typical Reason |
|---|---|---|
| Radius _i /Radius _j junction | $a_i/a_j < 10, a_i > a_j$ | Abrupt radius change will decrease accuracy (Burke and Poggio). |
| Angle of Wire Bend | Segment midpoint shall not fall within connected wire radius. | To avoid placing match point in field of another. |

Individual Incompatibilities

| | | |
|-------------|----------|-------------------------------------|
| ZERO LENGTH | ERROR: | LENGTH OF WIRE < .01 M |
| SEG/WAV | NOTE: | .05 < SEG/WAVE < .1 |
| | WARNING: | .10 < SEG/WAVE < .2 |
| | ERROR: | SEG/WAVE > .2 OR < .001 |
| SEG/RAD | WARNING: | 2.0 < SEG/RAD < 8 WITHOUT EK OPTION |
| | | 0.5 < SEG/RAD < 2 WITH EK OPTION |
| | ERROR: | SEG/RAD < 2.0 WITHOUT EK OPTION |
| | | SEG/RAD < 0.5 WITH EK OPTION |
| WAV/RAD | ERROR: | WAVE/RAD < 30 |

INCOMPATIBILITIES AT JUNCTIONS

| | | |
|-------------|----------|--|
| COINCIDENCE | ERROR: | BOTH WIRES COINCIDENT |
| SEG/SEG | ERROR: | LONGER SEGMENT/SHORTER SEGMENT > 5 |
| RAD/RAD | WARNING: | LONGER RADIUS/SHORTER RADIUS > 5 |
| | ERROR: | LONGER RADIUS/SHORTER RADIUS > 10 |
| SEG/RAD | ERROR: | CENTER OF ONE SEGEMENT WITHIN OTHER RADIUS |

TABLE II: CHECK CONSTRAINTS

CHAPTER 4

MODEL VALIDATION

Validation is an essential part of model development. Both internal and external validation procedures are used to verify whether a computer model accurately reproduces the electromagnetic response of the actual structure.

Internal validation is a check that can be made concerning solution validity within the model itself (Miller). This includes 'eyeballing' the data to determine whether the computed current and field results exhibit physically reasonable behavior. Graphic display programs, available in the Electromagnetic Compatibility Laboratory, offer a clear insight into the electromagnetic phenomena of numerical models.

4.1. Current Distribution Display

SPCTRM (Larose) is a computer code used to display the currents induced on wire grid models. SPCTRM utilizes colour to represent RF current magnitude or phase on a segment. Current reference direction is indicated by an arrow. The colour hues range from blue (0 current) to red (maximum current) and offer a qualitative appreciation of current

distribution on a wire grid model.

4.2. Radiation Pattern Displays

A radiation pattern is a graphical representation of the far field properties of an antenna or scatterer. The coordinate system used at the EMC Laboratory to plot the electric field patterns of vehicle-mounted antennas is shown in figure 14. The field at any point in space is resolved into two components in a spherical coordinate system with the origin at the antenna.

In navigational terms, the x-axis is directed forward, y-axis is port and z-axis is the top. Negative axis directions are designated as aft, starboard and bottom, respectively.

Two dimensional, polar, diagrams of the electric field intensity, $E(\theta, \phi)$, may be plotted by keeping one angular coordinate fixed while varying the other. Conical or azimuth cuts of the radiation pattern are obtained when θ is fixed and ϕ varies from 0 to 360 degrees. In elevation patterns, ϕ is fixed and θ varies from 0 to 360 degrees. Figure 25 illustrates a far field polar plot as drawn by the graphics display program, PATCMP (pattern comparison).

The far field characteristics of an antenna can

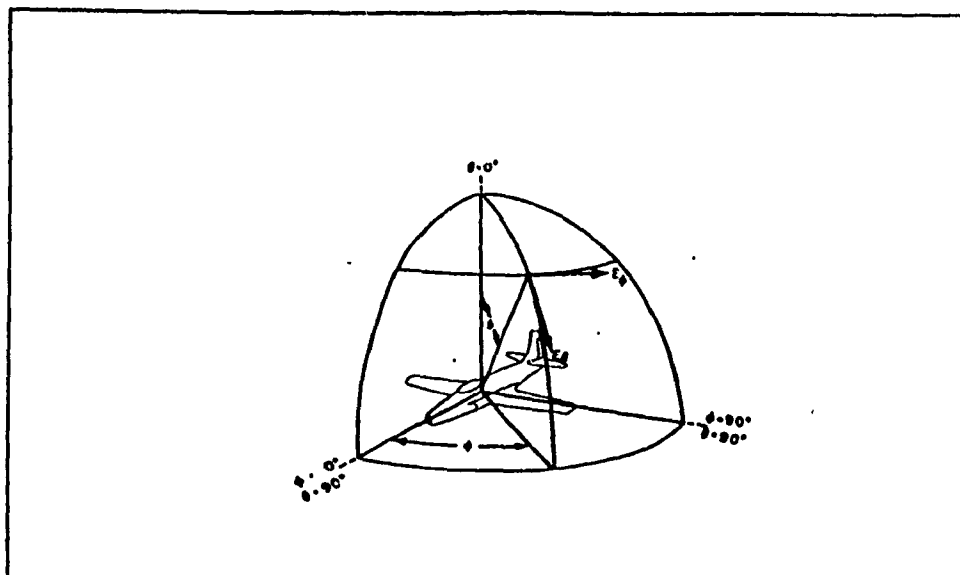


Figure 14 EMC Laboratory Reference Coordinate System

be described by a set of azimuth patterns spanning the theta sector in which communication must be established (Larose). In the EMC laboratory, a series of azimuth patterns from $\theta = 0$ to 180 degrees can be displayed in the form of altitude or colour plots. Examples of altitude graphs are shown in figure 25.

Graphic displays of the current distribution and far field patterns are used for internal as well as external validation of the wire grid model. External checks utilize independent data from other sources (Miller). For example, full scale and scale model pattern measurements are instrumental in assessing solution validity. Comparisons between the measured and computed fields reveal the degree of correlation of the actual structure with its numerical

representation.

To obtain a meaningful graphical comparison requires relative scaling of the measured and computed patterns. The fields are scaled so that they radiate equal amounts of power. The radiated power is computed by program ISOLEV (ISOotropic LEVel) (Bahsoun and Kubina).

4.3. Radiated Power and Isotropic Level

ISOLEV computes the radiated power from the azimuth patterns in the NEC solution file. The power is obtained by taking the closed surface integral of the power density, $S(\theta, \phi)$ over the surface of a sphere of radius 1 meter. The power density is

$$S(\theta, \phi) = \frac{E_{\theta}^2(\theta, \phi) + E_{\phi}^2(\theta, \phi)}{2\eta}$$

and the total radiated power is given by

$$P_r = \int_{\theta=0}^{\pi} \int_{\phi=0}^{2\pi} \frac{E_{\theta}^2(\theta, \phi) + E_{\phi}^2(\theta, \phi)}{2\eta} d\phi \sin\theta d\theta.$$

The radiated power of the antenna under test (AUT) is used to determine a reference or isotropic field level. The isotropic level is an omnidirectional electric field which radiates, in one

polarization, the same amount of power as the AUT.

The power density of the isotropic radiator over a spherical surface of radius 1 meter is

$$S_{iso} = \frac{E_{iso}^2}{2\eta} = \frac{P_r}{4\pi(1)^2}$$

Hence the isotropic field

$$E_{iso} = \sqrt{\frac{\eta P_r}{2\pi}}$$

The isotropic level is used to scale radiation fields for pattern comparison purposes. Program PATCMP scales two patterns so that their isotropic levels coincide, or equivalently, so that their radiated powers are the same.

In addition to the radiated power and isotropic level, ISOLEV calculates the HF aircraft performance parameters. The computation of radiation pattern parameters allow for single-valued assessment of antenna performance at a particular frequency. Consequently, the external validation effort is simplified by plotting and, subsequently, comparing performance criteria versus frequency curves of the actual structure and its corresponding wire grid model.

The HF frequency band is widely used for medium

and long range communications between an aircraft and the ground (Granger). Long distance radio propagation was generally accomplished by ionospheric reflection and is known as the skywave mode of propagation. In general, skywave signals are randomly polarized and, hence, the radiated power must include both the E-theta and E-phi contributions. Furthermore, for adequate communication coverage, HF aircraft antennas should radiate as much power as possible in the 60-120 degree zenith angle range (Bahsoun). The energy distribution requirements of HF antennas is quantified by the radiation pattern efficiency, η_p . This parameter is defined as the ratio of power radiated in both E-theta and E-phi in the solid angle between $\theta = 60$ degrees and $\theta = 120$ degrees (Kubina). Thus,

$$\eta_p = \frac{\int_{\phi=0}^{2\pi} \int_{\theta=\frac{\pi}{3}}^{\frac{2\pi}{3}} (|E_\theta|^2 + |E_\phi|^2) \sin\theta d\theta d\phi}{\int_{\phi=0}^{2\pi} \int_{\theta=0}^{2\pi} (|E_\theta|^2 + |E_\phi|^2) \sin\theta d\theta d\phi} \times 100\%.$$

For medium distances, communication was established via the ground wave (figure 15). The ground wave comprises of the direct, reflected and surface wave.

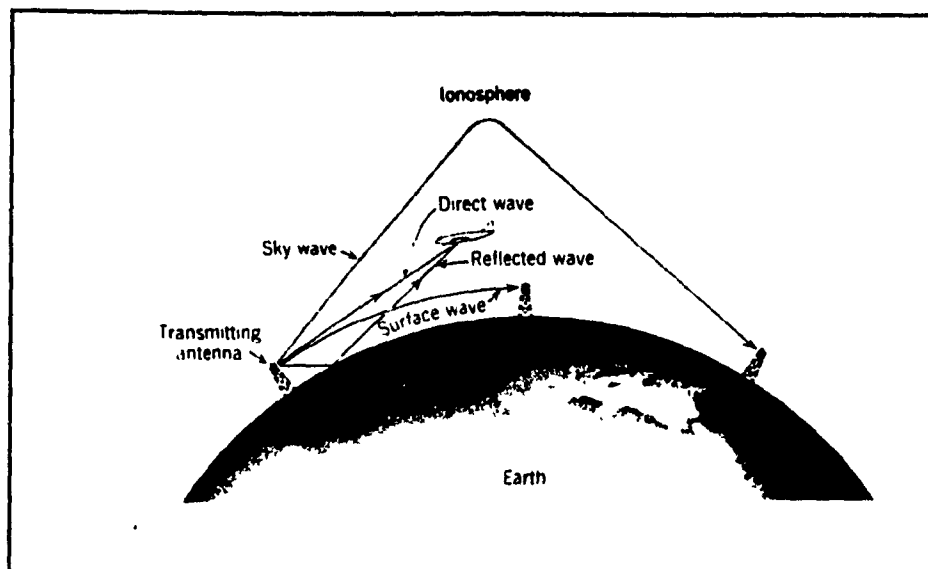


Figure 15 Nomenclature of Wave Propagation (Blake)

In surface wave propagation, the earth tends to guide a wave polarized perpendicularly to it, so that the wavefront remains approximately perpendicular and thus maintains a direction parallel to the surface (Blake). Hence, vertically polarized waves may propagate some distance beyond the line of sight. It is, therefore, desirable to radiate the greatest amount of power in the E-theta component. The $\%E_\theta$ parameter is the ratio of the power radiated in the vertical polarization alone to the total radiated power

$$\%E_\theta = \frac{\int_{\theta=0}^{2\pi} \int_{\phi=0}^{2\pi} |E_\theta|^2 d\phi \sin\theta d\theta}{\int_{\theta=0}^{2\pi} \int_{\phi=0}^{2\pi} (|E_\theta|^2 + |E_\phi|^2) d\phi \sin\theta d\theta} \times 100\%.$$

The last HF assessment parameter combines the two aforementioned requirements of power contained in the vertical component and radiated in the $\theta=60$ to 120 degree angular sector. The 'useful' %E- θ parameter is given by

$$SUB-\%E_{\theta} = \frac{\int_{\theta=\frac{\pi}{3}}^{\frac{2\pi}{3}} \int_{\phi=0}^{2\pi} E_{\theta}^2 d\phi \sin\theta d\theta}{\int_{\theta=0}^{2\pi} \int_{\phi=0}^{2\pi} (E_{\theta}^2 + E_{\phi}^2) d\phi \sin\theta d\theta} \times 100\%.$$

CHAPTER 5

EC-130 HF ANTENNA INSTALLATION

The EC-130 Tacamo is the United States Air Force high-wing, all metal monoplane. Its Canadian counterpart is the C130 Hercules aircraft. The Tacamo is equipped with five HF external wire antennas for long range communication. The HF complement consists of two flat top antennas that run from either side of the fuselage to the vertical stabilizer, two symmetrical dogleg antennas and one near-central receive antenna (figure 16).

The basic installation of each antenna is the

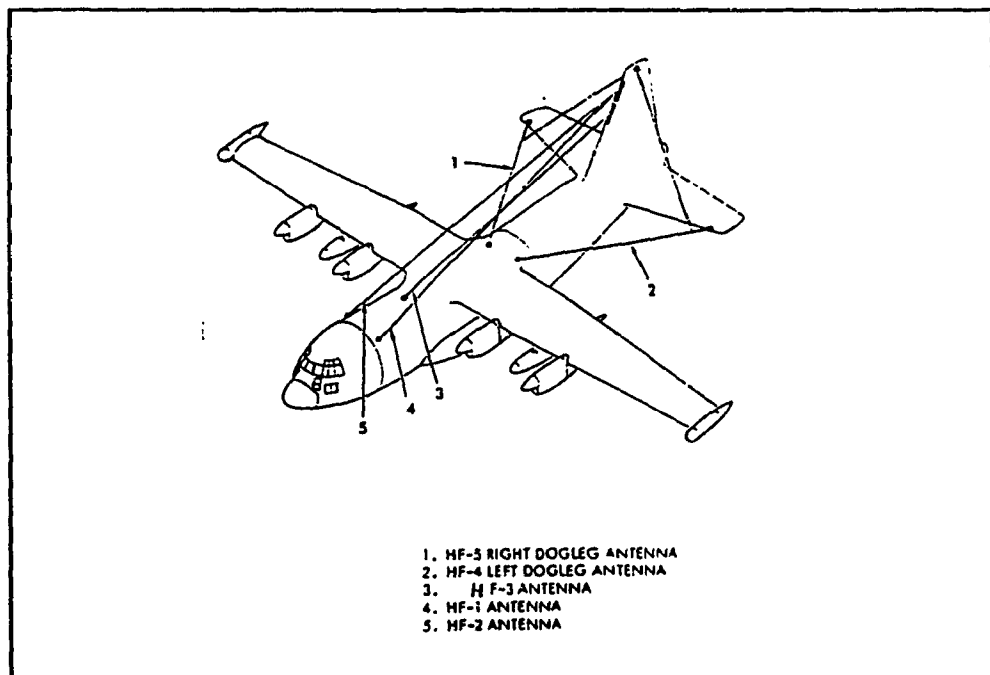


Figure 16 EC-130 Tacamo

same. Each external wire extends from the mast a forward attaching point of the antenna to the fuselage. The wire runs between the mast and the strain insulator which serves as an electrical termination point for the antenna. The aft end of the wire is mechanically anchored to the (vertical/horizontal) stabilizer by a tension take-up unit.

As illustrated in figure 17, HF1 is connected between the vertical stabilizer and the upper port side of the fuselage at station 267. The wire antenna is displaced 1.168 meters left of center. HF2 similarly extends from fuselage station 267 to the vertical stabilizer, however, it is displaced 0.940 meters to the right. The forward attaching point of external wire HF3 is at fuselage station 473 and 0.254 meters to the right of center. The HF4 external wire is connected to the port mast at station 681 and runs to the horizontal, then to the vertical stabilizer. HF5 is the starboard image of antenna HF4.

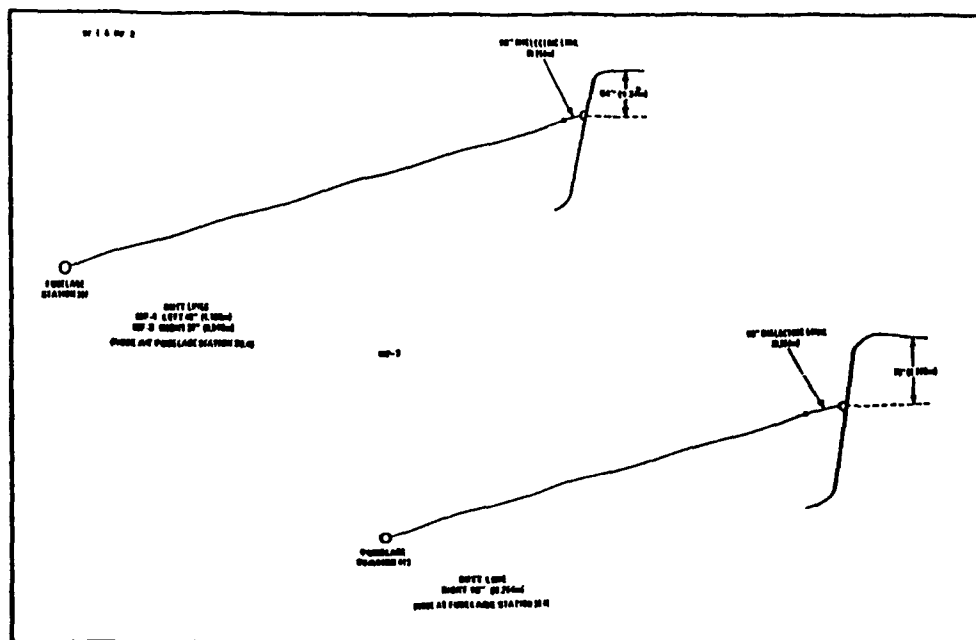


Figure 17 EC-130 HF Antenna Installation

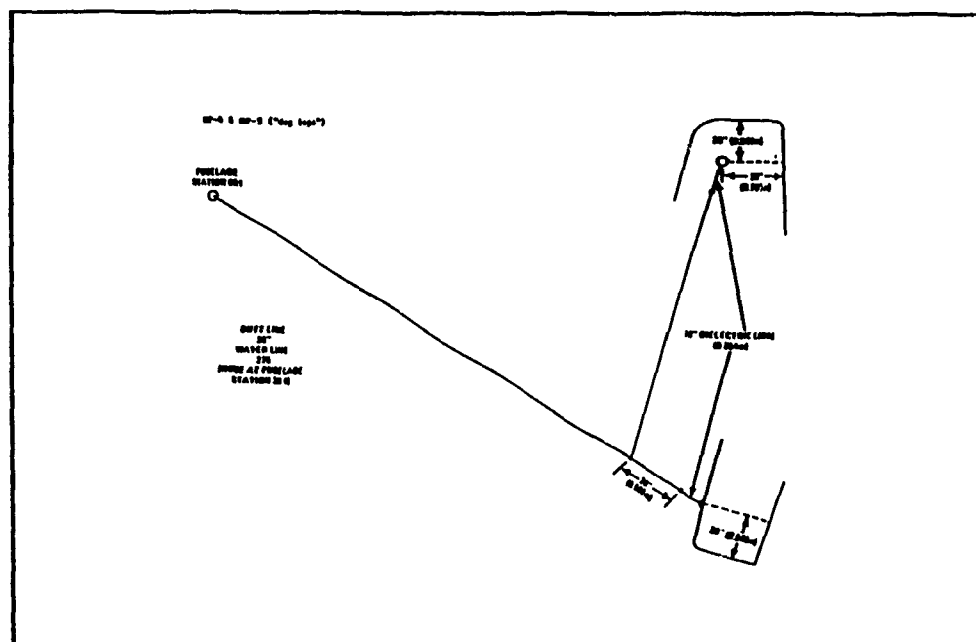


Figure 18 EC-130 HF Installation

5.1. Measurements

5.1.1. Scale Model

Radiation patterns were measured on a scale model of the EC-130 airframe/HF antenna system. The tests were conducted at the Naval Air Development Center in Warminster, Pennsylvania and the results are outlined in NATC report no. SY-11R-84.

The scale model is constructed of fiberglass and coated with copper. Its dimensions are 1/100 times those of the Tacamo prototype. Thus, the HF band of 2 to 30 MHz was increased accordingly to a working frequency of 200 to 3000 MHz. The measurements were conducted in a pyramidal anechoic chamber designed to operate in the 125 MHz to 40 GHz range.

Two EC-130 scale models were used for measuring the antenna radiation patterns. At frequencies below 500 MHz, a model containing miniature oscillators and batteries was tested under transmitting conditions. Alternatively, the second model was examined under receiving conditions for frequencies 500 through and including 3000 MHz. This scale model was drilled to permit the use of cables running between the antenna feed locations and the receiver.

The radiation patterns of antennas HF1, HF3 and HF4 were measured. Antennas HF2 and HF5 were not tested because of their respective symmetry with HF1

and HF4. Although HF1 and HF2 are not exact images, their roll off from top center of the 1/100 scale model differs by a mere 0.09 inches.

E-theta and E-phi polarization patterns were measured 360 degrees in azimuth for each elevation angle from 0 to 155 degrees in increments of 5 degrees. The test frequencies covered the complete HF frequency range at scale frequencies corresponding to 2.13, 4.04, 8.00, 11.00, 14.00, 17.00, 20.00, 23.00, 26.00 and 30.00 MHz.

At the EMC Laboratory in Concordia University, the scale model radiation patterns were interpolated and extrapolated to generate conical cuts in accordance with military standard MIL-A-9080. The military specifications require the three principal plane patterns and a set of azimuth patterns at theta = 0, 25, 37, 45, 53, 60, 66, 72, 78, 84, 96, 102, 108, 114, 120, 127, 135, 143, 155 and 180 degrees for both vertical and horizontal E-field polarizations. HF system performance parameters were derived for the EC-130 scale model.

5.1.2. Full Scale

In addition to the scale model measurements, full scale airborne testing of the EC-130 airframe-antenna installation was undertaken. Far field patterns of

the Tacamo HF antenna system were measured by utilizing the Antenna Testing Laboratory Automated System in Chesapeake Bay, Maryland. The NATC provided the H-plane patterns for both E-theta and E-phi polarizations of antennas HF1 and HF4 at the following frequencies: 4.00, 8.00, 14.00, 20.00, and 26.00 MHz.

The electric fields, displayed in Appendix A, reveal discrepancies between the full scale and scale model radiation pattern measurements. Pattern shape, alignment, lobe number, magnitude of vertical and horizontal polarizations and relative E-theta and E-phi levels are considered when comparing electric field plots.

Notable inconsistencies which occur when exciting antenna HF1 are mentioned below. At 4 MHz, the scale model E-theta polarization is cardioid-shaped whereas the full scale pattern is omnidirectional. The forward bell-shaped lobe of the scale model at 8 MHz is not evident in its full scale E-theta counterpart. Lobe inequalities exist between the scale model and full scale patterns in both polarizations at an operating frequency of 14 MHz. At higher frequencies, close attention must be paid to differences in magnitude and pattern alignment.

Discrepancies in the HF4 principal plane patterns consist of magnitude level and field shape variations.

In particular, distinct nulls are apparent in scale model E-phi plots at 8.00, 14.00, 20.00, and 26.00 MHz. However, the nulls are not nearly as well defined in the full scale patterns. In addition, there is a severe deviation in the relative E-theta and E-phi levels at 4.00 MHz.

The inconsistencies in radiation pattern measurements led to the development of a computer model. The computed electric fields serve to qualify the full scale and scale model HF antenna patterns.

In general, the validity of a numerical model is assessed by comparing the computed radiation patterns with the measured patterns. However, in this project, the reliability of the available measurement data is questionable. Therefore, only incremental perturbations in model development were effectuated.

5.2. Wire Grid Model Generation - Base Model F

The thrust of the computer simulation technique is to develop a model which is electromagnetically equivalent to the actual structure. An electromagnetically equivalent wire grid representation supports a current distribution which approaches that of the corresponding continuous surface. Thus, the wire mesh configuration is dictated by local variations in the surface geometry

and surface current density.

As stated in chapter 2, the wire grid should consist of segments near-equal in length. The segmentation is such that the wire lengths are 0.2λ at 30 MHz. In addition, the number of segments is the minimum possible to reduce computing time whilst upholding the aforementioned requirements.

Effectively, the EC-130 mesh is divided into near-uniform quadrilateral sections spanning a maximum of $(0.2(c/f))^2 = 4m^2$. Triangular and pentagonal grids of wires are also used to model complex surface geometry.

A layout of the wire grid was prepared on the aircraft's plans for digitization. The main portion of the fuselage consists of octagonal cross sections positioned so as to coincide with the feed location of each HF antenna. The octagons give way to diamond-shaped sections as the aft of the fuselage gradually slopes upwards. Longitudinal wires divide the fuselage into rectangular grids. The wings and stabilizers are plane surfaces and the model wheel wells approximate those of the actual aircraft.

Soon after completing the model digitization, more detailed drawings of the airframe became available. Water line, butt line and fuselage station coordinates were entered manually via DIDEK resulting

in a cleaner, crisper wire-grid representation. In addition, all five HF long wire antennas were connected in accordance with the NATC specifications.

The same surface area rule of thumb was used to calculate the radii of the airframe wires. The model antenna wires are 0.002 meters in diameter.

Wire radii and segmentation were changed in some instances in order to remove all junction incompatibilities. Only individual seg/wav errors remained at high frequencies. Since the wires exceeded the upper limit of 2 meters by a minimal amount, and subdividing the wires would substantially increase the number of segments, seg/wav errors were tolerated. The resulting EC-130 wire grid model contains a total of 405 segments and is entitled base model F (figures 19 and 20).

The excitation at the antenna terminals is a voltage source of 1 volt magnitude and 0 degrees phase. NEC requires a feed element segment at the voltage source location so that the required potential drop can be specified as a boundary condition (Burke and Poggio).

As in the case of the scale model measurements, antennas HF1, HF3 and HF4 are tested in turn. Thus, at each frequency, three NEC input files differing only in the location of the feed element segment are

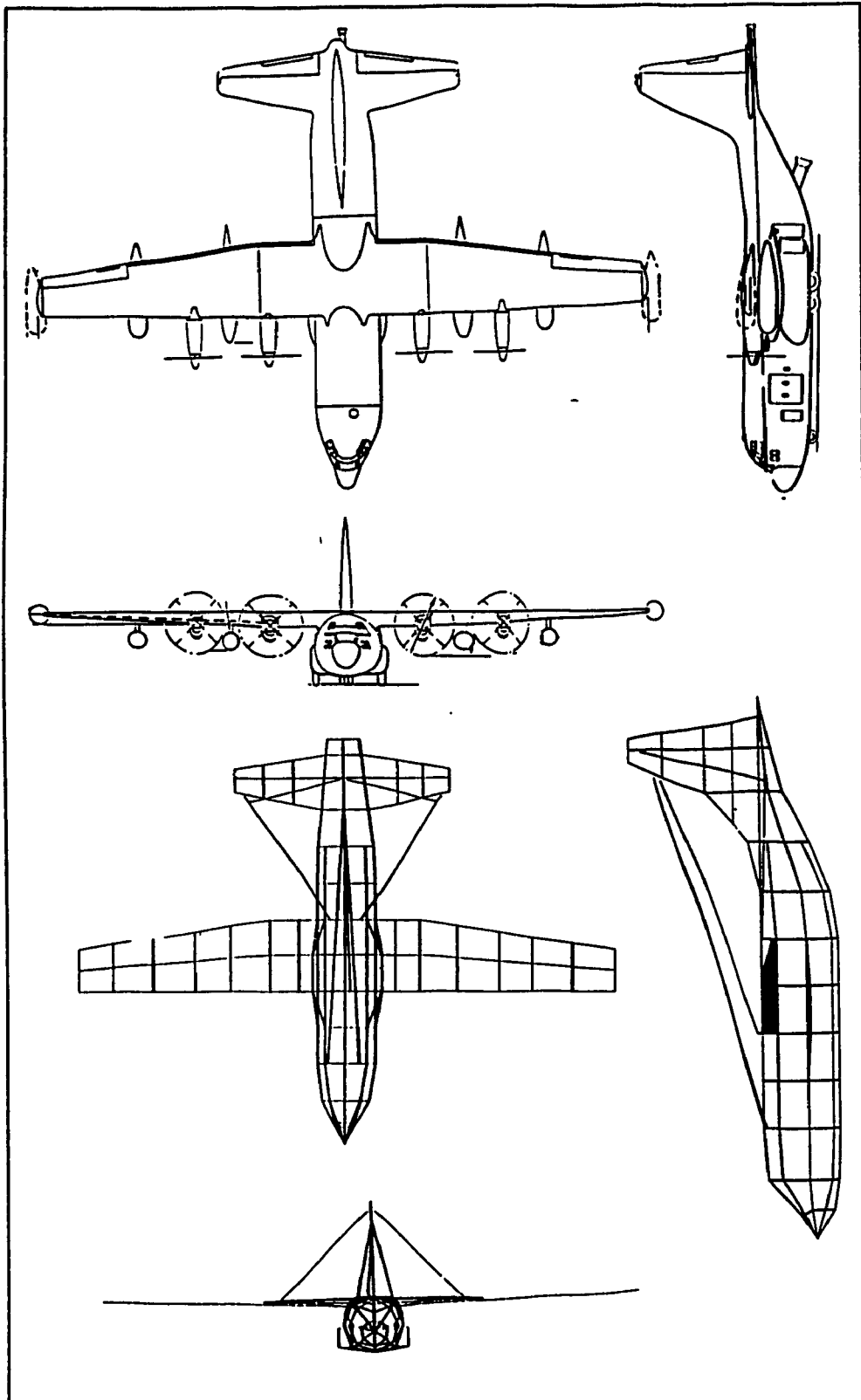


Figure 19 EC-130 Aircraft

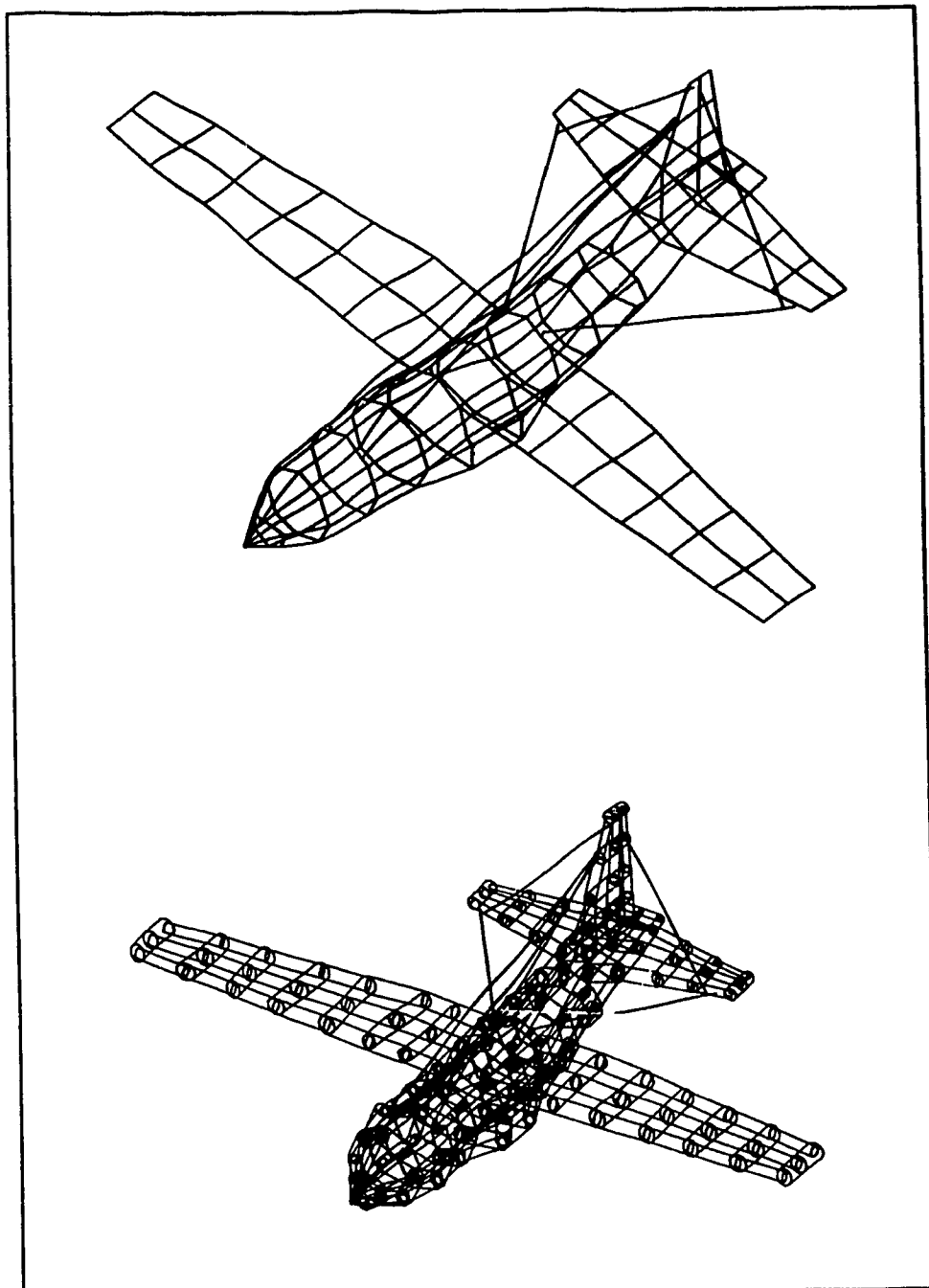


Figure 20 EC-130 Base Model F

required. Because the model geometry is fixed, the impedance matrix $[G]$ remains constant for all three excitations. With the Numerical Green Function (NGF) option in NEC, the impedance matrix is extracted from

the output of the first NEC run and stored for the remaining two executions. The elements of the voltage matrix [E] are rearranged according to the location of the excitation source and the currents are solved in each case. The NGF feature reduces the CPU time used by a factor of N^2 where N is the number of segments (Stutzman and Thiele).

5.2.1. Current Distribution

A transmitting system will operate at maximum efficiency when the aircraft antenna system provides an input impedance that will match the transmitter impedance. The antenna impedance curve is influenced by the electromagnetically coupled currents that exist on the wires of the model. In particular, strong currents that flow along resonant paths will significantly affect the input impedance. Granger defines six current modes on the airframe (figure 21). The resonances of these modes occur when the lengths of the current paths are equal to an integral multiple of $\lambda/2$.

The current on HF1 at 4.04 MHz is predominant along the wire antenna and couples into antenna HF3 (figure 22). In addition, the spurious current at the tip of the vertical stabilizer exemplifies a NEC limitation in which large circulating currents are

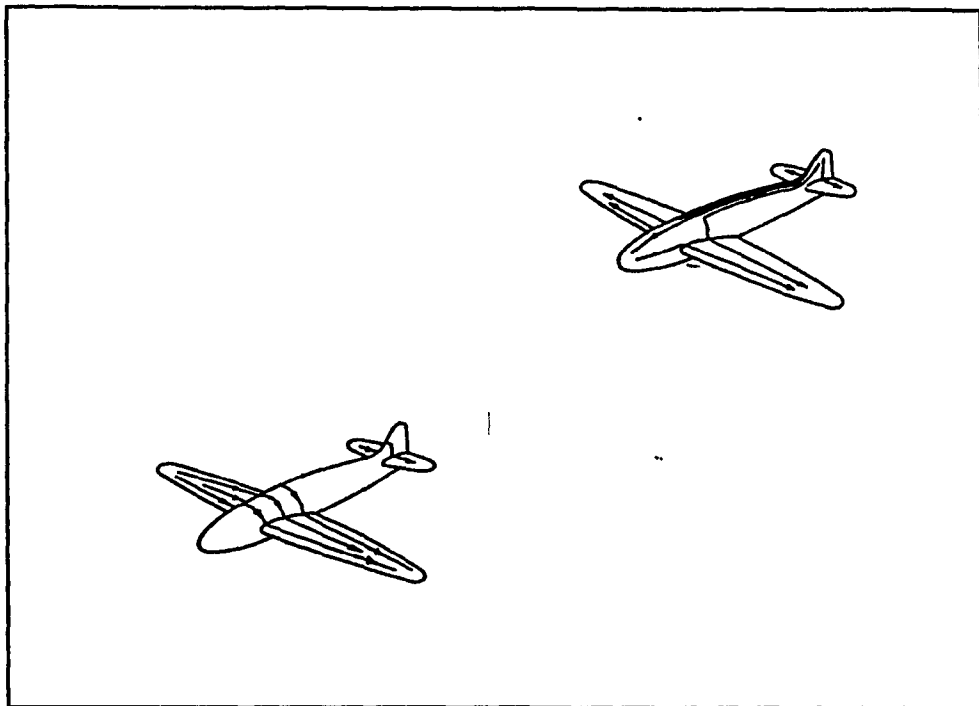


Figure 21 Resonant Current Modes on Airframe
(Granger)

found to occur on the interior loops of wire grids (Mittra).

The HF3 wire antenna extends along the near-central longitudinal axis of the aircraft. Consequently, the excitation of HF3 results in an even distribution of current about the central axis of the fuselage (figure 23). The computed radiation patterns are ,predictably, symmetrical.

Figure 24 shows a colour plot of the amplitude of the current distribution when the HF4 dogleg is the antenna under test. The current magnitude is highest along its horizontal wire. Currents are weakly coupled into the port side of the fuselage, the

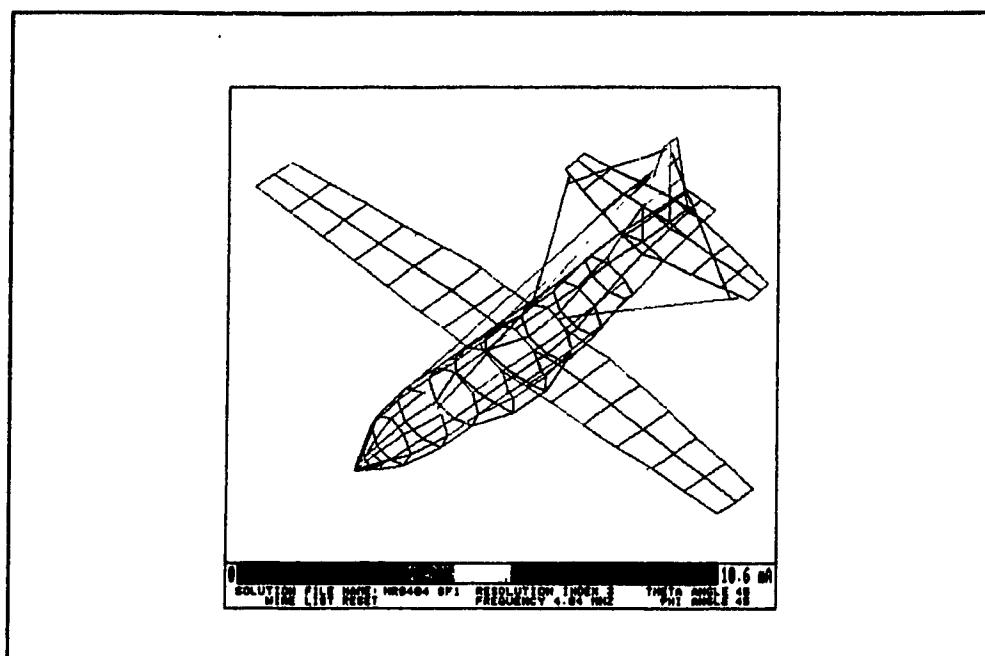


Figure 22 Currents on Model F at 4.04 MHz - HF1

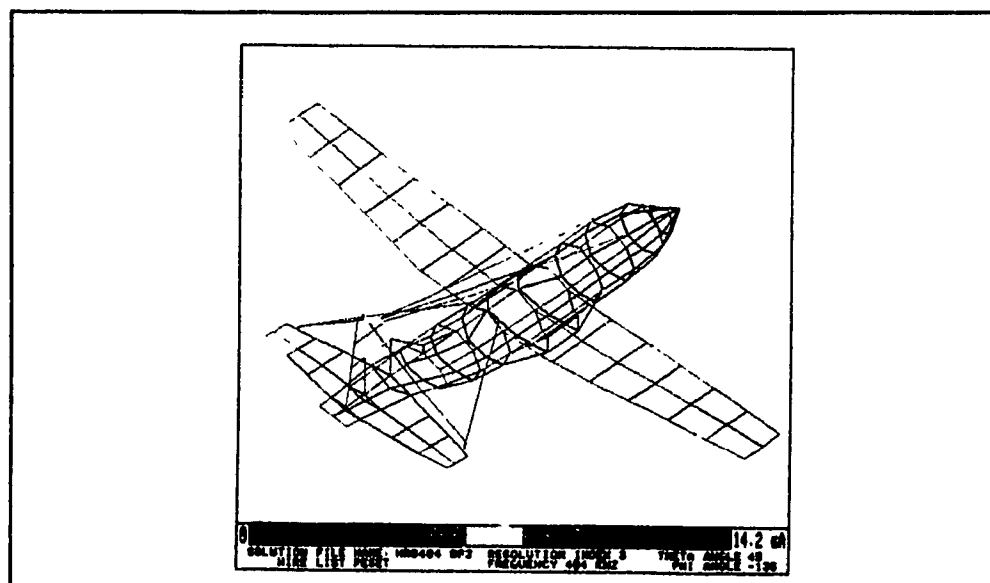


Figure 23 Current Distribution on Model F at 4.04 MHz - HF3

forward edge of the horizontal stabilizer, and the aft edge of the left wing.

In this case, the fixed wire is poorly coupled to the current modes of the airframe. Thus, the input

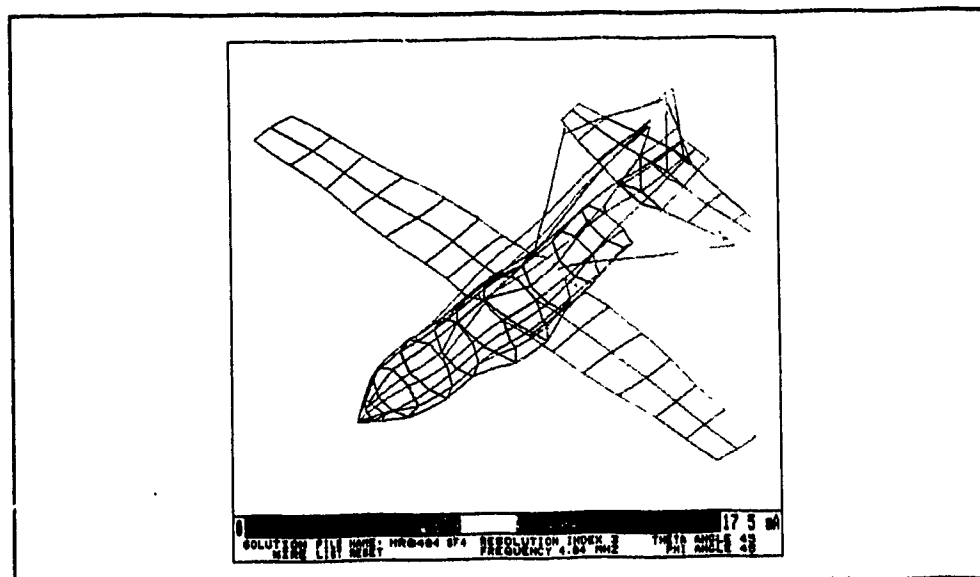


Figure 24 Currents on Model F at 4.04 MHz - HF4

impedance of the antennas are not substantially affected by the current modes.

5.2.2 Radiation Patterns

5.2.2.1. Computed/Scale Model

To begin, the radiation patterns of antennas HF1, HF3 and HF4 were computed at a frequency of 4.04 MHz. As illustrated in figure 25, the computed patterns of antenna HF1 closely track the corresponding scale model measurements. The only notable difference is the occurrence of a shift in the cardioid of the measured E-theta azimuth pattern. In contrast, the computed cardioid pattern is symmetrical about the antenna.

The HF3 radiated fields of the EC-130 numerical model shows reasonably good agreement with the experimental measurements (figure 26).

The gradual variation in the shapes of the computed E-theta patterns parallel those of the scale model patterns through out most of the complement of conical cuts. However, there exist some differences in magnitude levels. Both the computed and measured E-phi polarizations are figure eight patterns with minima forward and aft of the aircraft.

The computed radiation patterns of antenna HF4 resulted in some agreement with the measurement data (figure 27). The computed E-phi polarization reproduces the tilted, two-lobed scale model pattern. However, the computed E-theta pattern continuously

exhibits deeper nulls and degrades considerably in the $\theta = 66$ degrees to 96 degrees range.

The initial modelling effort resulted in a credible model at 4.04 MHz for antennas HF1, HF3 and HF4. Radiation patterns were obtained at sample frequencies of 8.00, 14.00 and 23.00 MHz to test the performance of base model F over the HF band.

There is some agreement between the computed and scale model fields of antenna HF1 at 8.00 MHz. However, there exist differences in the shape of the E- θ polarization pattern. This is evident in the azimuth pattern where the forward lobe of the measured E- θ component is bell-shaped and its computed counterpart is approximately circular (figure 28). The azimuth plane pattern also clearly shows the presence of a deeper null in the computed E- ϕ polarization at the forward location. The pattern agreement for antennas HF3 and HF4 has also degraded since increasing the operating frequency from 4.04 to 8.00 MHz (figure 29).

The agreement is very good at 14.00 MHz for antennas HF1, HF3 and HF4 (figure 30). The only apparent anomaly is the presence of two extra small lobes in the computed E- ϕ polarization of antenna HF3. At 23.00 MHz, the computed patterns closely reproduce the measured data HF1, HF3 and HF4. The

entire set of radiation patterns is displayed at 23.00 MHz in the altitude plots of figure 31.

The degradation in pattern agreement at 8.00 MHz was initially attributed to an increase in seg/wav incompatibilities. However, the computed fields closely approximate the experimental measurements at the operating frequencies of 14.00 and 23.00 MHz. This implies that the main electrical consideration of segment length relative to the wavelength has been sufficiently satisfied.

5.2.2.2. Computed/Full Scale

Full scale azimuth patterns for antennas HF1 and HF4 of the EC-130 aircraft were provided by NATC. At 4.0 MHz¹, the HF1 E-theta polarization is a frayed circular pattern whereas, at 4.04 MHz, the computed E-theta field is a forward-directed cardioid (figure 32). The measured E-phi polarization consist of two lobes with minima in the forward-starboard and port-aft directions. The computed E-phi also comprises of two lobes, however, the minima are forward and aft of the aircraft. For antenna HF4, the measured E-theta pattern is near-omnidirectional and the measured E-phi polarization is rounded with a null in the forward location (figure 33). The computed E-theta and E-phi patterns of antenna HF4 are illustrated in figure 27

¹ Computed pattern at 4.04 MHz compared to Full Scale at 4.0 MHz (due to limited availability of full scale - 4, 8, 14, 20 & 26 MHz)

and show poor pattern agreement with the full scale measurements.

To approximate the in-flight test environment, a perfect ground plane was included in the computer model simulation. As expected, the computed currents on the wire grid aircraft 5000 feet above the ground are identical to the current in the free-space model since reflection coefficient analysis rather than method of moments is incorporated.

The radiated field is the superposition of the source model and image fields. The resultant computed E-theta polarization of antenna HF1 remains a cardioid (figure 34). The E-theta pattern of antenna HF4 for the above ground case is illustrated in figure 35. At the azimuth, E-phi is simply the tangential component of the electric field at the interface of free space and perfect ground. Therefore, boundary conditions dictate that

$$E_{tan}=E_{phi}=0.$$

The EC-130 base model patterns more closely follow the scale model than full scale measurements. Model F remains stable throughout the HF band as illustrated by the pattern agreement at frequencies as low as 4.04 MHz and as high as 23.00 MHz. However, discrepancies persist, particularly at 8.00 MHz.

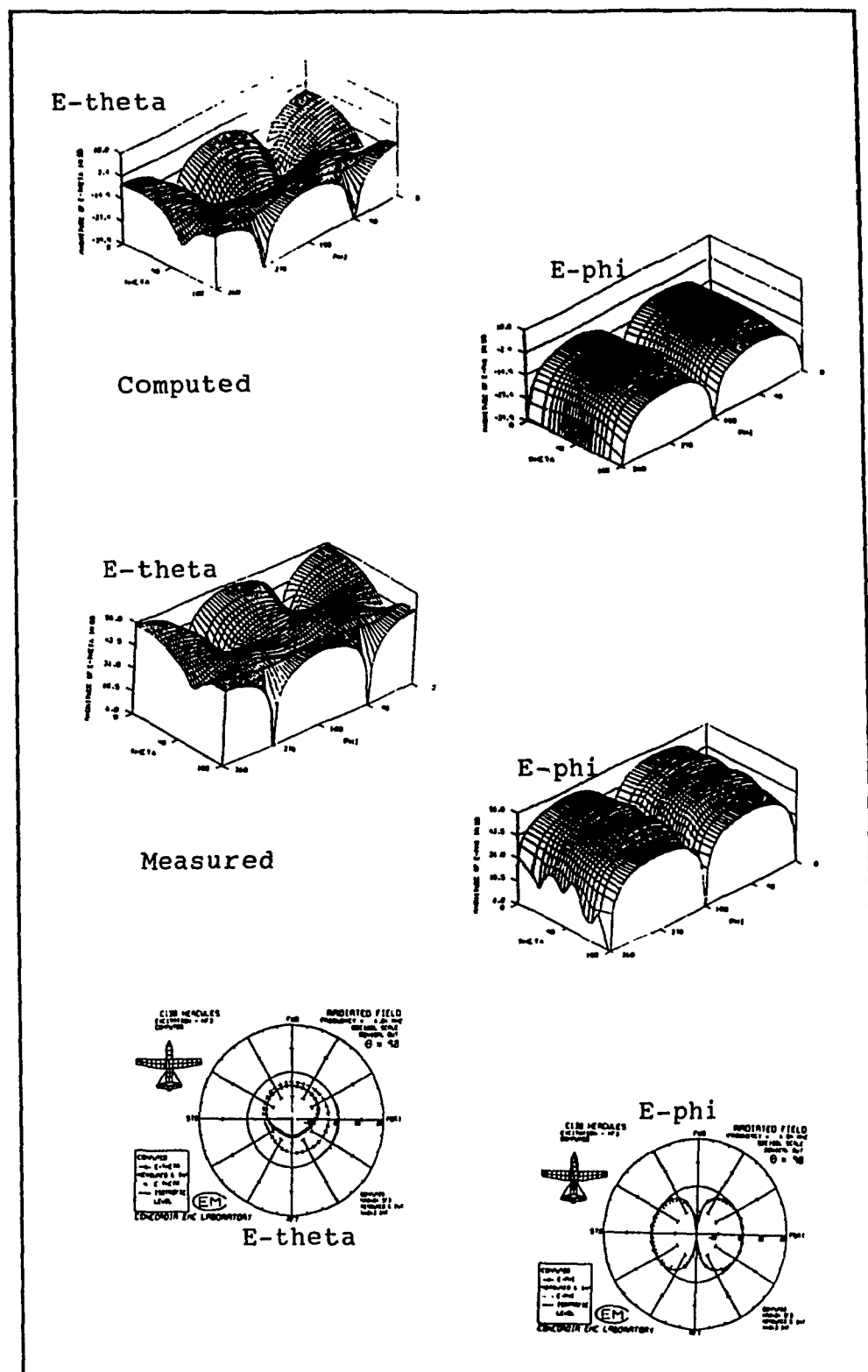


Figure 26 HF3 - Wire Grid Base Model Radiation Patterns versus Scale Model Measurements at 4.04 MHz

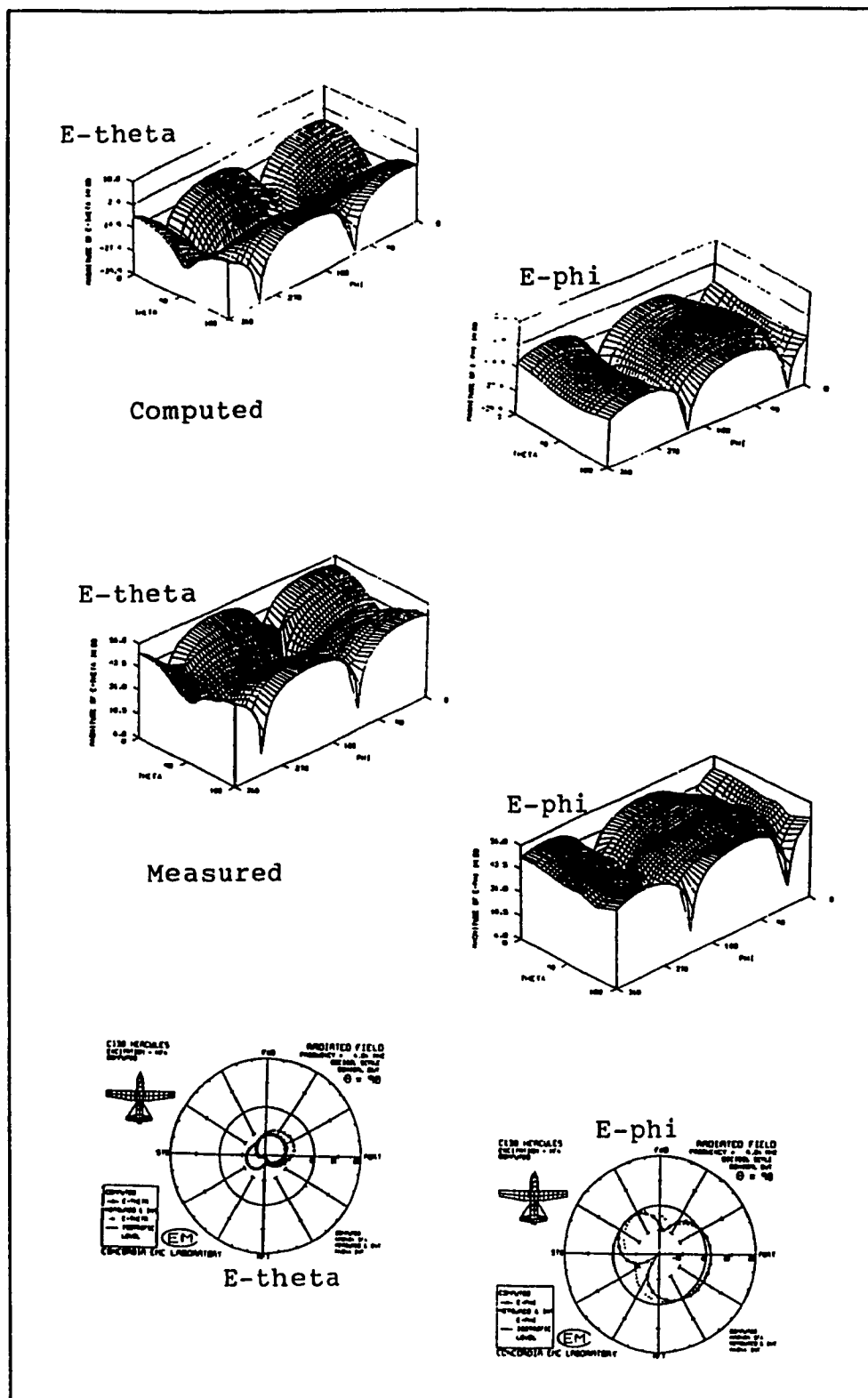


Figure 27 HF4 - Wire Grid Base Model Radiation Patterns versus Scale Model Measurements at 4.04 MHz

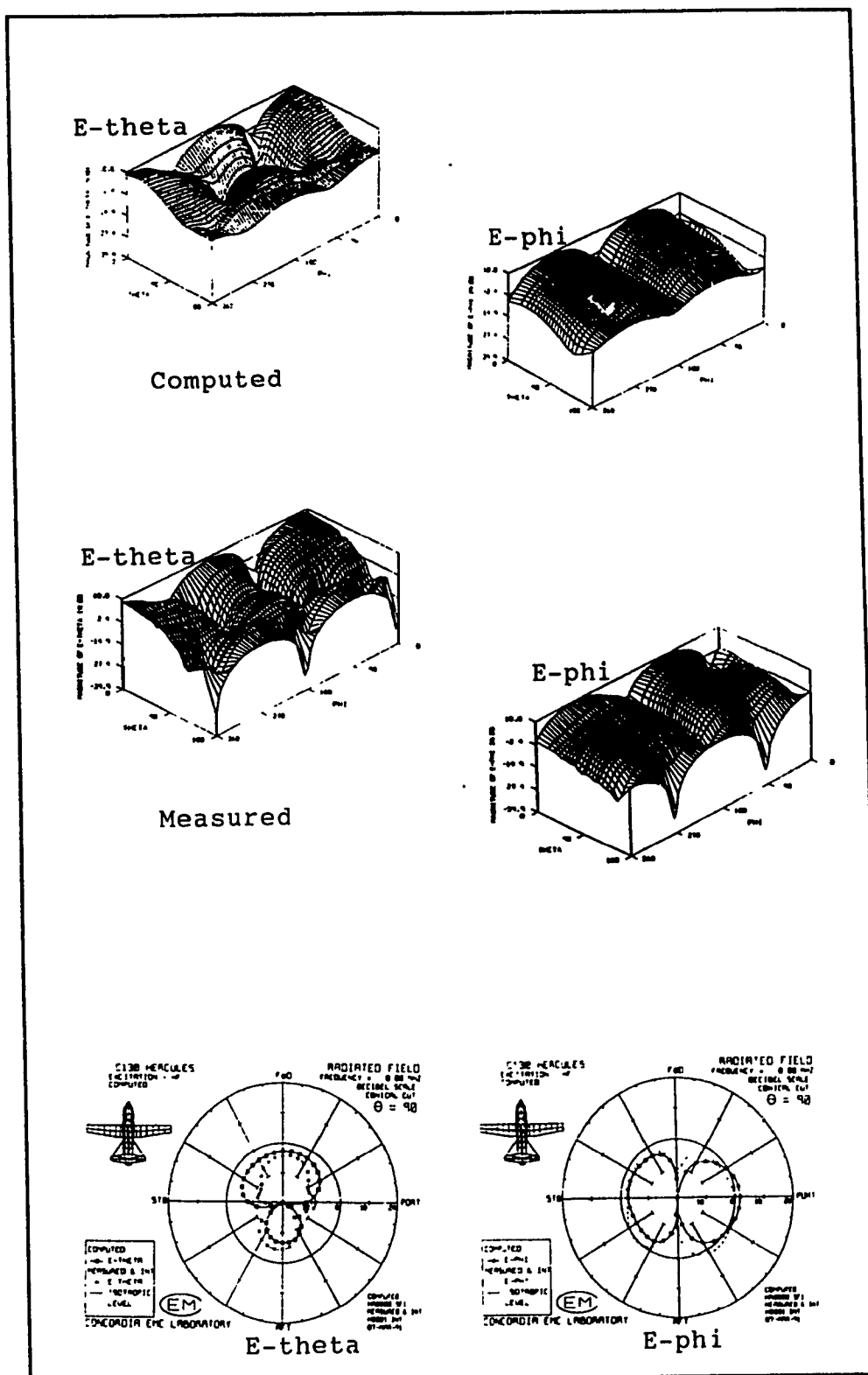


Figure 28 HF1 - Radiation Patterns for Base Model F versus Scale Model Measurements at 8.00 MHz

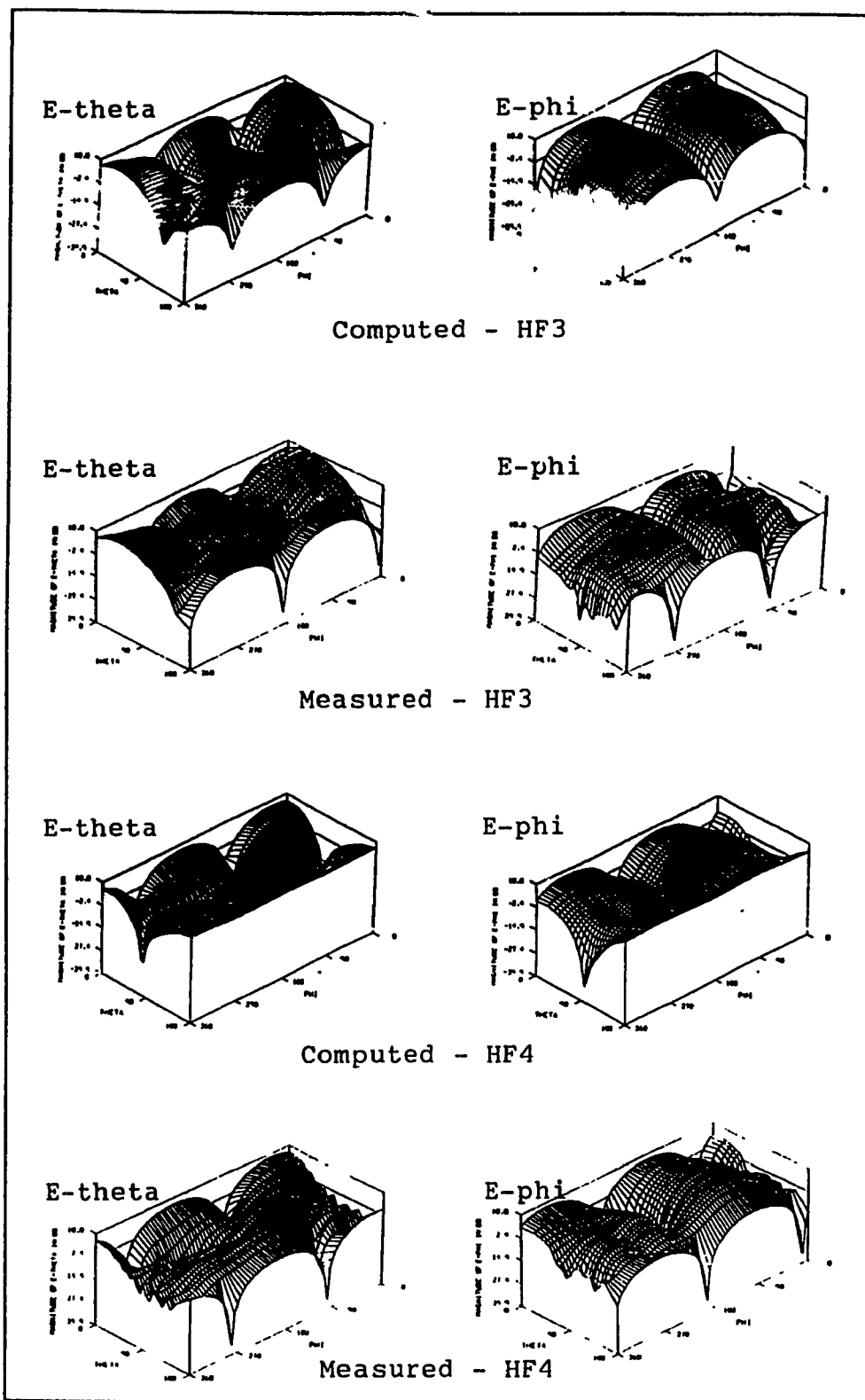


Figure 29 HF3 & HF4 - Base Model F Radiation Patterns at 8.00 MHz

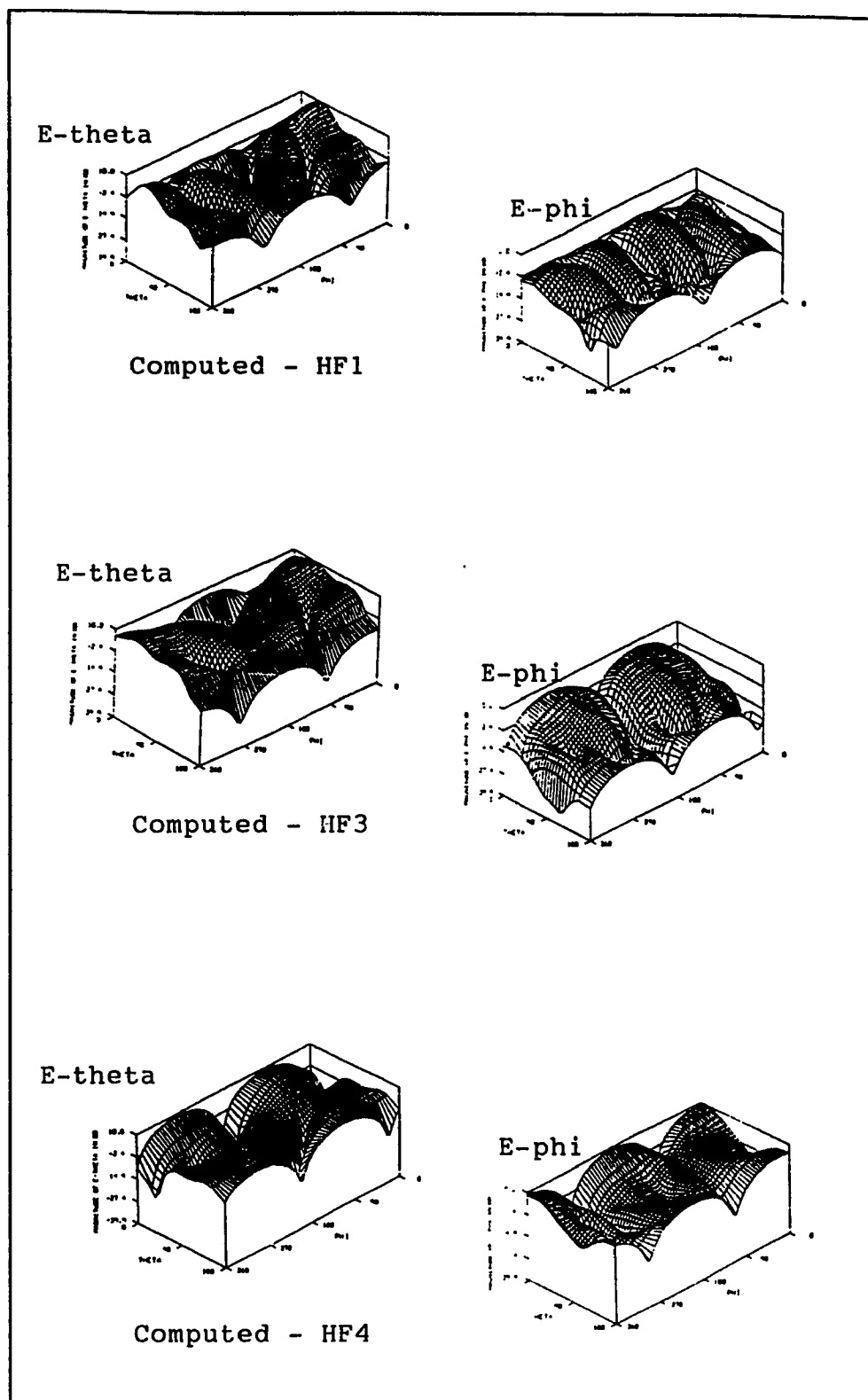
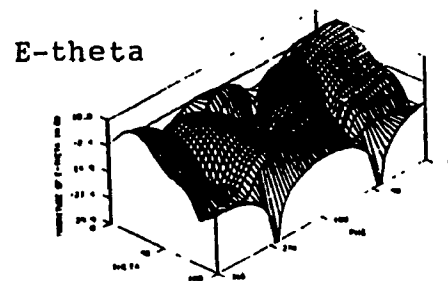
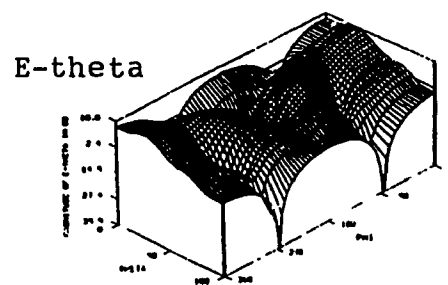
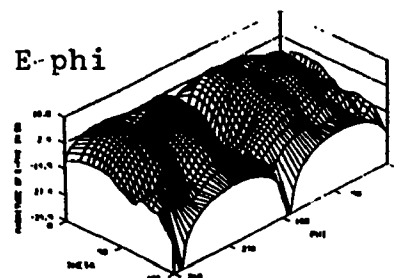


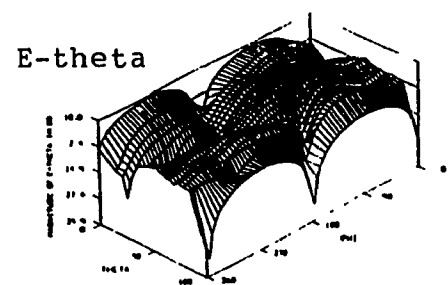
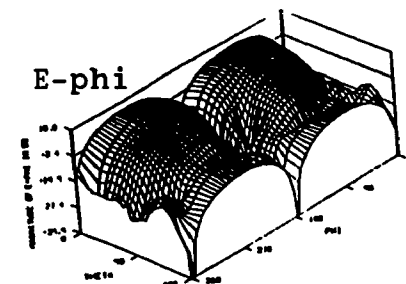
Figure 30 Base Model F at 14.00 MHz for excitation HF1, HF3 & HF4 versus Scale Model Measurements



Measured - HF1



Measured - HF3



Measured - HF4

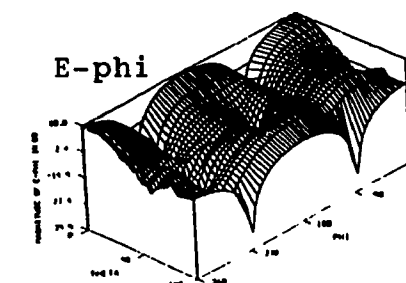


Figure 30 Continued

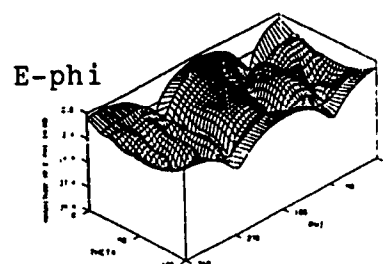
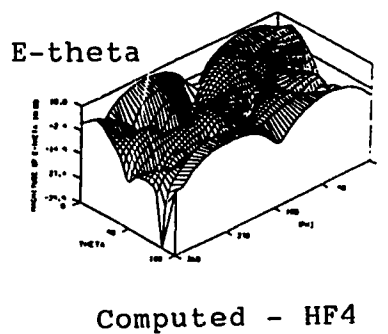
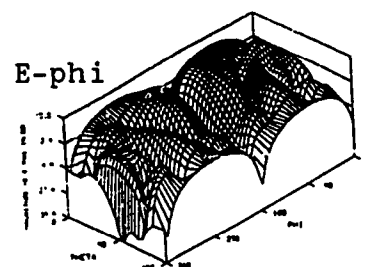
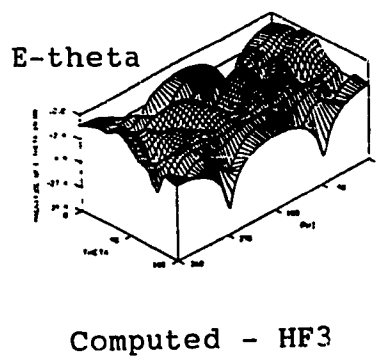
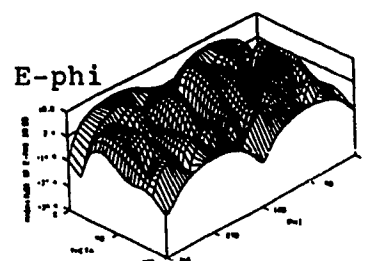
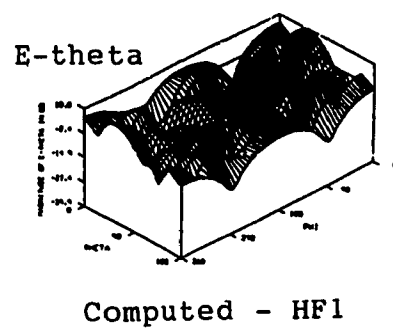
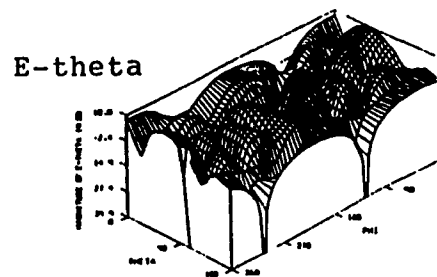
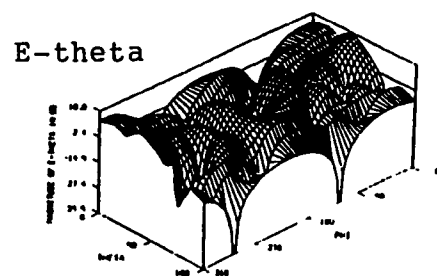
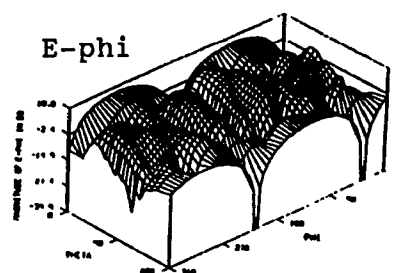


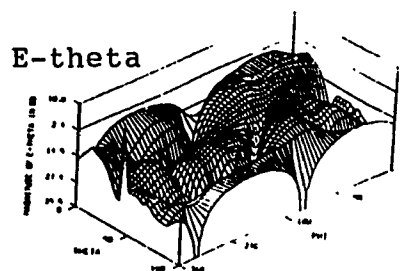
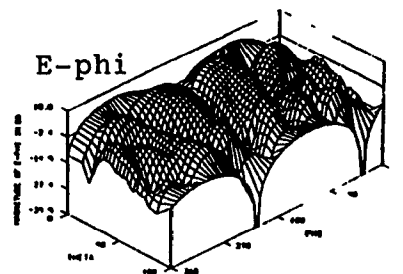
Figure 31 Base Model F at 23.00 MHz for excitation HF1, HF3 & HF4 versus Scale Model Measurements



Measured - HF1



Measured - HF3



Measured - HF4

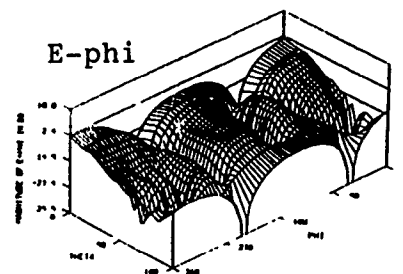


Figure 31 Continued

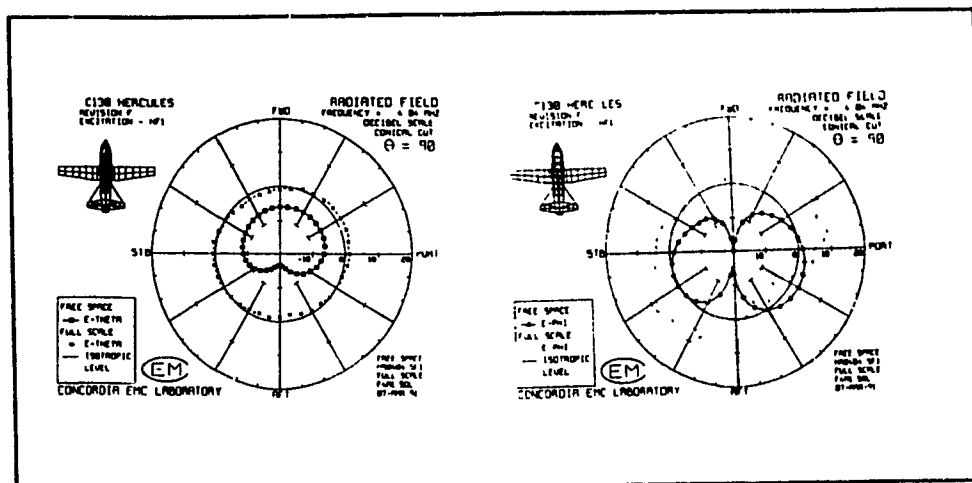


Figure 32 HF1 - Base Model F Azimuth Plane Pattern versus Full Scale Measurements

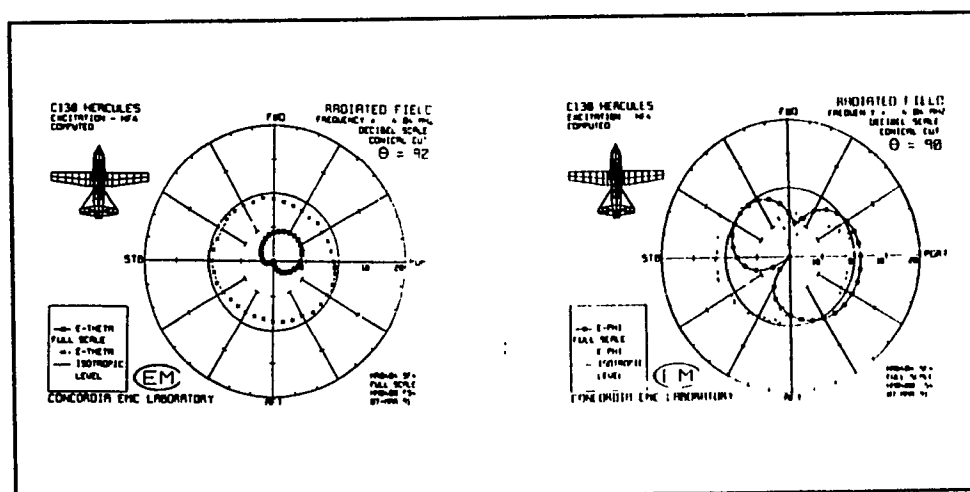


Figure 33 HF4 - Base Model F Azimuth Plane Pattern versus Full Scale Measurements

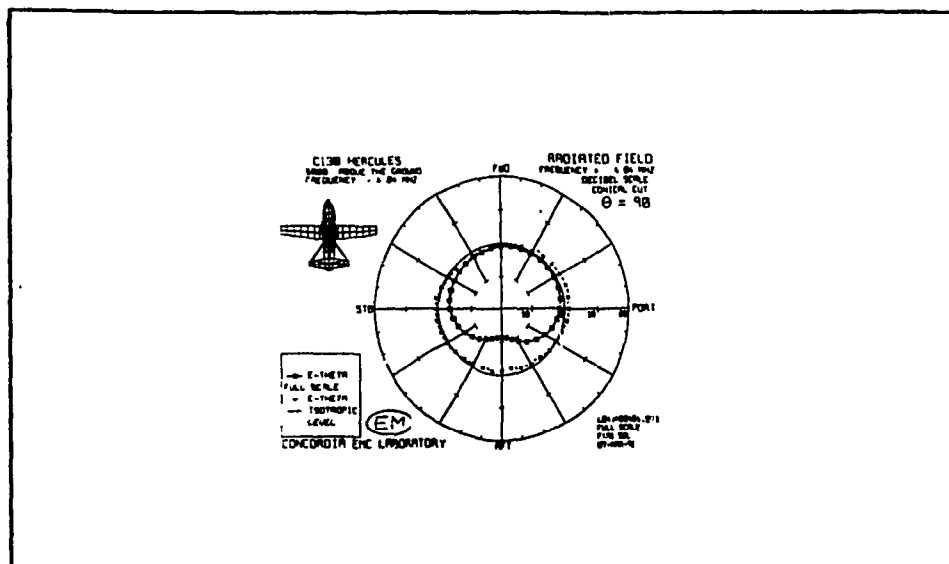


Figure 34 HF1 - Base Model F Above Perfect Ground versus Full Scale Measurements

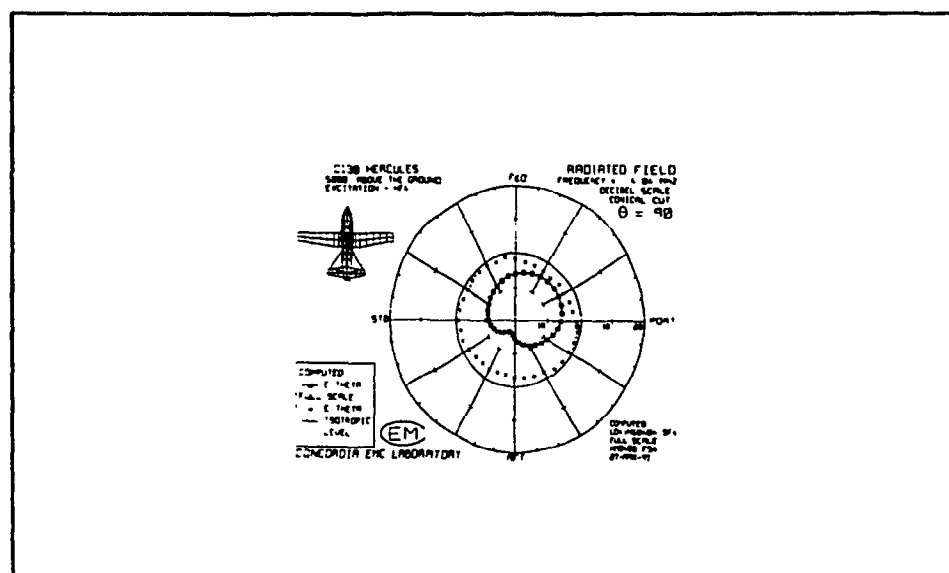


Figure 35 HF4 - Base Model F Above Perfect Ground versus Full Scale Measurements

5.3. Geometrical Perturbations

At this point, incremental perturbations in wire-grid topology were effectuated to assess model stability. Segmentation, radii selection and impedance loading are fundamental to the model development process.

5.3.1. Segmentation

To achieve electromagnetic equivalence, the wire grid should support a current distribution which approximates that on the corresponding surface. Therefore, optimal segmentation of a model would incorporate finer mesh where larger currents might be expected to flow. More wires were added in the feed element regions of the airframe to account for current flow outward and around the antenna source segment. Models G, H and I were derived from base model F by providing a denser grid around the feed points.

Wires were added around the feed elements of antennas HF1 through HF5 augmenting the total number of segments to 476 for model G. Soon after, the HF3 feed region grid was reflected onto the port side to maintain airframe symmetry. The resulting model H contains 486 segments. Revision I called for the addition of four cross wires connected to the source segment of antenna HF2. Figures 36-38 illustrate the levels of model refinement. The current distribution

and radiation patterns of antennas HF1, HF3 and HF4 were computed at an operating frequency of 4.04 MHz. Models G, H and I conform to NEC guidelines on segment length, radius and interconnections at 4.04 MHz.

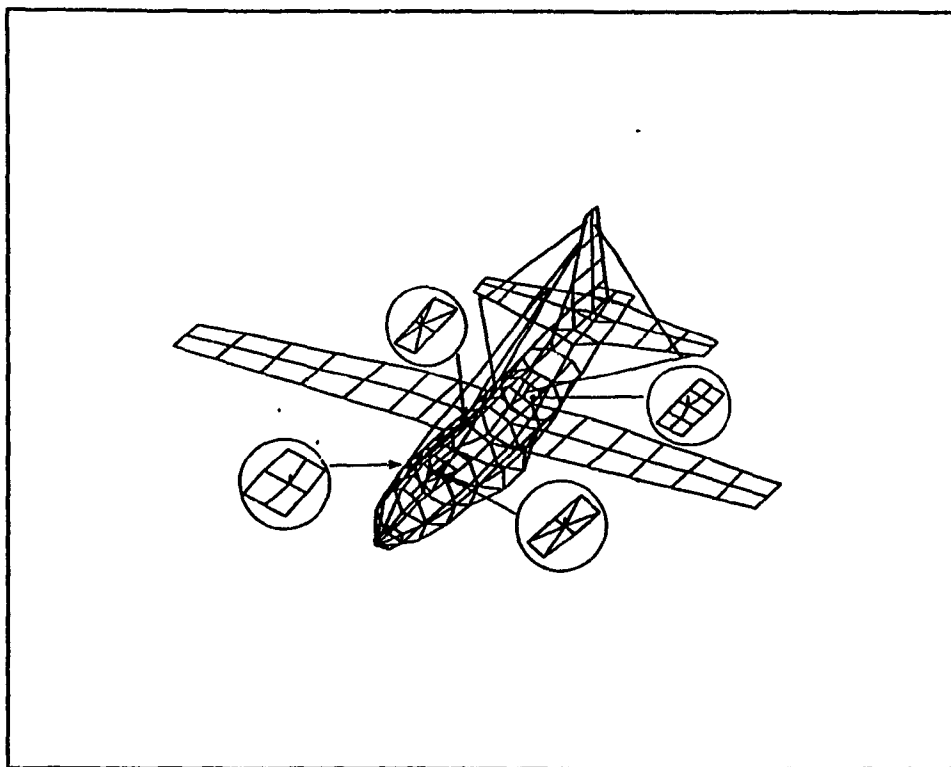


Figure 36 Wire Grid Model G

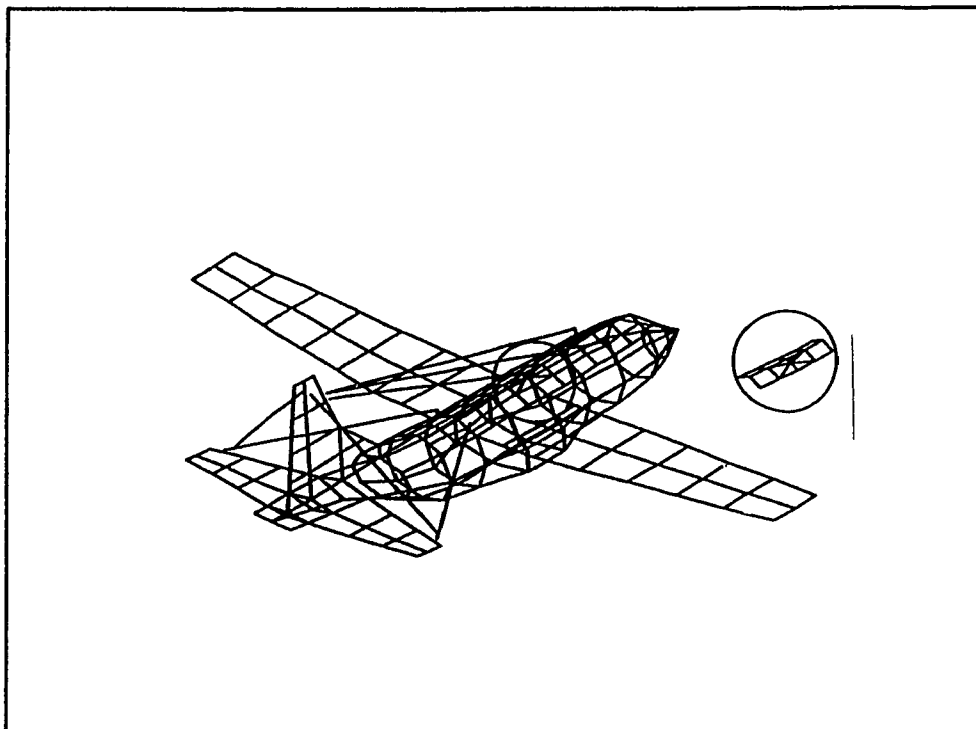


Figure 37 Wire Grid Model H

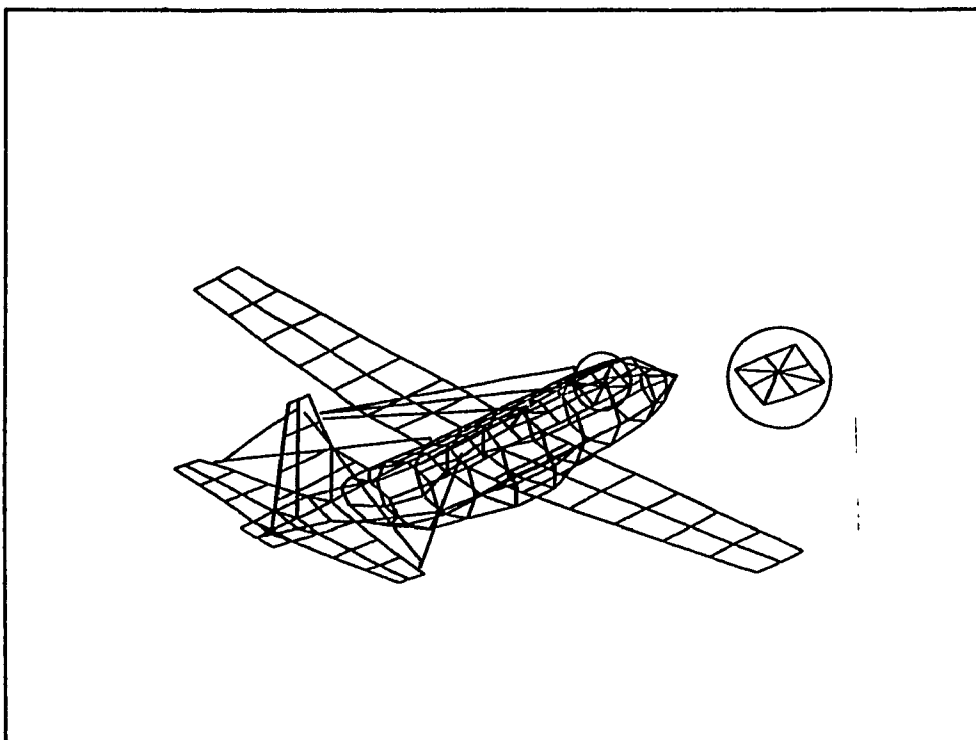


Figure 38 Wire Grid Model I

5.3.1.1. EC-130 Wire Grid Model G

Overall, the radiated fields of EC-130 model G correspond quite closely to those of base model F, particularly, the HF3 and HF4 patterns (figures 25, 26, 27 and 39). However, the agreement between the computed and scale model patterns of antenna HF1 degrade at the higher conical cuts. The desired, heart-shaped E-theta patterns that were intricately reproduced by the base model, are replaced by oval patterns of model G.

The similarity between the HF3 antenna patterns of model F and revision G stems from the similarity in current distribution on the two models. In both cases, the excitation of the near-central antenna results in current coupling evenly into antennas HF1 and HF2 as well as along the wheel wells and wing edges (figures 23 and 40).

Similarly, the excitation antenna HF4 results in the highest current along the horizontal wire of the dogleg antenna for both models F and G (figures 24 and 40). Consequently, the radiation patterns of the two models are predictably alike.

The current distribution on model G when exciting antenna HF1 offers insight into reasons for the degradation between the computed and scale model radiation patterns. Most notably, the largest current flows in the feed region of antenna HF3.

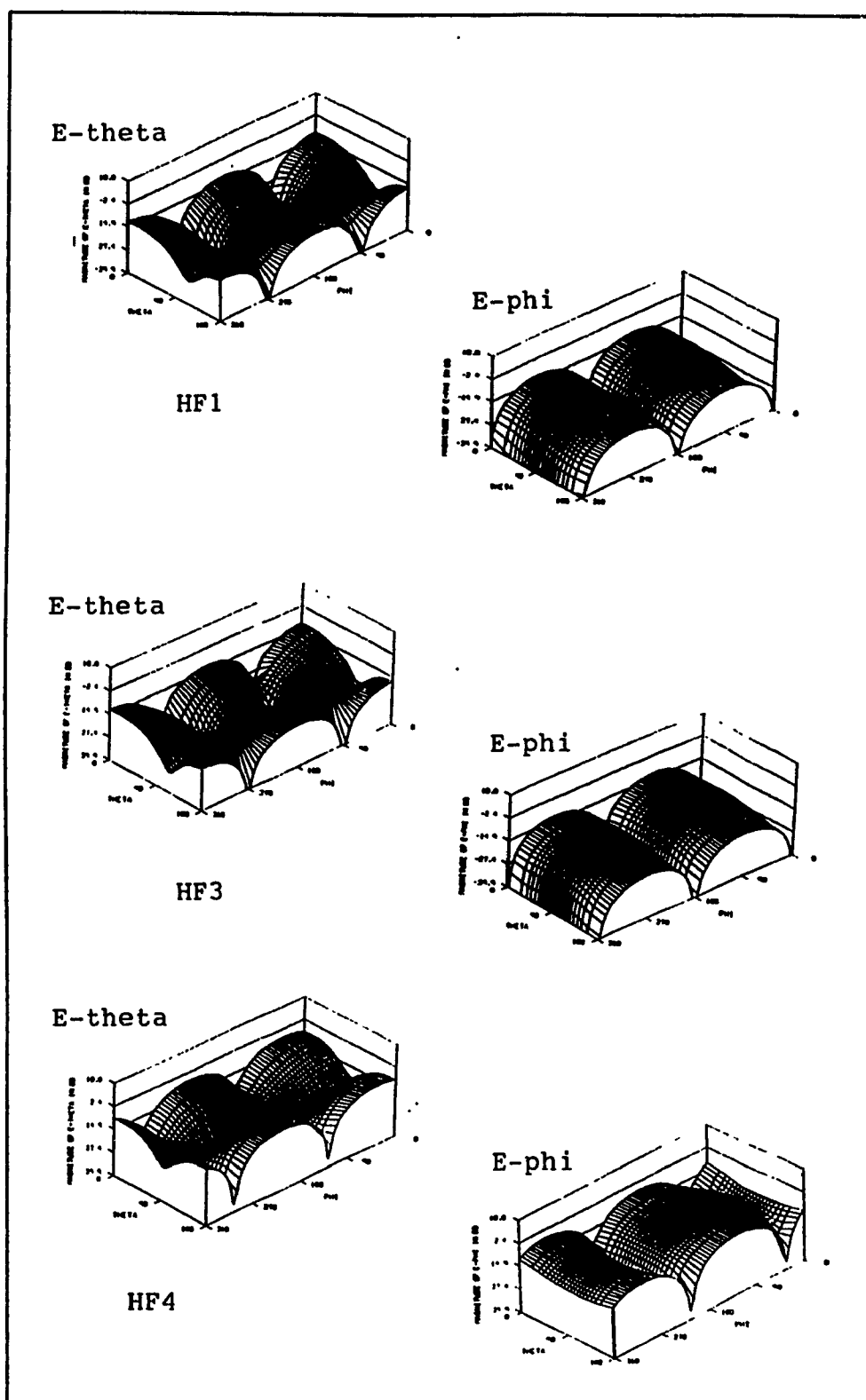


Figure 39 Model G - Radiation Patterns for HF1, HF3 & HF4 at 4.04 MHz (Computed)

Figure 40 Model G - Current Distribution for Excitation HF1, HF3 & HF4

This phenomena does not occur for the base model and is, therefore, attributed to the addition of wires on the starboard side of the airframe in the HF3 feed point region.

The spatial placement of segments is an important consideration in the modelling process. Intuitively, the wires should closely follow the geometrical topology of the conducting paths of the aircraft. Thus, reflecting the HF3 feed region wires onto the port side would maintain the symmetry of the full-scale aircraft structure. The resulting model H is illustrated in figure 37.

5.3.1.2. EC-130 Wire Grid Models H and I

The current distribution for EC-130 model H is significantly high in the feed region of antenna HF3 for each successive AUT (figure 41). This coupling behaviour has also occurred when testing model G and is illustrated in figure 40. Consequently, the radiated fields of EC-130 revisions G and H exhibit similar pattern characteristics (figure 42).

Model I was created by adding four crosswires in the HF2 feed region to maintain the integrity of the airframe symmetry. Since there is negligible current coupling into the starboard side of the aircraft when exciting port antenna HF1 and HF4, and only limited

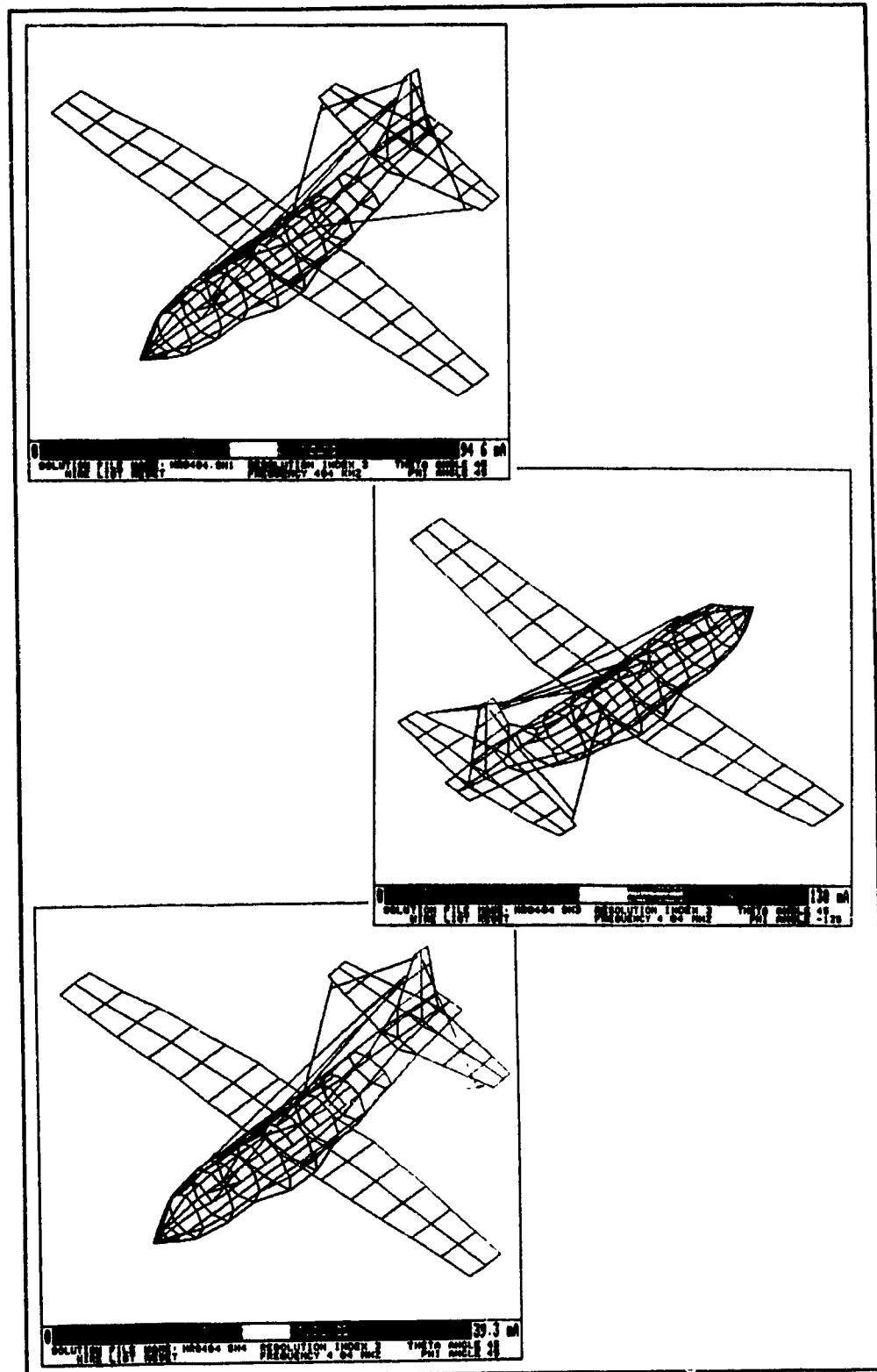


Figure 41 Model H - Current Distribution for Excitation HF1, HF3 & HF4 at 4.04 MHz

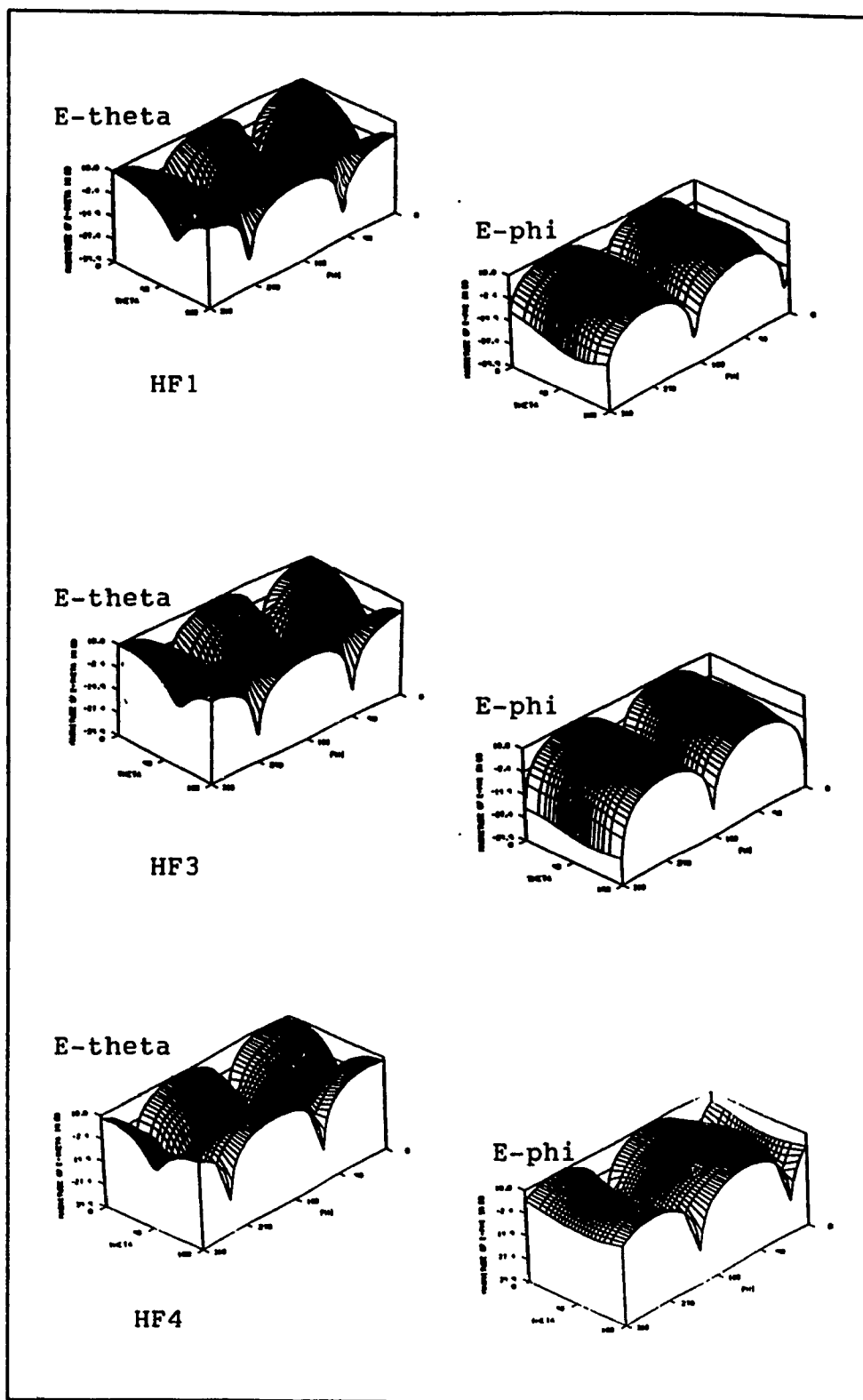


Figure 42 Model H - Radiation Patterns for HF1, HF3 & HF4 at 4.04 MHz (Computed)

coupling when exciting antenna HF3, the incremental perturbation in model topology did not adversely affect the electromagnetic response of EC-130 model I. The wire currents and radiation patterns approximate those of the preceding models (figures 43 and 44).

The results of the wire grid revisions G, H and I indicate that the numerical model of the EC-130 aircraft is especially sensitive to the wire distribution in the HF3 feed region.

5.3.1.3. EC-130 Triangulated Wire Grid Model P

In the book *Moment Method in Electromagnetic Techniques and Applications*, Moore and Pizer suggested that triangular segmentation be used for the mesh modelling of a continuous surface. In this way, currents will flow as they would in reality rather than 'forcing' the current paths.

The base model was triangulated by inserting diagonal wires in the rectangular grids. Model P consists of 591 segments and is illustrated in figure 45. At 4.04 MHz, model P complies absolutely to the NEC radii and segmentation requirements.

Once again, high current coupling occurs in the antenna HF3 feed region for each successive AUT (figure 46). The pattern agreement between the computed and scale model far fields has diverged (figures 25, 26, 27 and 47).

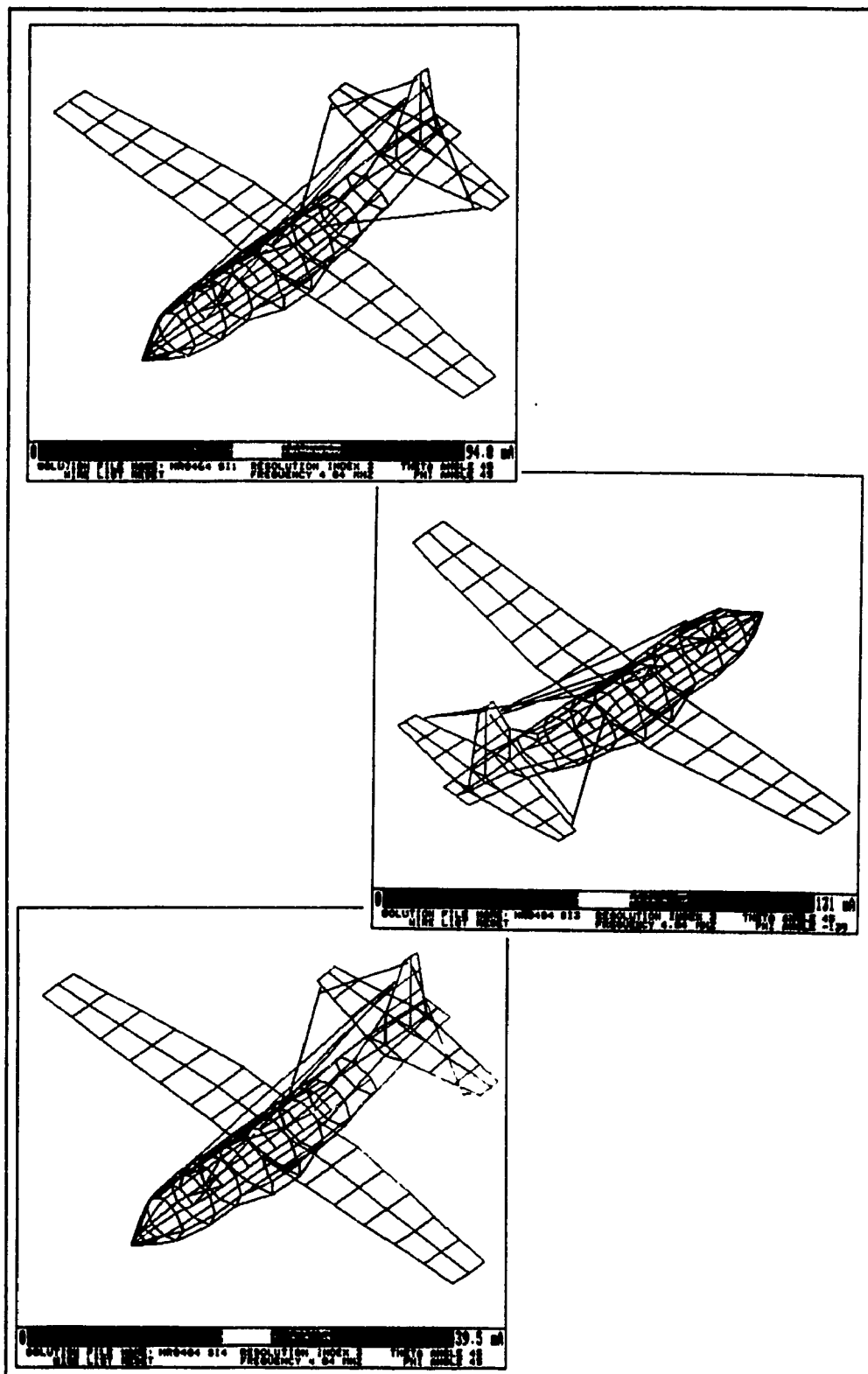


Figure 43 Model I - Current Distribution for Excitation HF1, HF3 & HF4 at 4.04 MHz

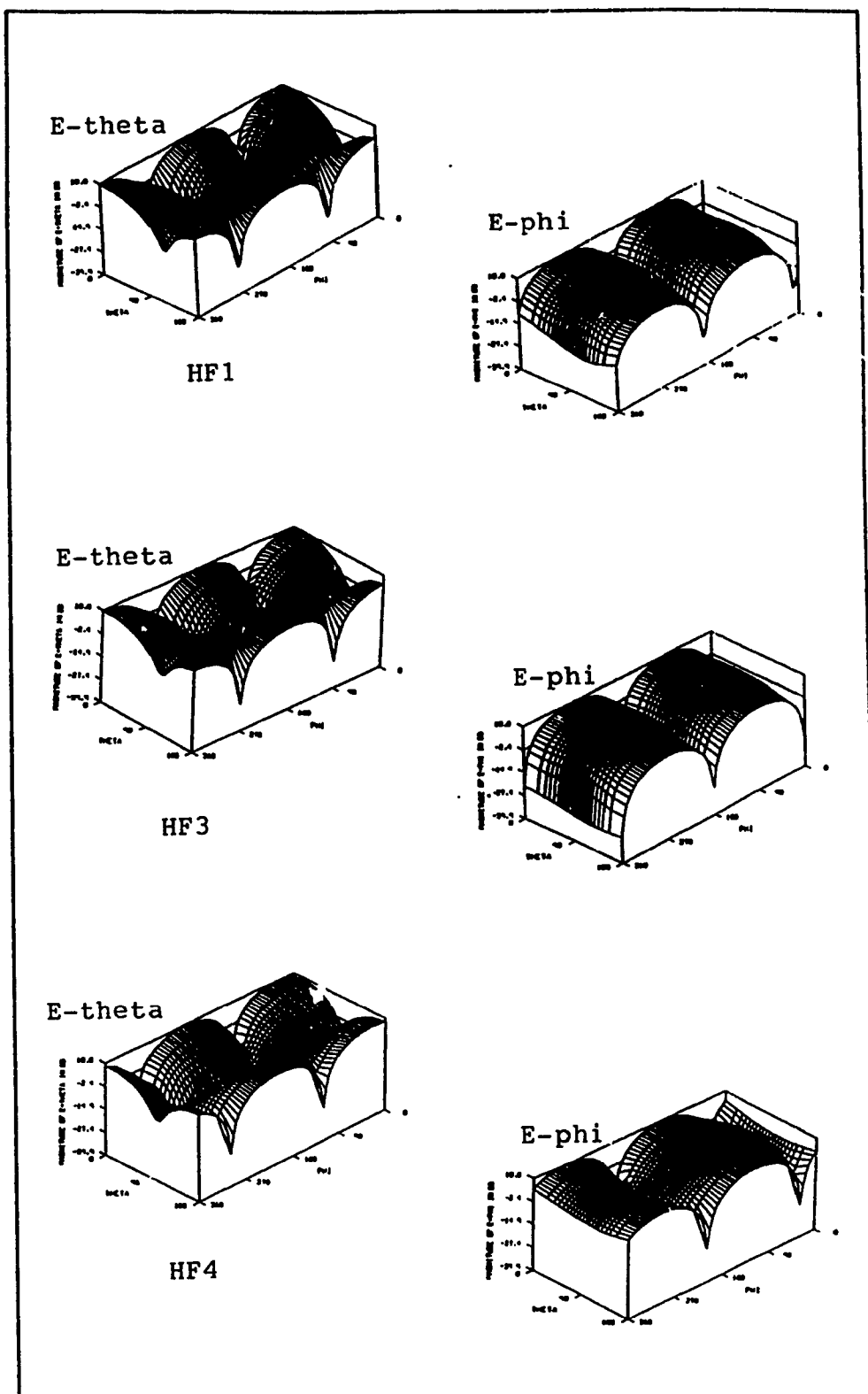


Figure 44 Model I - Radiation Patterns at 4.04 MHz for Excitation HF1, HF3 & HF4 (Computed)

Intuitively, the most effective approach to segmentation involves aligning the wires so as to maintain the integrity of the structure surface geometry. In order to model efficiently, a finer mesh should be incorporated in areas where larger currents might be expected for flow.

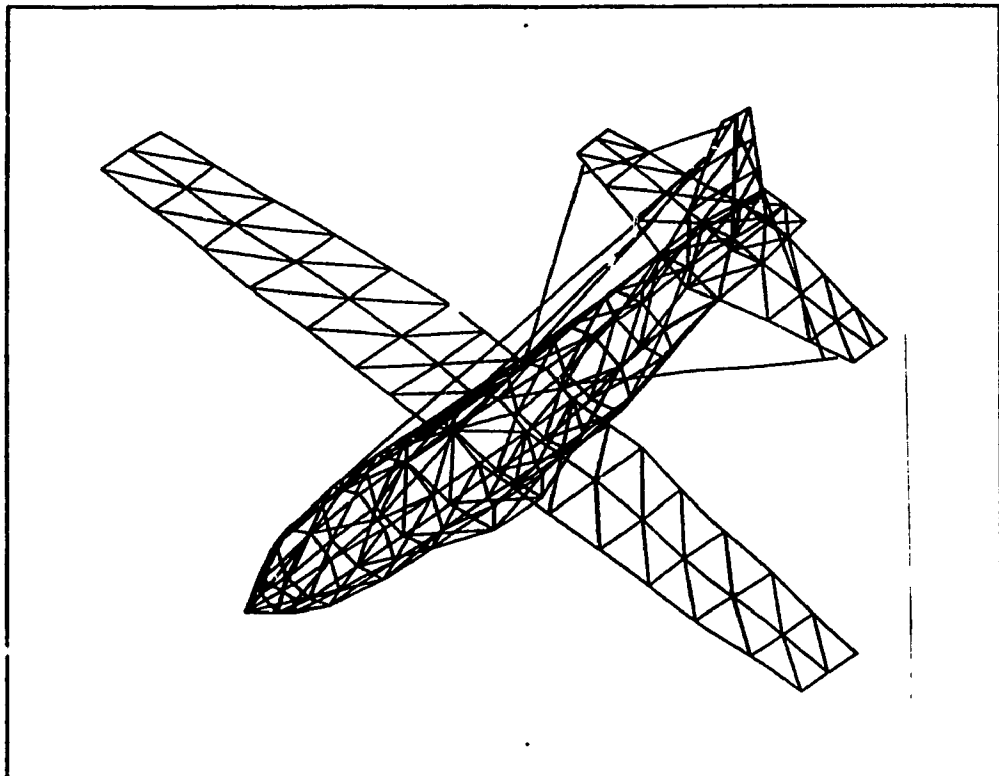


Figure 45 Triangulated Wire Grid Model P

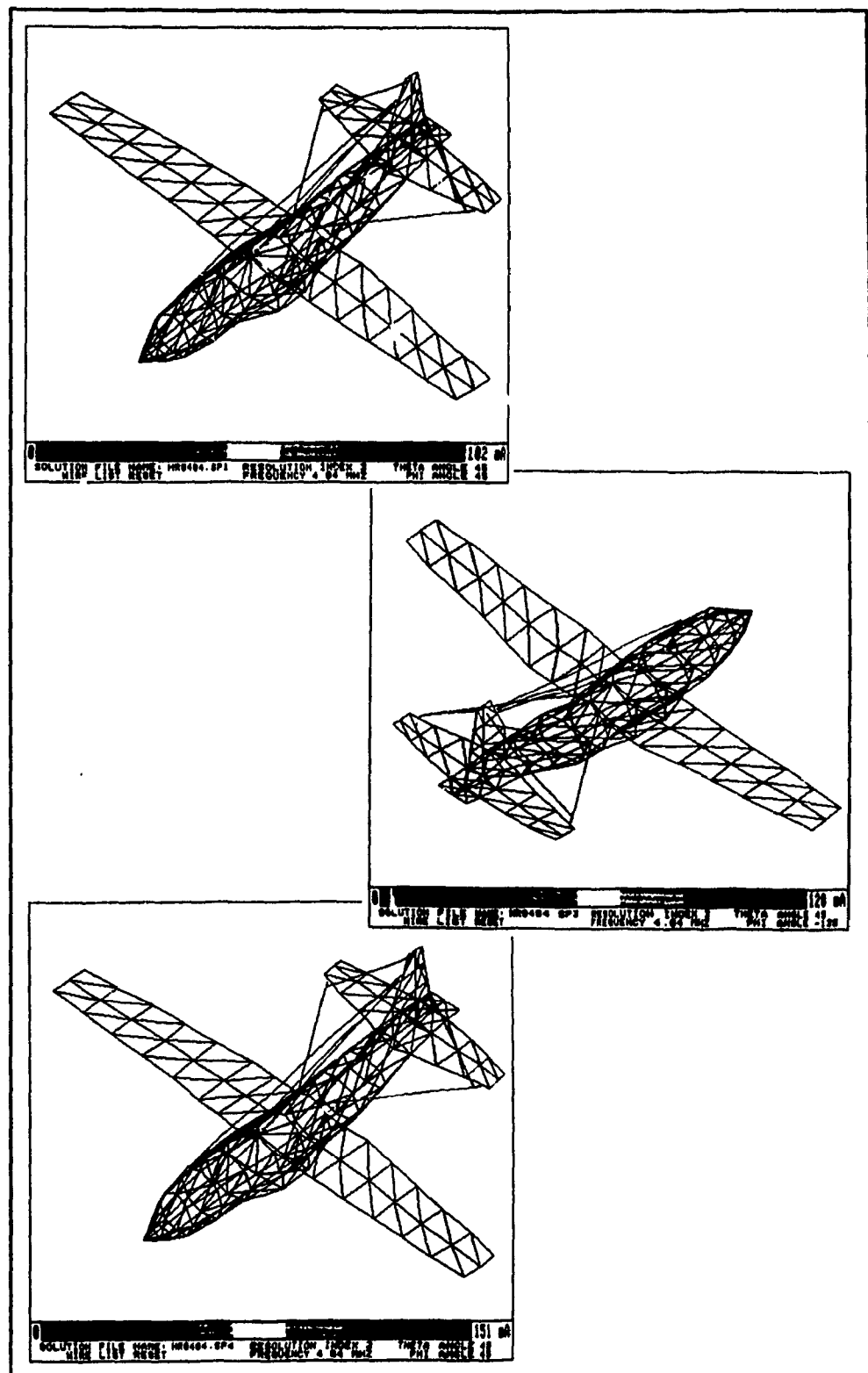


Figure 46 Model P - Current Distribution at 4.04 MHz for Excitation HF1, HF3 & HF4

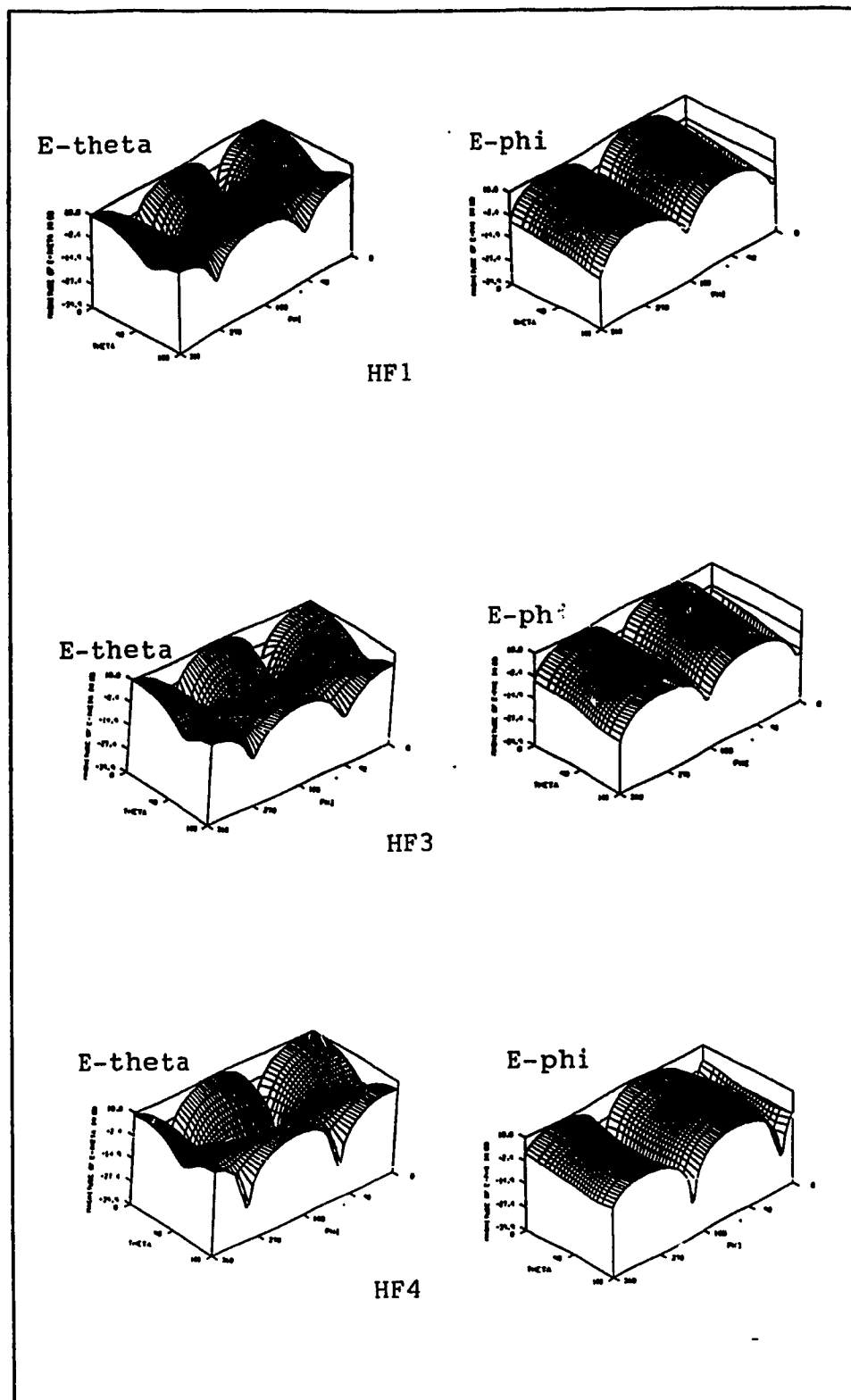


Figure 47 Model P - Radiation Pattern at 4.04 MHz for Excitation HF1, HF3 & HF4 (Computed)

5.3.2. Radius

As stated in chapter 3, the wire diameter is selected to 'correct' for the inductive differences between the wire grid model and the corresponding solid surface. The radii is such that the wire mesh has twice the external surface area of the surface being modelled. In addition, the wire radii must comply with the requirements of the Numerical Electromagnetics Code.

The segment diameter of model F through I inclusive were calculated manually using the same surface area rule of thumb. Soon after, programs RADIUS and CLEAN became available and automated the radii computation process. The program algorithm implements the 'twice the surface area' approach and, thus, the computed results closely approximate the manually derived diameter values. However, there is finer tapering in the computed radii of adjacent segments due to the iterative potential of high speed computers. Gradual changes in radius between connected segments are desirable since abrupt differences in diameter may decrease accuracy.

5.3.2.1. EC-130 Wire Grid Model J

EC-130 model J is identical to model I in terms of wire grid topology. The sole difference is that the radii of revision J is computed by programs RADIUS and CLEAN. The optimization in radii selection is illustrated in figure 48.

Antennas HF1, HF3 and HF4 of EC-130 model J were tested at an operating frequency of 4.04 MHz. The electromagnetic response of wire grid J differs from its topological equivalent - model I - and is more closely identified with base model F.

Figure 49 illustrates the current distribution on EC-130 J when exciting HF1. The largest current flows along the source antenna and there is coupling into the near-central and starboard antennas. When HF3 is the AUT, the highest current is along the receive antenna and a significant amount of energy is transferred into the port and starboard antennas. A plot of current distribution for source antenna HF4 shows the greatest current along its horizontal wire. In all cases, the current coupling into the airframe is most prominent at the extremities of the aircraft structure such as the nose, wheel wells, wing edges and tips of the vertical stabilizer and horizontal stabilator.

The radiation patterns, shown in figure 50, are

very similar to those of the base model F thus, confirming frequency stability of the model (figures 25, 26 and 27).

Intuitively, the finer tapering in wire radii is more desirable since, in reality, current varies gradually rather than abruptly.

5.3.2.2. EC-130 Wire Grid Model K

The wire grid topology of EC-130 model K is identical to that of model J. For the two-sided surfaces (wings, stabilizers), the surface area was equated to the total area of both sides for wires running in perpendicular directions in the mesh. In effect, the wire diameters on the wings, vertical and horizontal stabilizers were doubled (figure 51).

A frequency sweep of 2.13 to 30.00 MHz inclusive was executed on EC-130 model K. The number of seg/wav and wav/rad incompatibilities became increasingly significant as the operating frequency exceeded 8.00 MHz.

A chart tabulating the level of pattern agreement in terms of the number of lobes, shifting, E-theta and E-phi magnitude levels, and relative magnitude comparisons is shown in table III. The rating varies from 0 (poor) to 5 (very good) points. The corroboration between the computed fields and scale model measurements is exceptionally good at 4.04,

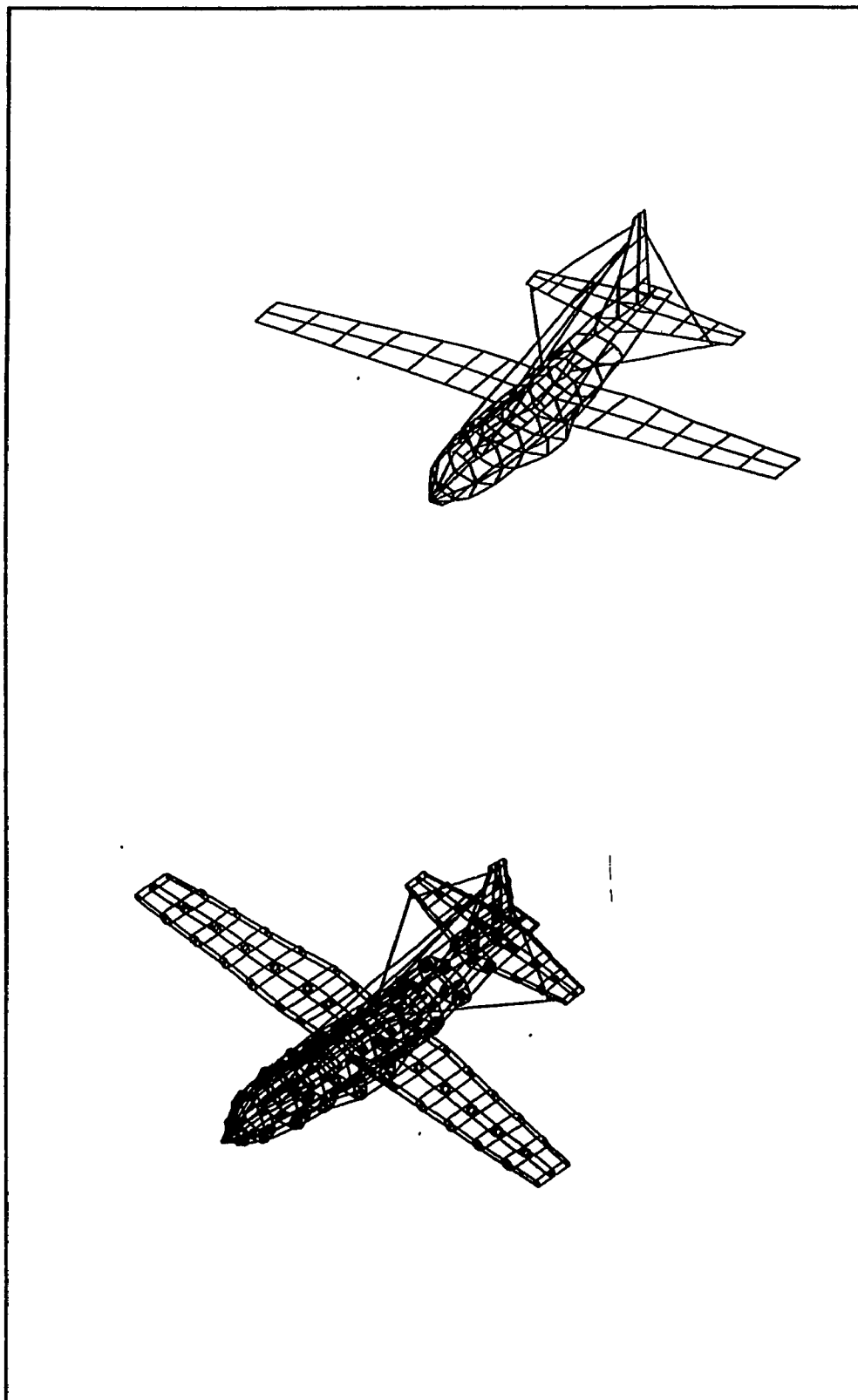


Figure 48 Wire Grid Model J

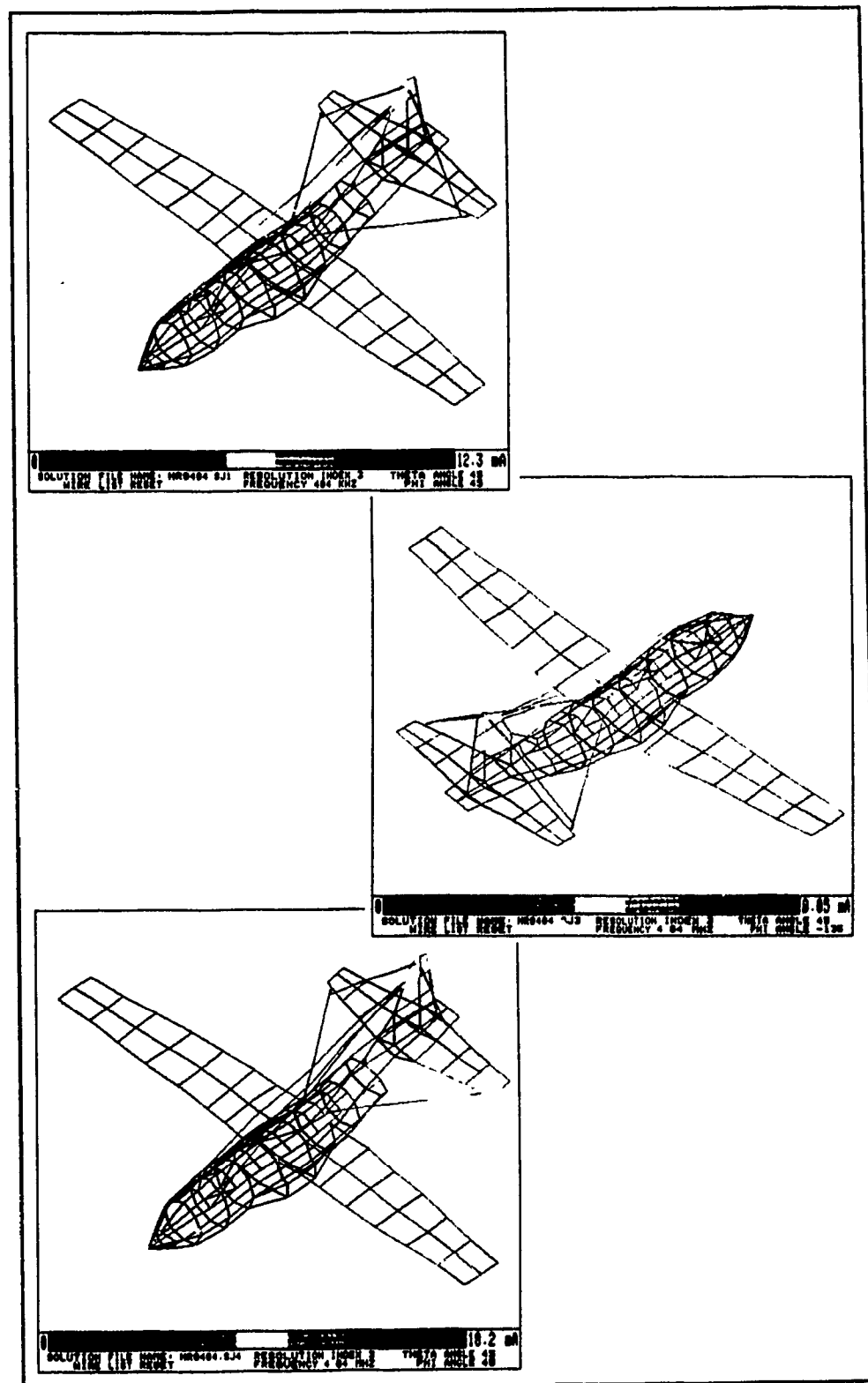


Figure 49 Model J - Current Distribution at 4.04 MHz for Excitation HF1, HF3 & HF4

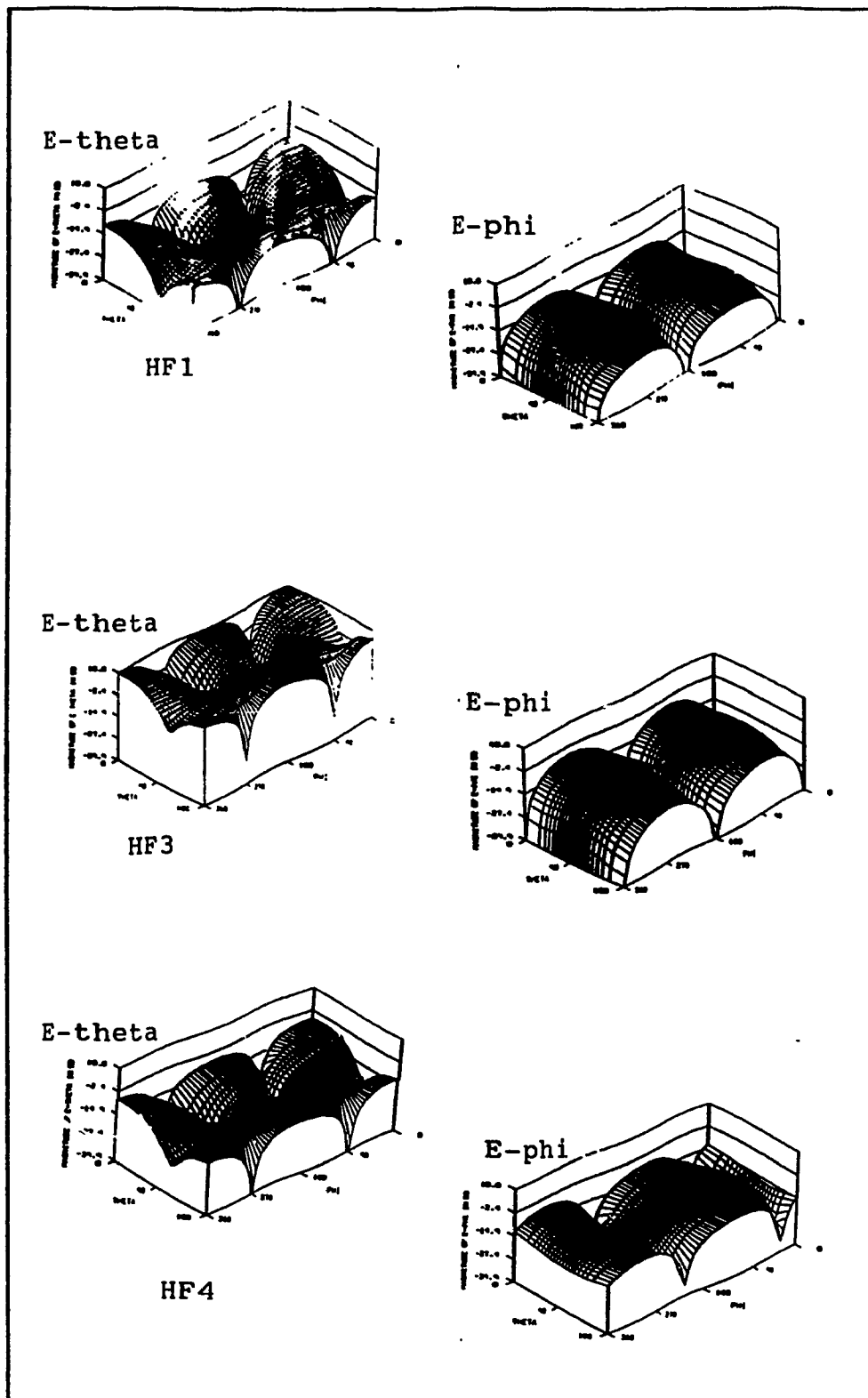


Figure 50 Model J - Radiation Pattern at 4.04 MHz for Excitation HF1, HF3 & HF4

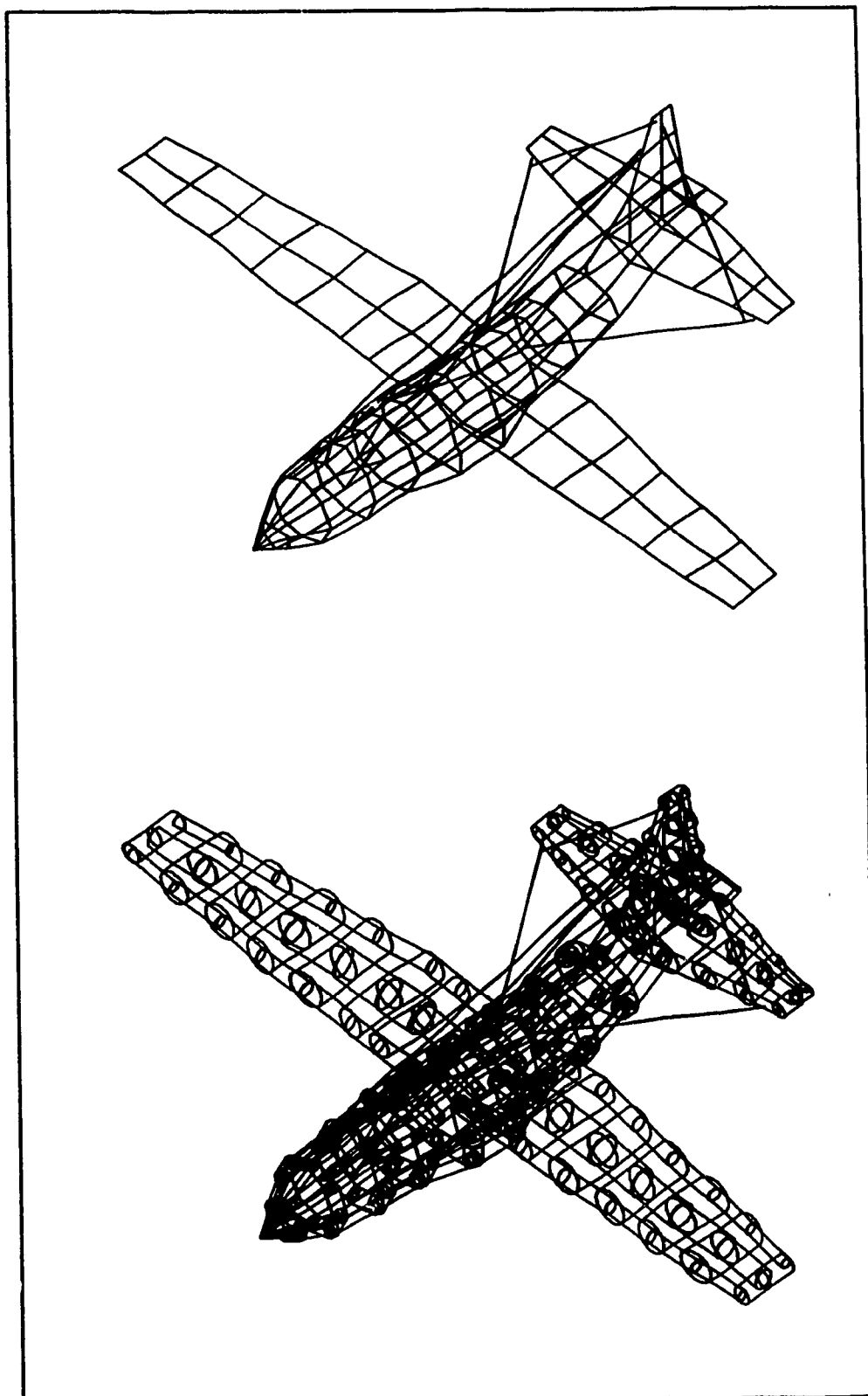


Figure 51 Wire Grid Model K

20.00 and 23.00 MHz for antennas HF1, HF3 and HF4.

The pattern agreement at lower and higher segments of the HF spectrum confirm the frequency stability of the model. In addition, the dimension/wavelength incompatibilities that appear at higher frequencies do not seem to adversely affect the accuracy of the results. A similar conclusion was drawn with base model F. The entire set of scale model and computed radiation patterns are displayed in Appendix B and C, respectively.

The performance parameters, η_p , $\%E_0$ and sub $\%E_0$ are plotted versus frequency for antennas HF1, HF3 and HF4. The graphs indicate that the computed values closely track the scale model parameters (figures 52 to 54).

| 2.13 MHz | Magnitudes | | Relative Magnitudes | No. of Lobes | | Alignment | | Total |
|----------|----------------|----------------|------------------------|----------------|----------------|----------------|----------------|-------|
| | | | | E _θ | E _φ | E _θ | E _φ | |
| | | | | | | | | |
| | E _θ | E _φ | | | | | | |
| HF1 | 3 | 4 | 4 | 4 | 5 | 4 | 5 | 31 |
| HF3 | 2 | 2 | 2 | 2 | 5 | 2 | 0 | 15 |
| HF4 | 3 | 4 | 3 | 3 | 5 | 3 | 3 | 24 |

| 4.04 MHz | Magnitudes | | Relative Magnitudes | No. of Lobes | | Alignment | | Total |
|----------|----------------|----------------|------------------------|----------------|----------------|----------------|----------------|-------|
| | E _θ | E _φ | | E _θ | E _φ | E _θ | E _φ | |
| | | | | | | | | |
| HF1 | 4 | 4 | 4 | 4 | 5 | 3 | 5 | 29 |
| HF3 | 3 | 5 | 3.5 | 3 | 5 | 3 | 5 | 27.5 |
| HF4 | 2.5 | 4 | 3.5 | 2.5 | 5 | 3 | 3.5 | 24 |

| 8.00 MHz | Magnitudes | | Relative Magnitudes | No. of Lobes | | Alignment | | Total |
|----------|----------------|----------------|------------------------|----------------|----------------|----------------|----------------|-------|
| | | | | E _θ | E _φ | E _θ | E _φ | |
| | E _θ | E _φ | | | | | | |
| HF1 | 2 | 2.5 | 2.5 | 2.5 | 3 | 4 | 19 | |
| HF3 | 2.5 | 3 | 3 | 3 | 4 | 4 | 22.5 | |
| HF4 | 2.5 | 4 | 3 | 2 | 4.5 | 3 | 4 | 23 |

Table III: Level of Pattern Agreement (Model K/Scale Model)

| 11.00 MHz | Magnitudes | | Relative Magnitudes | No. of Lobes | | Alignment | | Total |
|-----------|--------------|------------|------------------------|--------------|------------|--------------|------------|-------|
| | E_{θ} | E_{ϕ} | | E_{θ} | E_{ϕ} | E_{θ} | E_{ϕ} | |
| | | | | | | | | |
| HF1 | 2 | 2.5 | 3.5 | 2.5 | 0 | 4 | 3 | 17.5 |
| HF3 | 3 | 2 | 2.5 | 1.5 | 0 | 4 | 3.5 | 16.5 |
| HF4 | 2.5 | 3.5 | 3 | 3 | 3.5 | 3 | 4 | 22.5 |

| 14.00 MHz | Magnitudes | | Relative Magnitudes | No. of Lobes | | Alignment | | Total |
|-----------|--------------|------------|------------------------|--------------|------------|--------------|------------|-------|
| | E_{θ} | E_{ϕ} | | E_{θ} | E_{ϕ} | E_{θ} | E_{ϕ} | |
| | | | | | | | | |
| HF1 | 3.5 | 4 | 4 | 5 | 3 | 5 | 5 | 29.5 |
| HF3 | 4 | 3 | 4 | 4.5 | 2.5 | 5 | 4 | 27 |
| HF4 | 3 | 4 | 3.5 | 3.5 | 3 | 3.5 | 4 | 24.5 |

| 17.00 MHz | Magnitudes | | Relative Magnitudes | No. of Lobes | | Alignment | | Total |
|-----------|--------------|------------|------------------------|--------------|------------|--------------|------------|-------|
| | E_{θ} | E_{ϕ} | | E_{θ} | E_{ϕ} | E_{θ} | E_{ϕ} | |
| | | | | | | | | |
| HF1 | 3 | 3 | 3 | 2.5 | 2 | 4 | 3 | 20.5 |
| HF3 | 2.5 | 3 | 2.5 | 2 | 2.5 | 4 | 4 | 18.5 |
| HF4 | 2 | 4 | 3 | 2 | 4.0 | 4 | 4 | 23 |

| 20.00 MHz | Magnitudes | | Relative Magnitudes | No. of Lobes | | Alignment | | Total |
|-----------|------------|----------|------------------------|--------------|----------|------------|----------|-------|
| | E_θ | E_ϕ | | E_θ | E_ϕ | E_θ | E_ϕ | |
| | | | | | | | | |
| HF1 | 4 | 4 | 4 | 3.5 | 4 | 4 | 4 | 27.5 |
| HF3 | 3 | 3 | 3 | 3.5 | 3 | 4.5 | 3 | 23 |
| HF4 | 4 | 4 | 4 | 3.5 | 4 | 4 | 4 | 27.5 |

| 23.00 MHz | Magnitudes | | Relative Magnitudes | No. of Lobes | | Alignment | | Total |
|-----------|------------|----------|------------------------|--------------|----------|------------|----------|-------|
| | E_θ | E_ϕ | | E_θ | E_ϕ | E_θ | E_ϕ | |
| | | | | | | | | |
| HF1 | 4 | 4 | 4 | 3 | 4.5 | 4 | 4 | 27.5 |
| HF3 | 3.5 | 4.5 | 4 | 3.5 | 4.5 | 4 | 5 | 29 |
| HF4 | 3 | 3.5 | 3 | 2.5 | 3 | 4 | 4 | 23 |

| 26.00 MHz | Magnitudes | | Relative Magnitudes | No. of Lobes | | Alignment | | Total |
|-----------|------------|----------|------------------------|--------------|----------|------------|----------|-------|
| | E_θ | E_ϕ | | E_θ | E_ϕ | E_θ | E_ϕ | |
| | | | | | | | | |
| HF1 | 4 | 4 | 4 | 3.5 | 3.5 | 4 | 4 | 27 |
| HF3 | 2 | 2.5 | 2 | 2 | 2 | 4 | 4 | 18.5 |
| HF4 | 3 | 2 | 2.5 | 3 | 3 | 3 | 4 | 20.5 |

| * 30.00 MHz | Magnitudes | | Relative Magnitudes | No. of Lobes | | Alignment | | Total |
|-------------|--------------|------------|------------------------|--------------|------------|--------------|------------|-------|
| | E_{θ} | E_{ϕ} | | E_{θ} | E_{ϕ} | E_{θ} | E_{ϕ} | |
| | | | | | | | | |
| HF1 | 3 | 3 | 3 | 3 | 3.5 | 4 | 4 | 23.5 |
| HF3 | 2.5 | 3 | 3 | 2 | 2.5 | 4 | 4 | 22 |

* Note: HF4 scale model field patterns were not measured at 30 MHz.

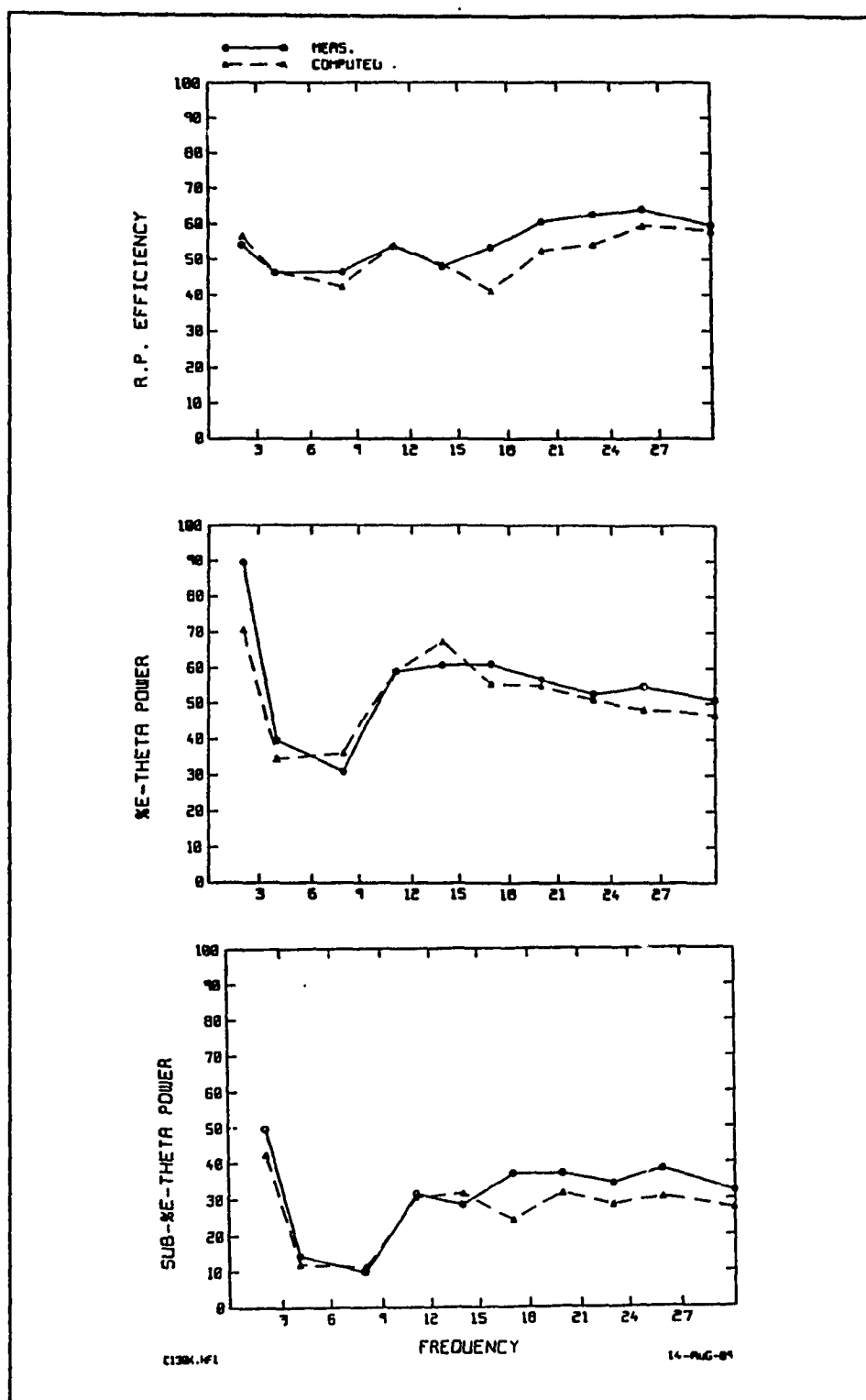


Figure 52 Model K - HF Assessment Parameters for HF1

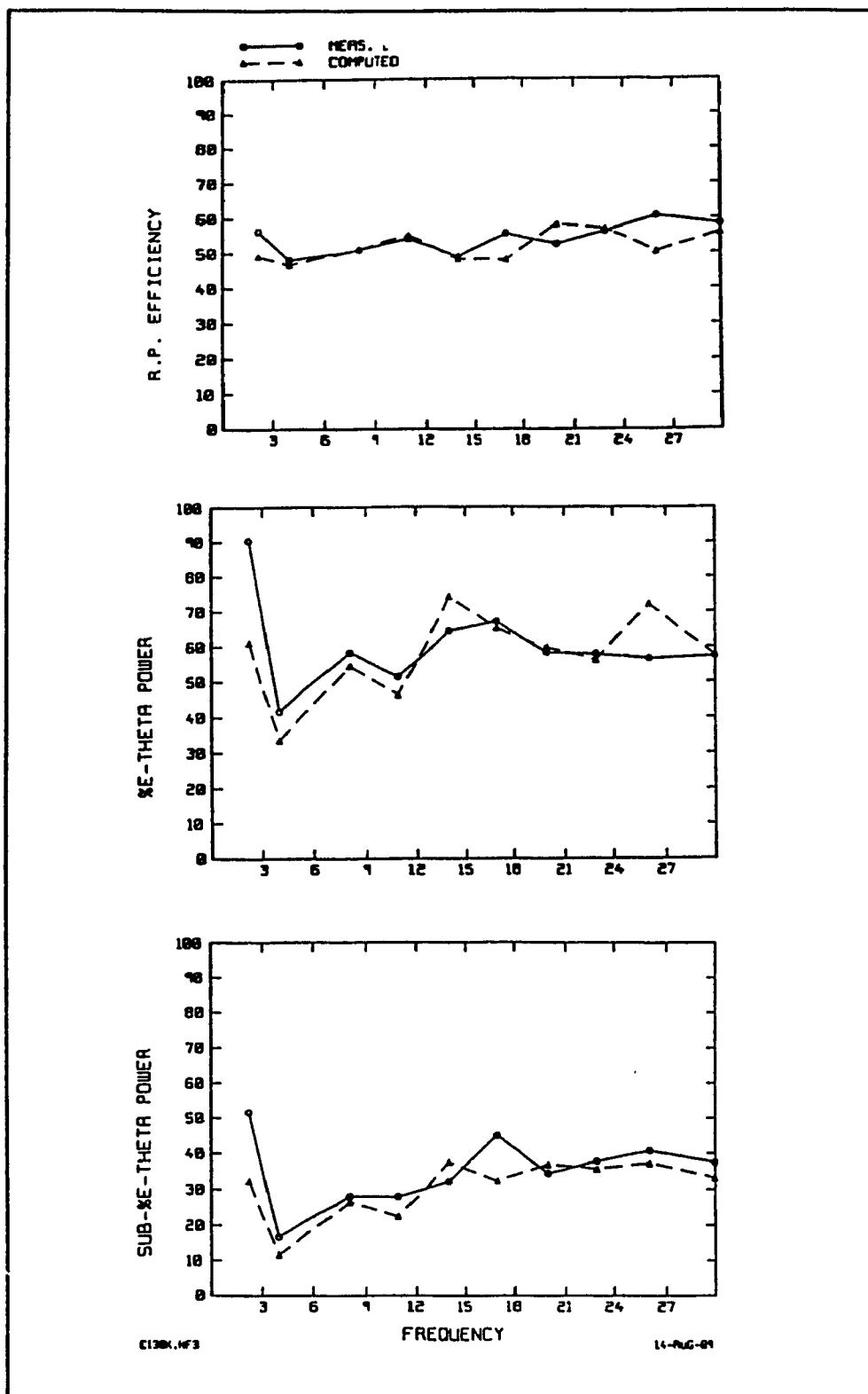


Figure 53 Model K - HF Assessment Parameters for HF3

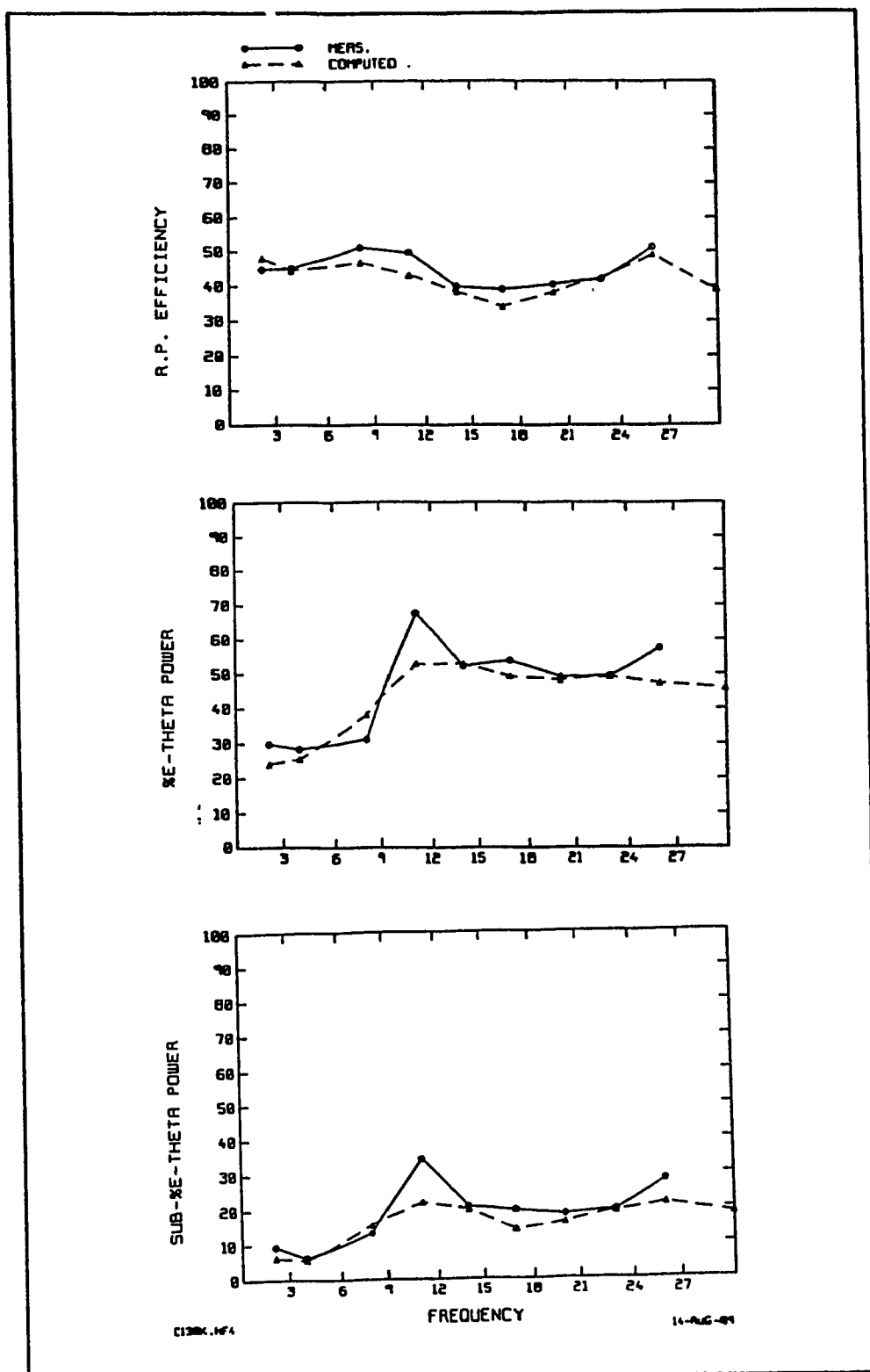


Figure 54 Model K - HF Assessment Parameters for HF4

Input Impedance and Resonance

The input impedance of an antenna is the impedance presented by the antenna at its terminals. Complex input impedance is composed of input resistance (real) and input reactance (imaginary) such that

$$Z_{in} = R_{in} + jX_{in}$$

The input resistance accounts for the radiated and dissipated power losses whereas the input reactance represents the power stored in the near field of the antenna (Stutzman and Thiele).

Plots of the input impedance versus frequency are shown in figure 55 for antennas HF1, HF3 and HF4. The input impedance can be understood by equating the wire antenna mounted atop the wire grid airframe to a transmission line terminated in an open circuit (figure 56).

Accordingly, resonances will occur when the antenna length is of the order $L = (2n-1)\lambda/4$. The losses that are incurred by input resistance is due to radiation and alludes to a low loss transmission line model. The inclusion of losses results in a slight shifting of the resonant condition ($X_{in} = 0$).

For a lossless open circuited transmission line, resonance occurs at intervals of $l = (2n-1)\lambda/4$. The

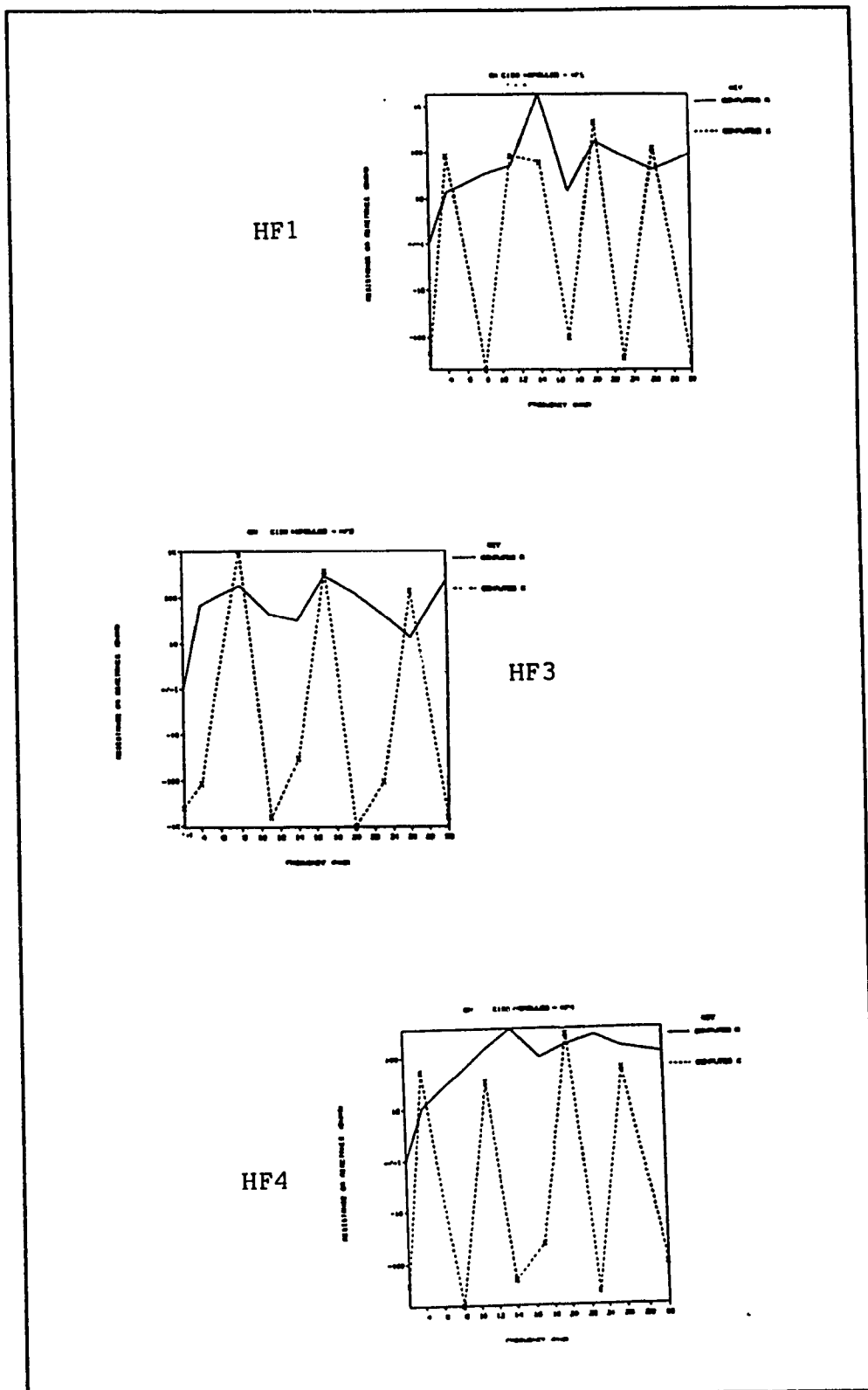


Figure 55 Model K - Input Impedance

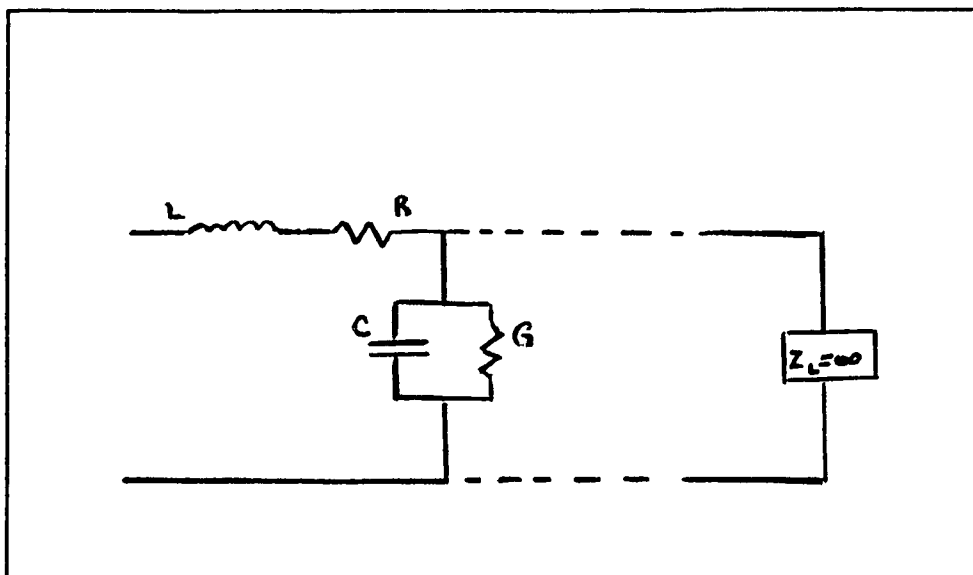


Figure 56 Open Circuit Transmission Line Model

length of port antenna HF1 is 20.384 meters and is expected to exhibit resonance at 3.7 MHz, 11.0 MHz, 18.4 MHz and 25.8 MHz. The graph of impedance versus frequency for antenna HF1 indicate that resonance occurs at frequencies corresponding to the intersections with the horizontal line passing through the point where $X_{in} = 0$. The frequencies of 3.1, 9.8, 18.3 and 24.8 MHz are lower than those predicted for the lossless transmission model and is due to the inclusion of losses in the circuit.

Similarly, antenna HF3 is 14.937 meters in length and is expected to exhibit resonance at 5.0, 15.1, and 25.1 MHz for the lossless transmission line analogy. The graph indicates resonances at 5.2, 15.0 and 24.9 MHz. The transmission line model closely approximates the actual resonant condition. The slight difference

is a result of the finite input resistance of the antenna.

The HF4 dogleg antenna is 20.718 meters in total length and resonances are predicted to occur at 3.0 MHz, 10.9 MHz, 18.1 MHz and 25.34 MHz. According to the computed plots of input impedance, the reactance vanishes at 3.6 MHz, 10.0 MHz, 18.0 MHz and 24.9 MHz. Once again, the predicted and computed resonant conditions occur at approximately the same frequency and the slight shifting is attributed to the input resistance of antenna HF4.

Thin Wire Kernel Analysis

In all the previous models, the extended thin wire kernel (EK) option of the Numerical Electromagnetic Code was invoked. The EK feature represents the current as a current tube rather than a line source along the segment axis. Soon after, it was discovered that the current tube simulation is applied only to those segments that are parallel to and of the same radius of the connecting segments. In all other instances, NEC reverts to the line source model.

The segments forming the HF antennas are the sole wires that satisfy the criteria for implementing the EK option. Model K 'minus EK' was executed. The

resulting current distributions for source antenna HF1, HF3 and HF4 were identical to the original model K. This may be due to the limited application of the current tube representation.

Computed/Full Scale

EC-130 model K was executed at 14 MHz above a perfect ground plane. In addition, the full scale test site was simulated by defining the electrical properties of seawater in the NEC input file. Despite efforts to model the aircraft and the test environment, the computed patterns do not converge to full scale measurements.

CHAPTER 6

CONCLUSION

In-flight radiation patterns of the EC-130 Tacamo HF antennas were measured at the Antenna Test Laboratory (ATLAS) in Chesapeake Bay. In addition, two copper-plated, fiberglass 1/100 scale models of the airframe-antenna system were constructed and tested under the following conditions:

1. transmitting mode, $f < 500$ MHz
2. receiving mode, $500 \text{ MHz} < f < 3000 \text{ MHz}$.

Pattern comparisons revealed significant discrepancies between the full scale and scale model measurements. Consequently, a computer model of the EC-130 HF antenna installation was developed in order to qualify the in-flight and scale model results.

Generally, validating numerical models of complex geometry requires experimental measurements. However, reliable data is unavailable. Therefore, only incremental perturbations in model topology were effectuated.

The Numerical Electromagnetics Code uses the Electric Field Integral Equation with the Method of Moments to solve for the currents on the wire grid model. Once the current distribution is found, the far field is readily determined by traditional

radiation integrals.

An effective wire grid model will support a current distribution that approximates that on the corresponding structure surface. A wire mesh, in the shape of the solid surface, will electromagnetically approximate said surface, provided that the grid size is small compared to a wavelength. To this effect, it is the structure geometry and the electrical factor of dimension/ λ that determines the wire grid topology.

EC-130 base model F was developed in accordance with the aforementioned modelling principles. Antennas HF1, HF3 and HF4 were tested at frequencies 4.04, 8.00, 14.00 and 23.00 MHz. The agreement between the computed and scale model patterns is quite good for both polarizations throughout the HF band. The base model maintained good agreement at the higher frequencies confirming model stability.

High currents were evident in the feed element regions of the source antennas. Intuitively, a finer segmentation should be used where large currents are expected to flow. Wires were added progressively to the feed element areas of HF antennas 1 through 5 inclusive, resulting in models G, H and I. Overall, the radiation patterns at 4.04 MHz were similar to those of base model F. However, there were large currents in the near-central feed region of the

airframe when exciting antenna HF1, HF3 or HF4.

The smoother radius tapering of models J and K seemed to correct the unusually high current in the HF3 feed region. Antennas HF1, HF3 and HF4 on wire grid model K were tested at frequencies 2.13, 4.04, 8.00, 11.00, 14.00, 17.00, 20.00, 23.00, 26.00 and 30.00 MHz. The agreement with the scale model measurements were exceptionally good through most of the HF range. Furthermore, the computed performance parameters closely track the scale model values for antennas HF1, HF3 and HF4. In addition, the predicted resonant frequencies based on the open circuit transmission line analogy matched the resonant frequencies of the input impedance curves of wire grid model K.

Impedance loading , although not covered in the thesis, is an alternative or complementary approach to model refinement. This may include shunting the excitation source with a capacitance to modify the input impedance of the antenna or inserting a resistance in parallel with a capacitance at the aft end of an antenna to simulate the electrical termination.

The in-flight testing site was simulated with the addition a perfectly conducting ground plane as well as seawater. However, the computed patterns failed to

converge to full scale measurements. The numerical models continuously demonstrated superior agreement with the scale model measurements.

Development of the EC-130 wire grid model served to qualify prior full scale and scale model measurements. Further work in model refinement will optimize the agreement between the computed and scale model patterns. In particular, modifications in segmentation and radii selection for the sensitive HF3 feed region of the airframe should be explored.

The EMC Laboratory at Concordia University has recently acquired greater computing capability enabling the Numerical Electromagnetic Code to be executed in a more time efficient manner. As a result, wire grid models are tested more readily at finer increments of frequency. This would offer new insight into resonant behaviour and input impedance characteristics of the model.

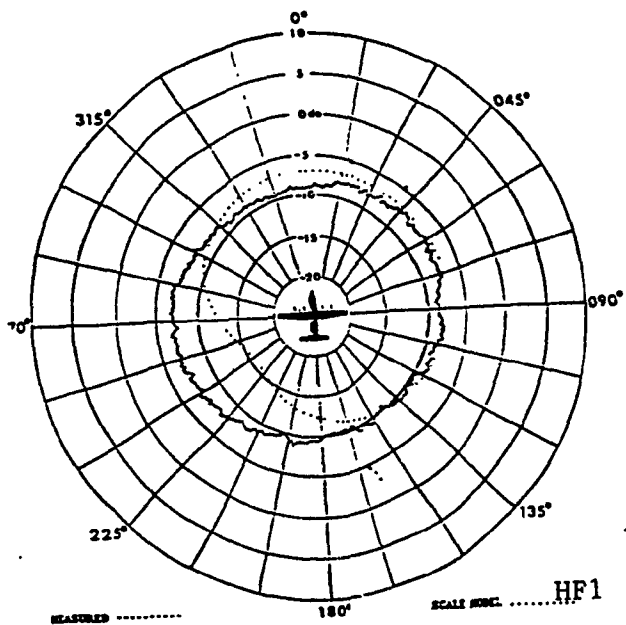
The impedance curves of the EC-130 wire grid representation corroborates with the predictions based on the open circuit transmission line analogy. It is recommended that scale model impedance values be made available to further validate the numerical model.

A surface patch modelling approach can also be used to validate the wire grid results. Program Junction (Hwu) solves for surface currents on

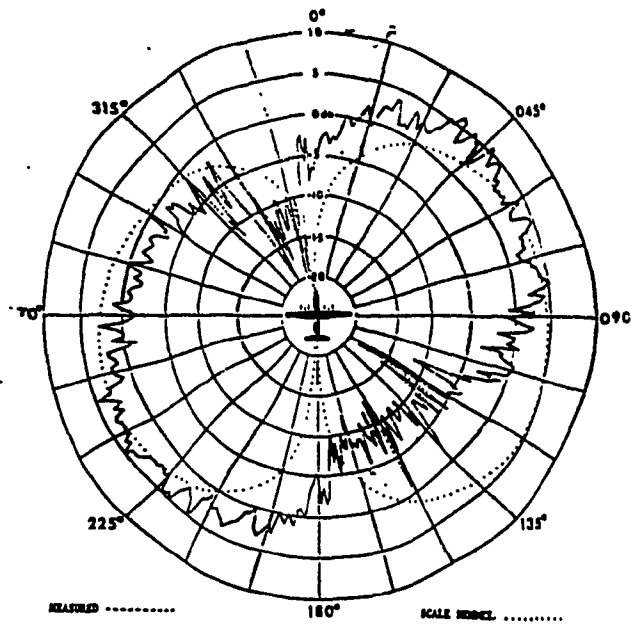
triangular patch models and is presently available at
Concordia University.

APPENDIX A

Appendix A contains the in-flight and scale model radiation patterns of antennas HF1 and HF4. The experimental data was provided by the Naval Air Test Center.

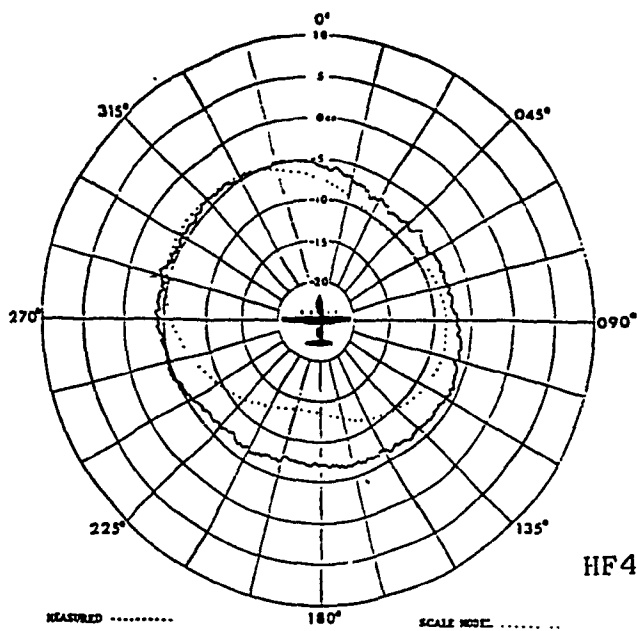


E-theta

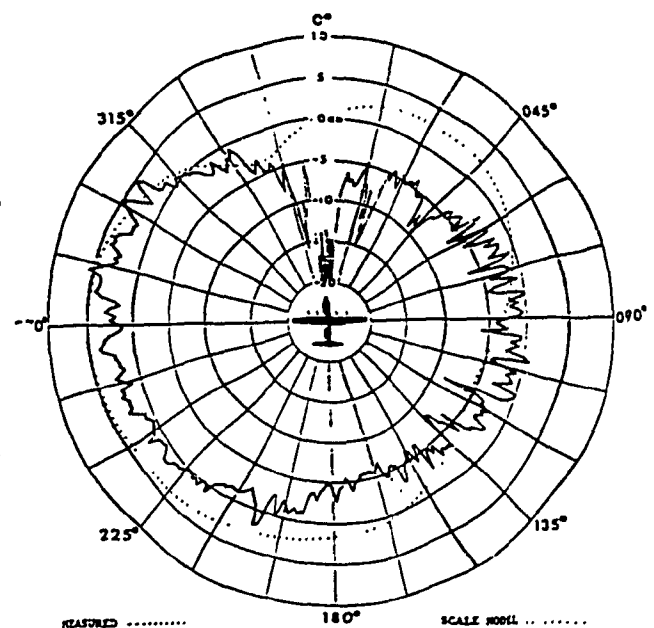


E-phi

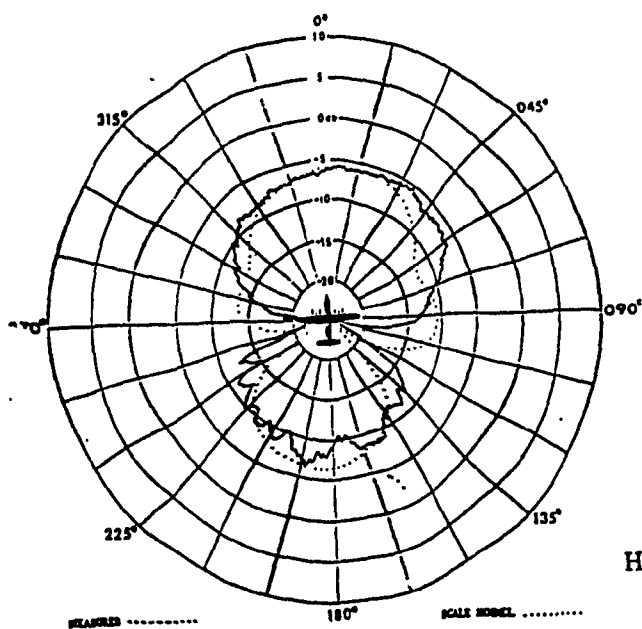
Frequency - 4.00 MHz



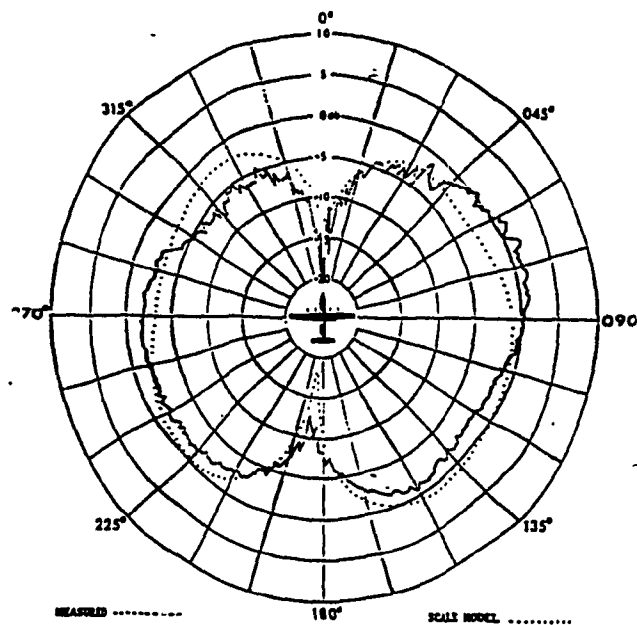
E-theta



E-phi

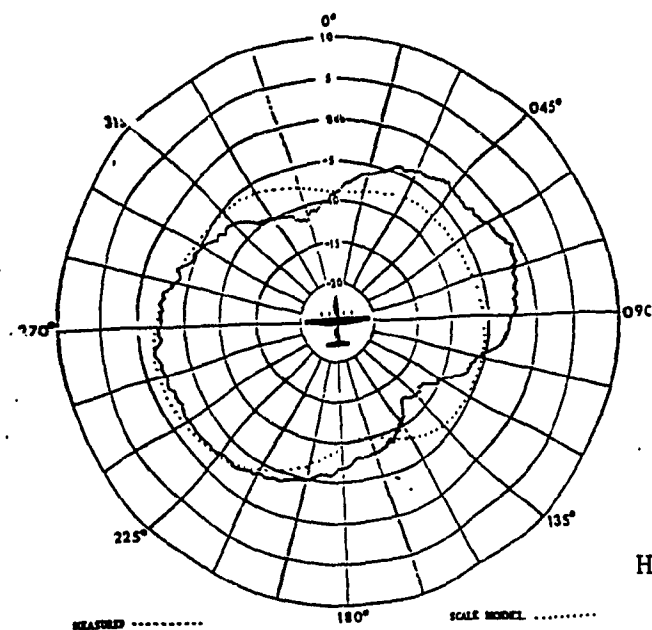


E-theta

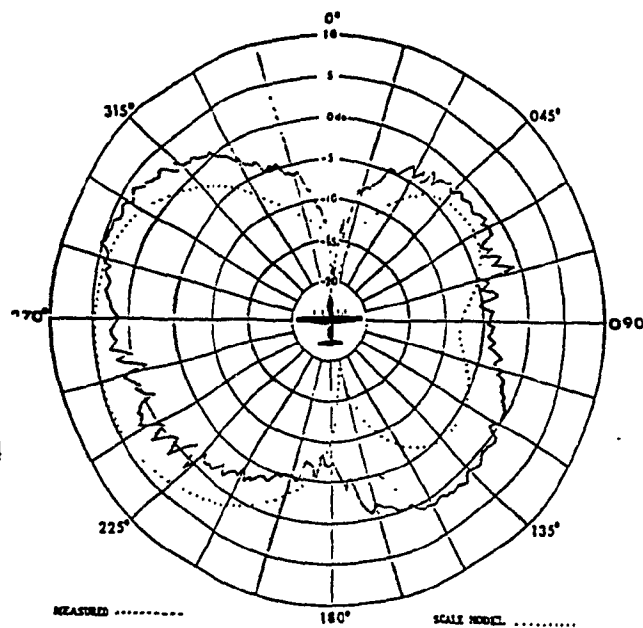


E-phi

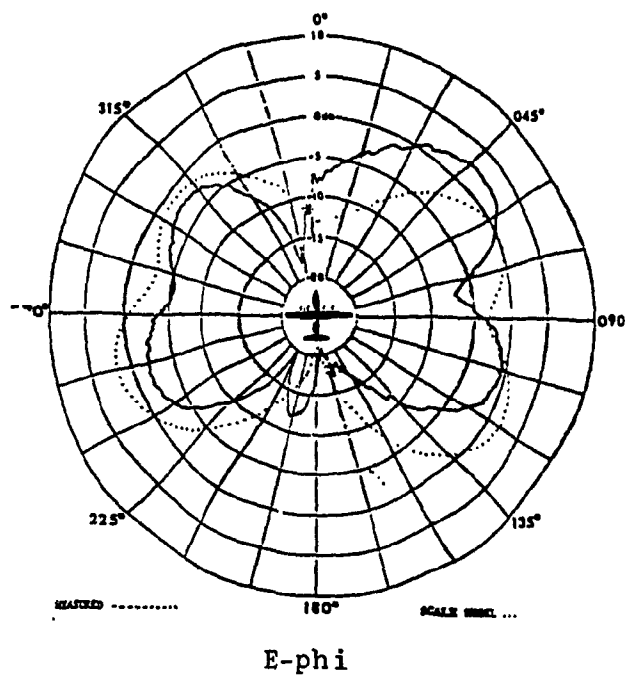
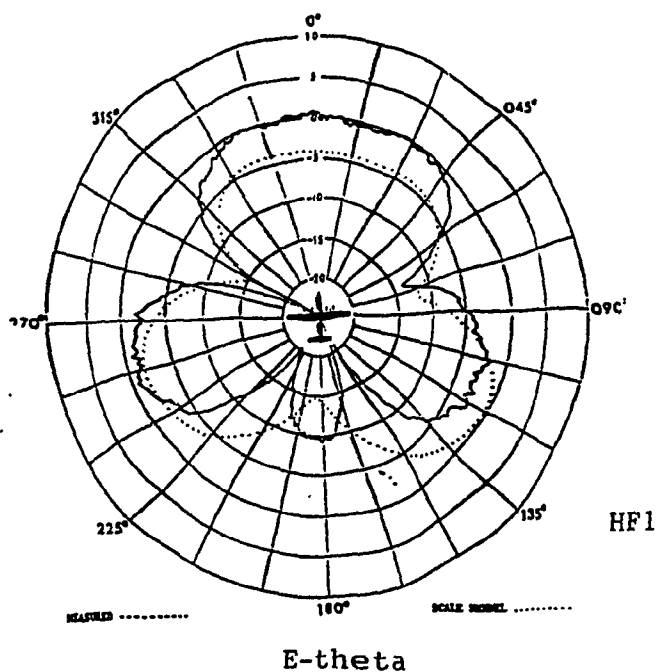
Frequency - 8.00Mhz



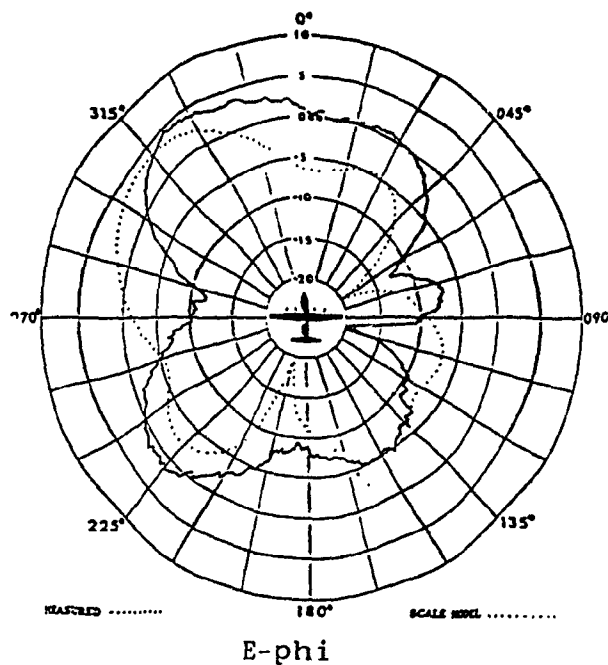
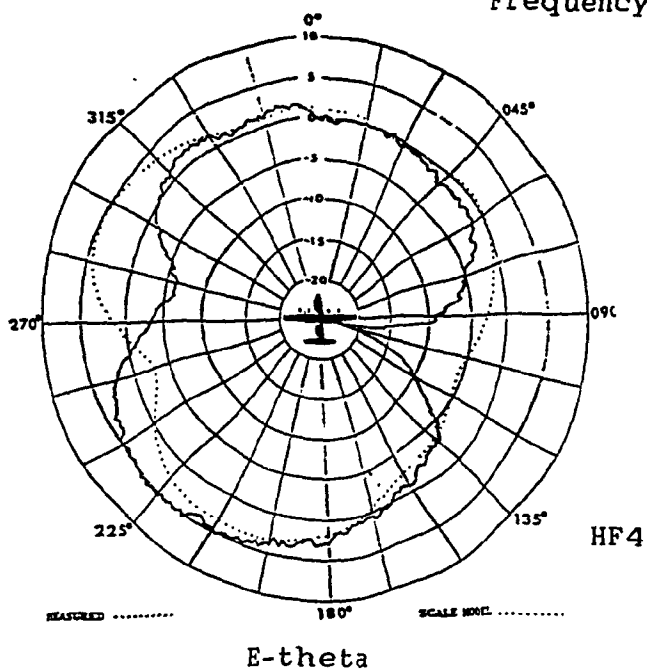
E-theta

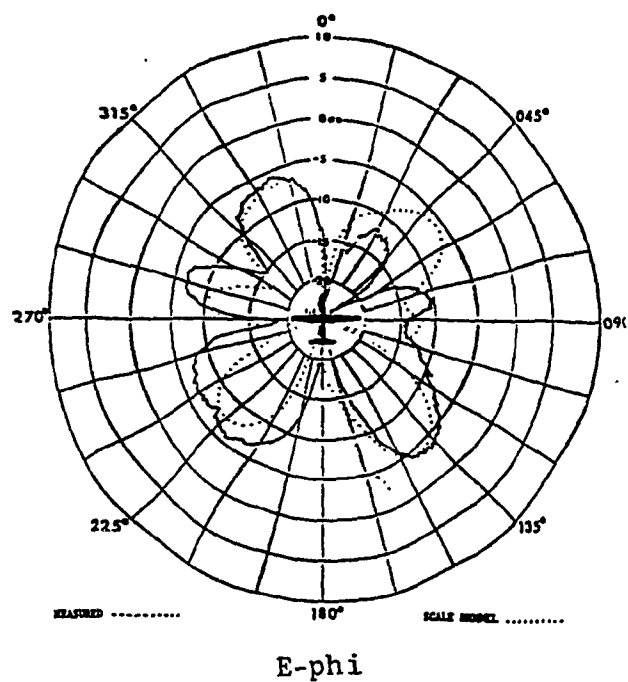
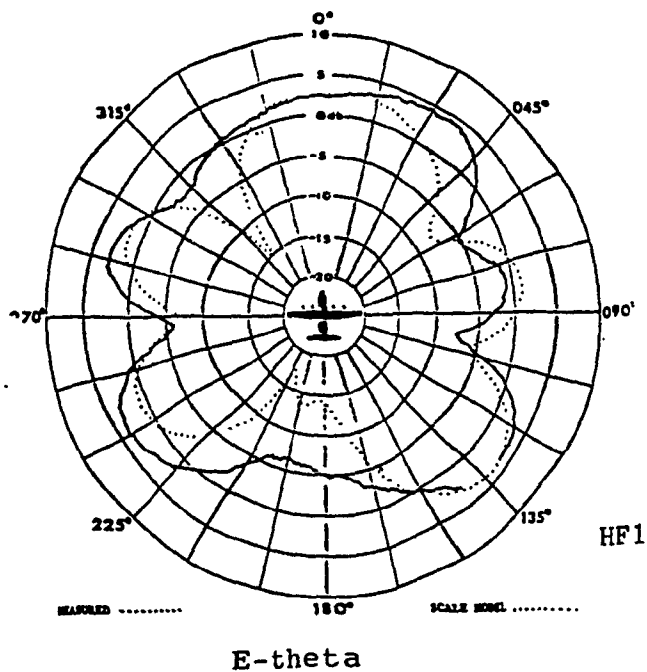


E-phi

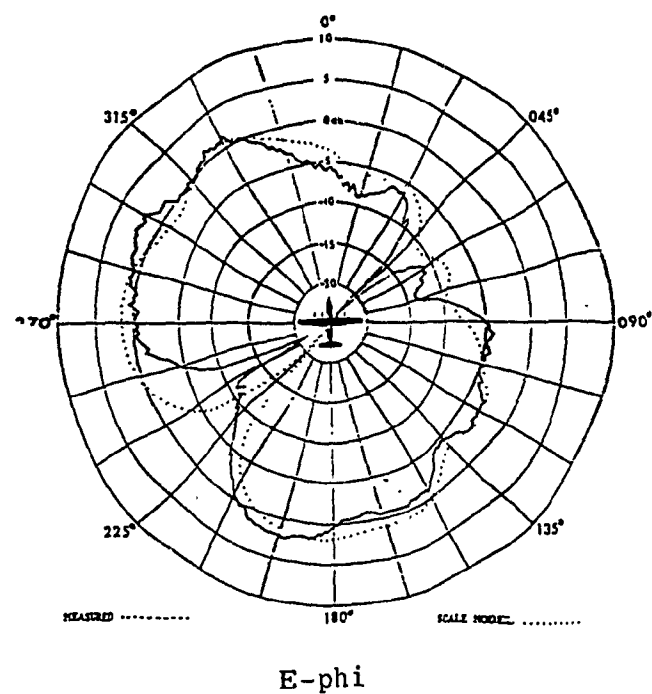
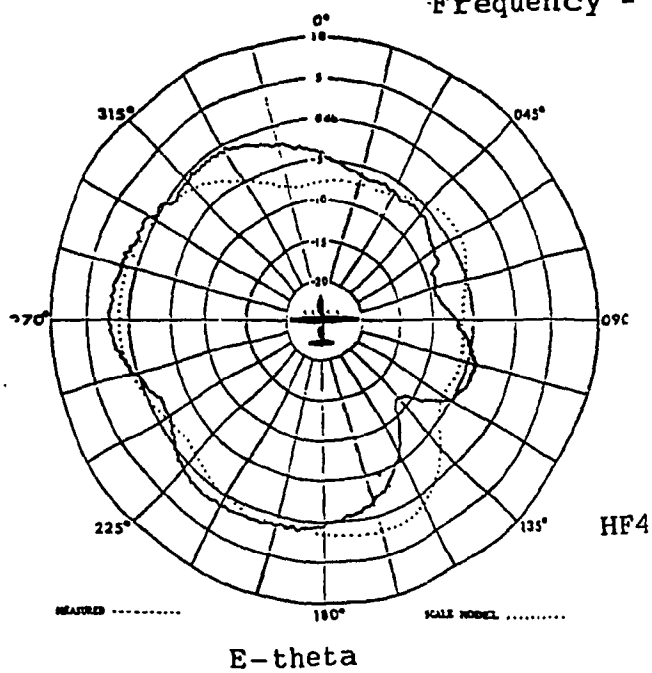


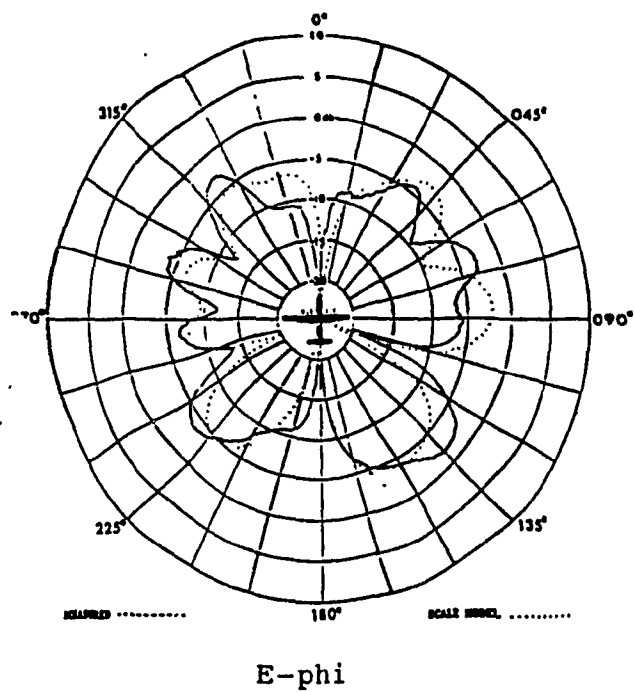
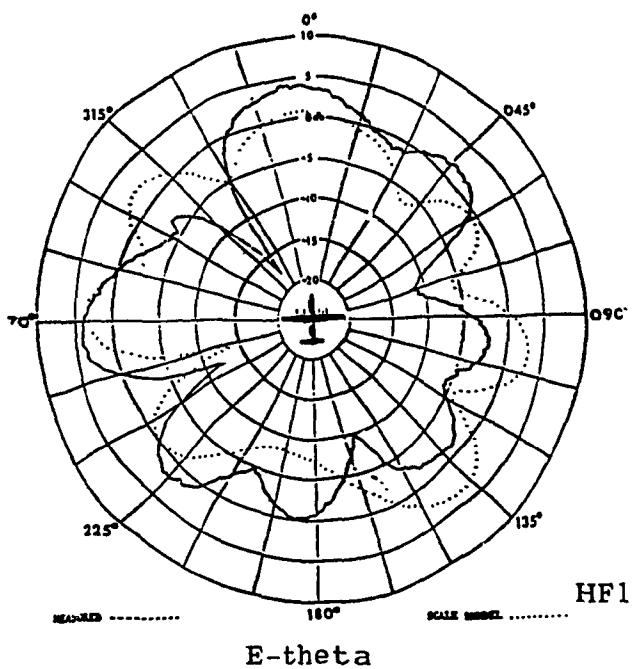
Frequency - 14.00 MHz



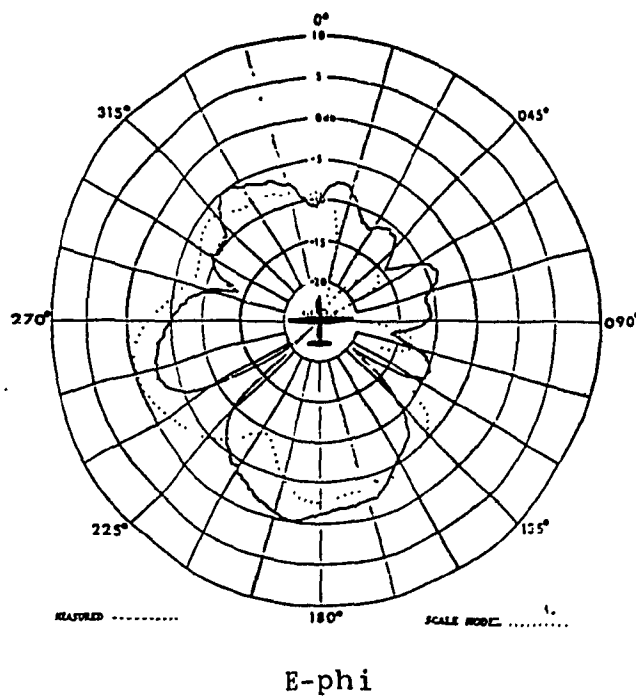
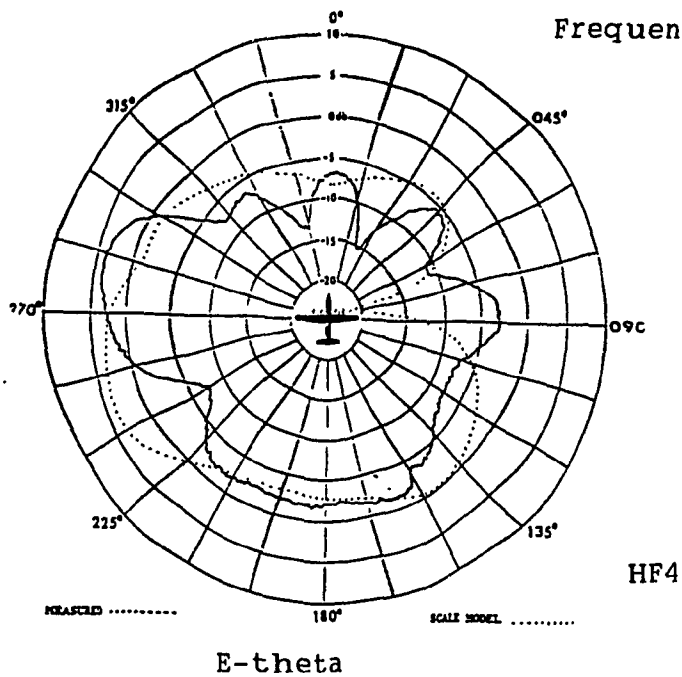


Frequency - 20.00 MHz



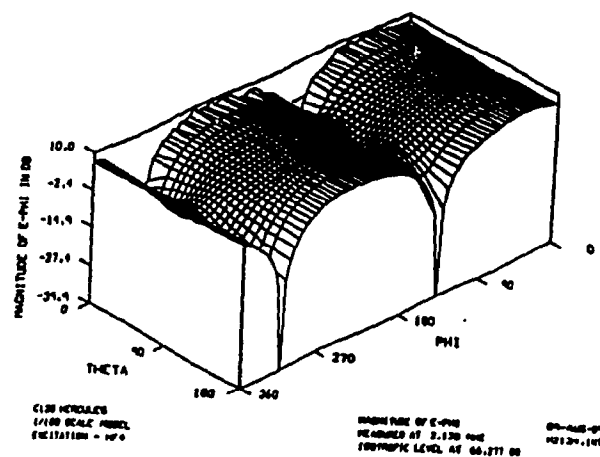
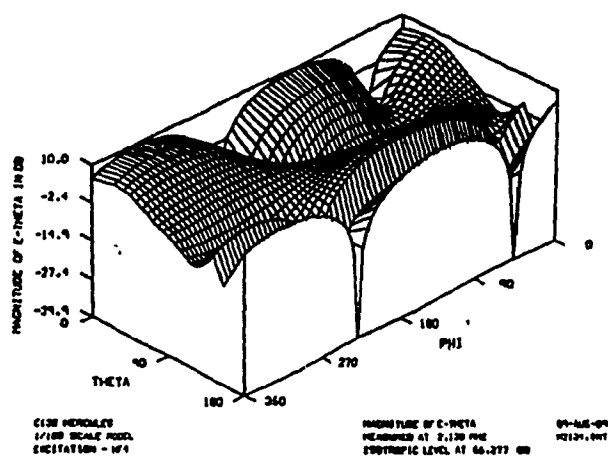
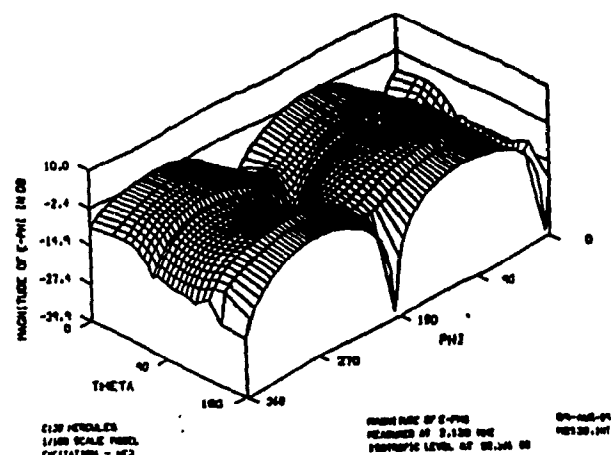
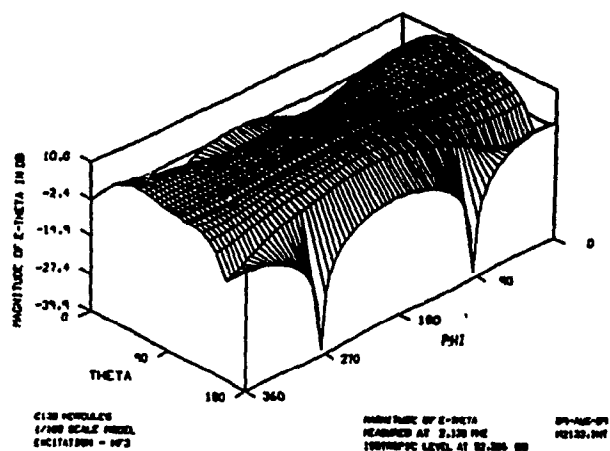
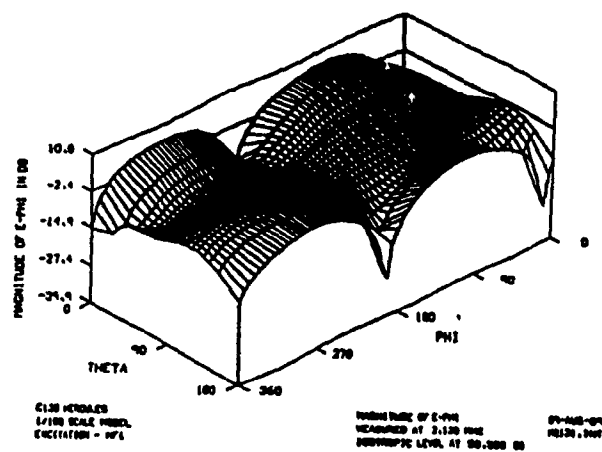
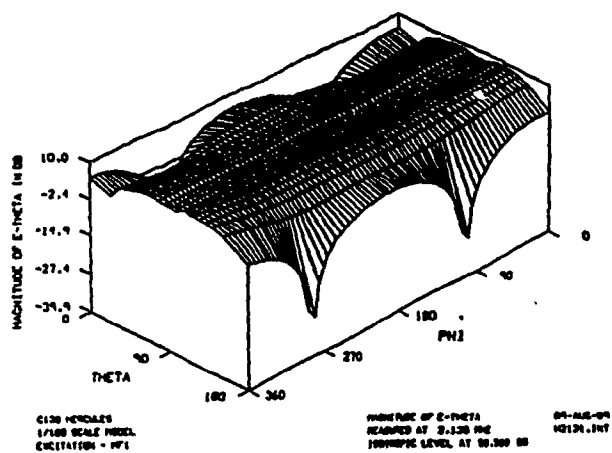


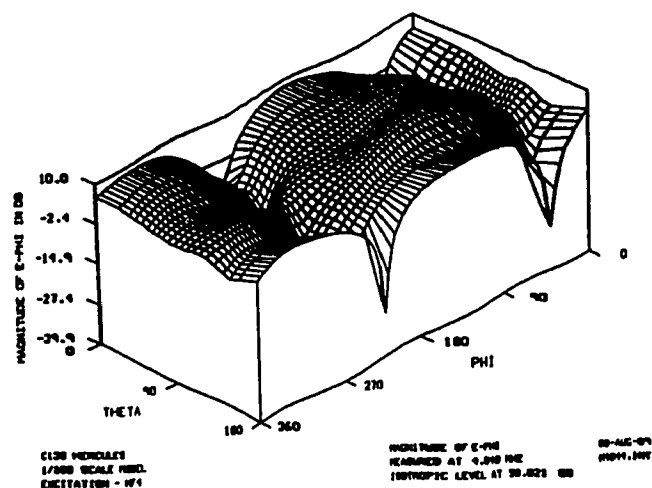
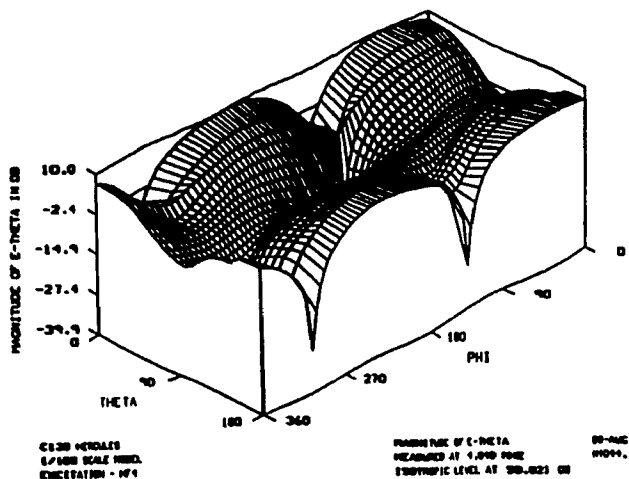
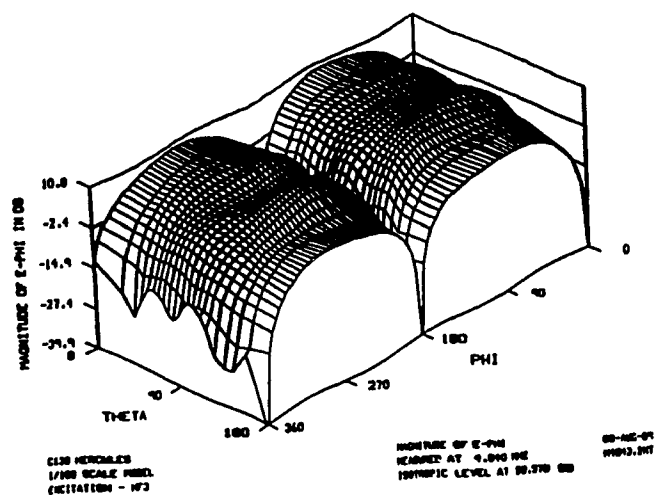
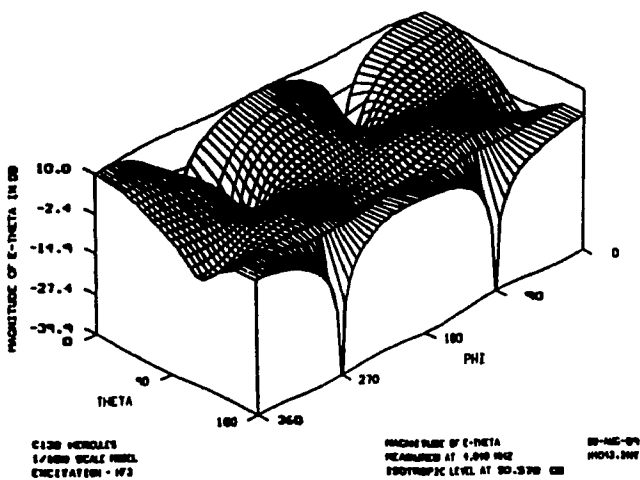
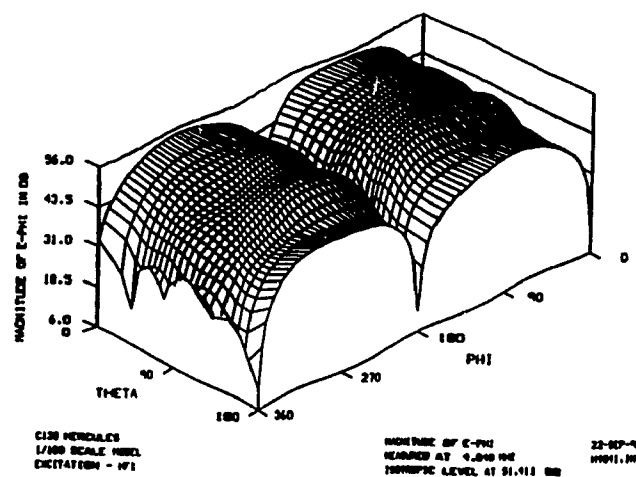
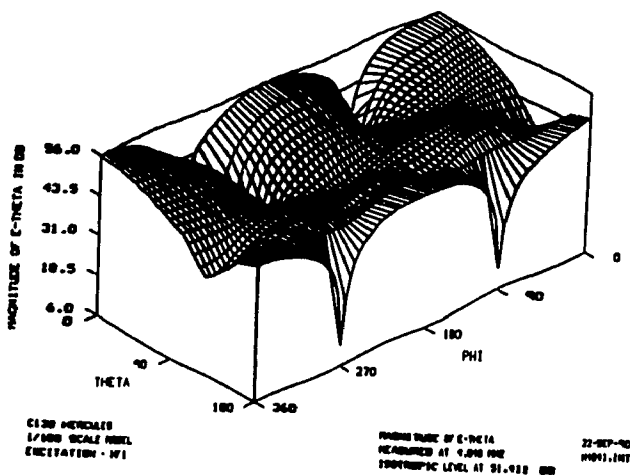
Frequency - 26.00 MHz

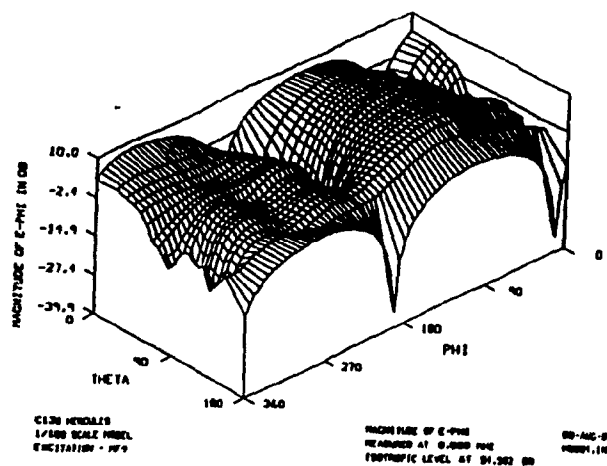
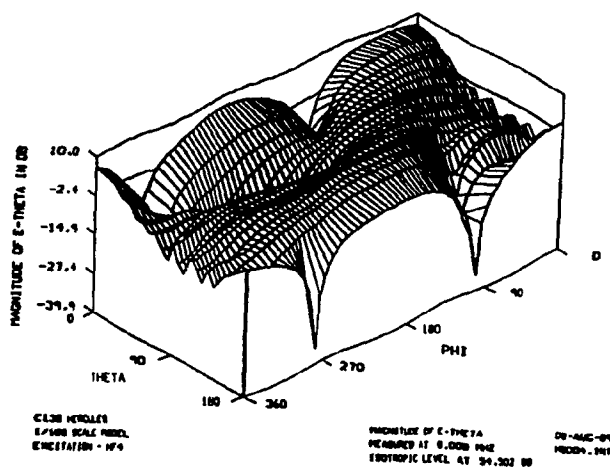
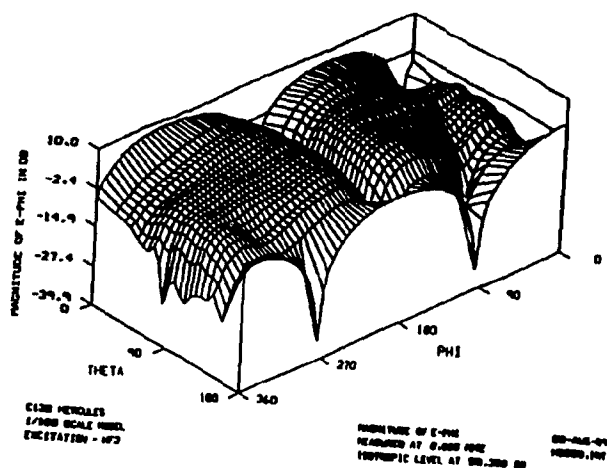
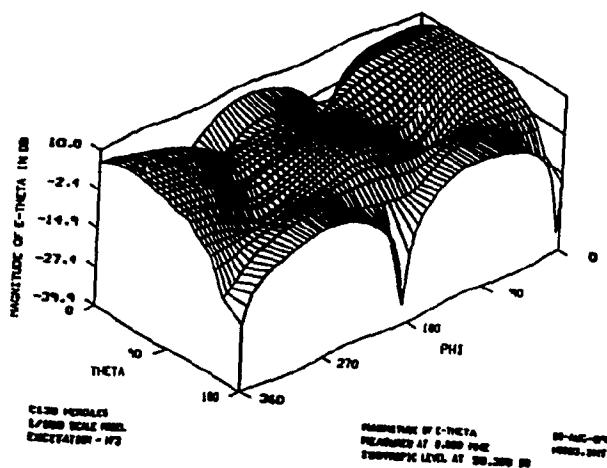
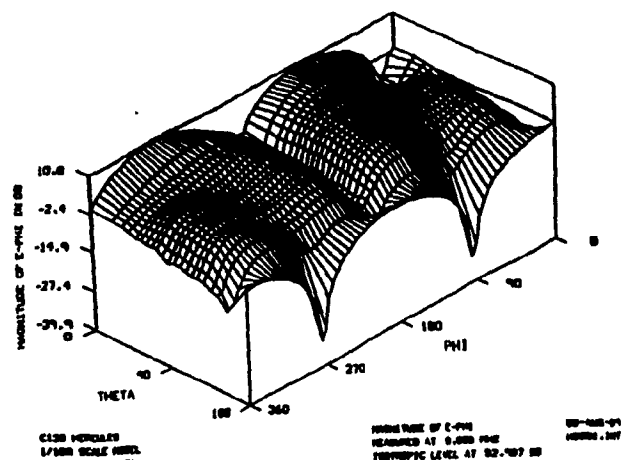
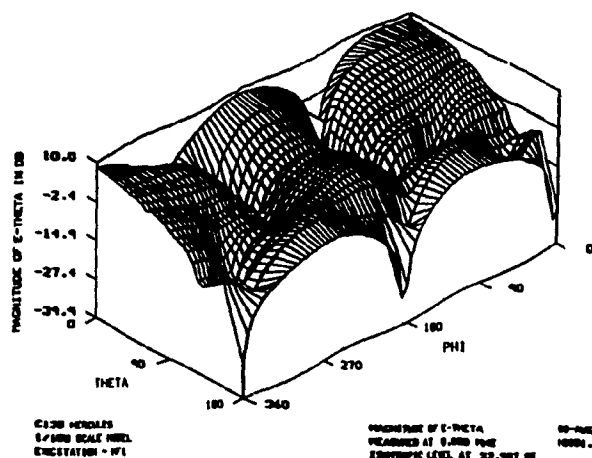


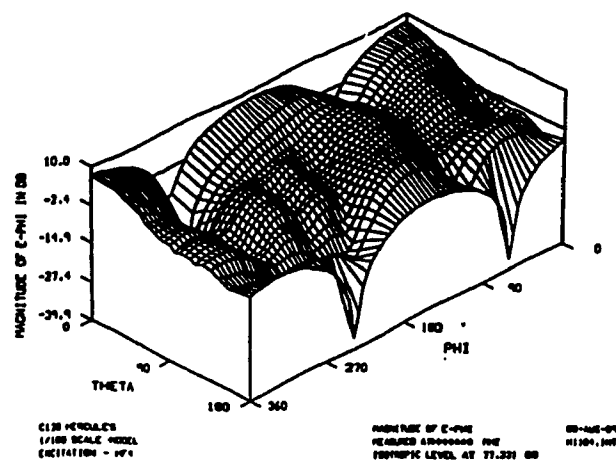
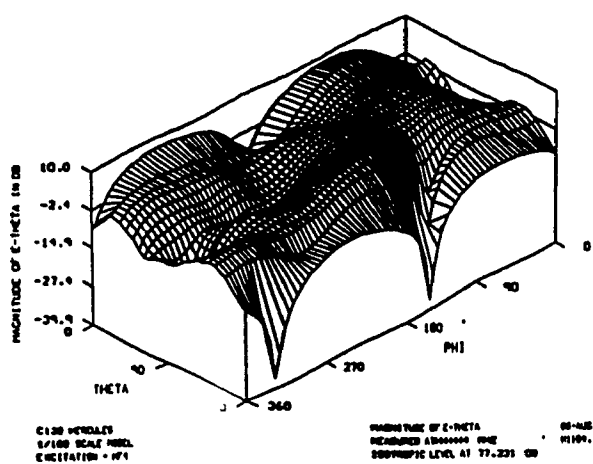
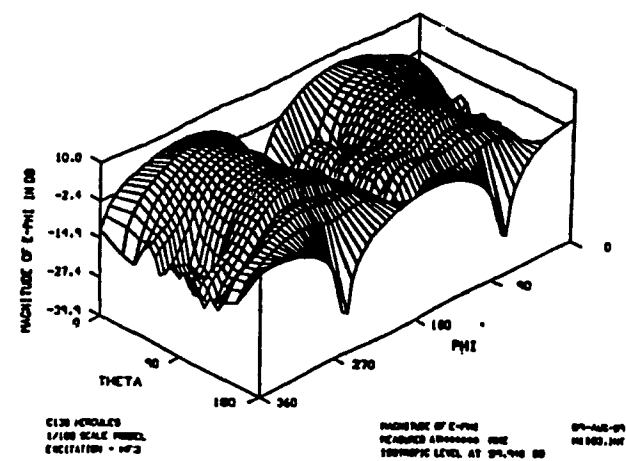
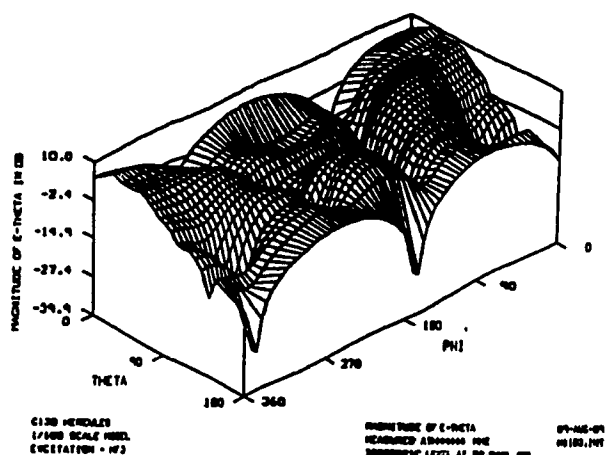
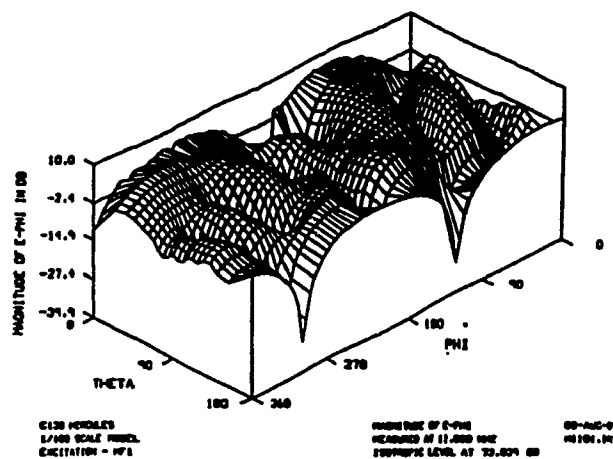
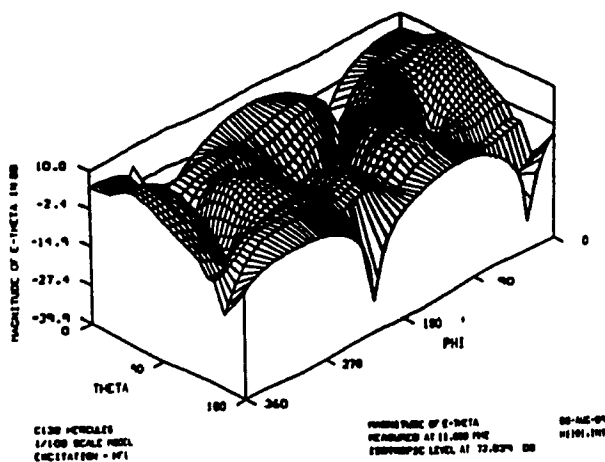
APPENDIX B

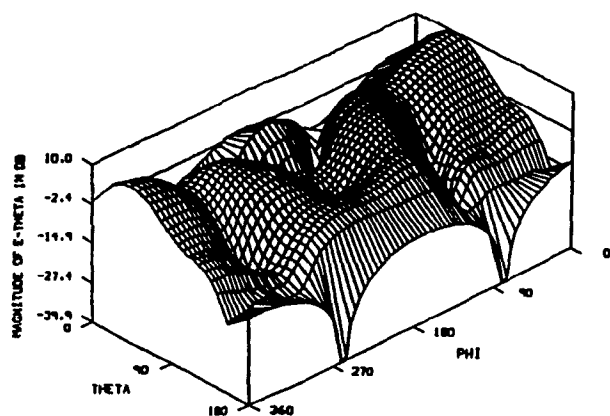
Appendix B contains the scale model measurements of antennas HF1, HF3 and HF4 over the HF band.







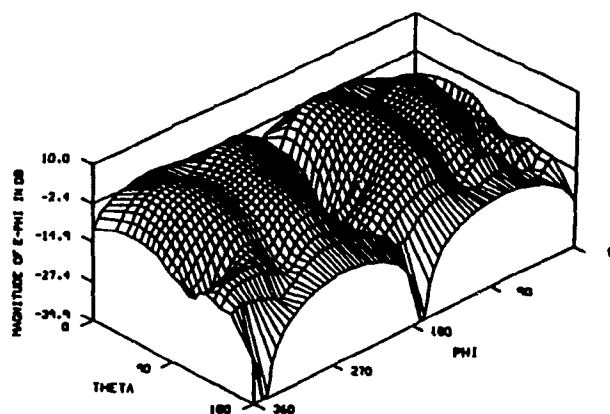




C130 MODALES
1/100 SCALE MODEL
EXCITATION - W1

MAGNITUDE OF E-THETA
MEASURED AT 14,000 PPM
ISOTHERMIC LEVEL AT 52,400 DB

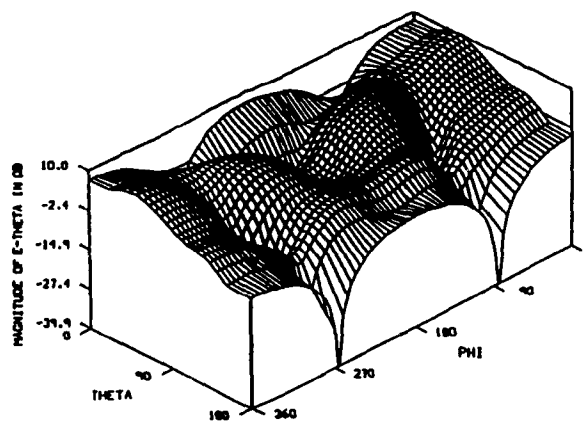
00-AUG-89
H1401,INT



C130 MODALES
1/100 SCALE MODEL
EXCITATION - W1

MAGNITUDE OF E-PHI
MEASURED AT 14,000 PPM
ISOTHERMIC LEVEL AT 52,400 DB

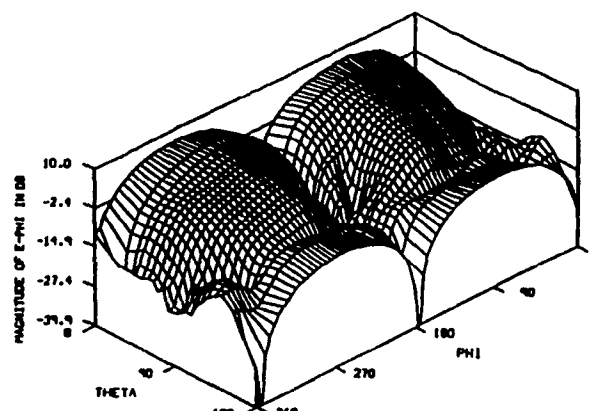
00-AUG-89
H1401,INT



C130 MODALES
1/100 SCALE MODEL
EXCITATION - W2

MAGNITUDE OF E-THETA
MEASURED AT 14,000 PPM
ISOTHERMIC LEVEL AT 59,636 DB

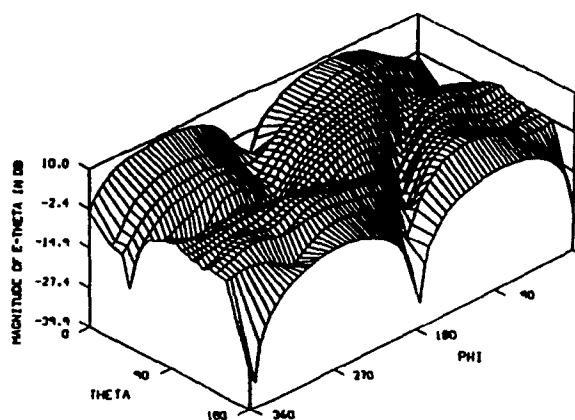
00-AUG-89
H1402,INT



C130 MODALES
1/100 SCALE MODEL
EXCITATION - W2

MAGNITUDE OF E-PHI
MEASURED AT 14,000 PPM
ISOTHERMIC LEVEL AT 59,636 DB

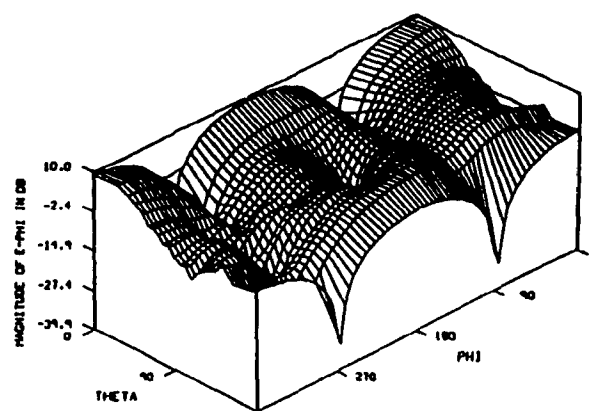
00-AUG-89
H1402,INT



C130 MODALES
1/100 SCALE MODEL
EXCITATION - W4

MAGNITUDE OF E-THETA
MEASURED AT 14,000 PPM
ISOTHERMIC LEVEL AT 50,406 DB

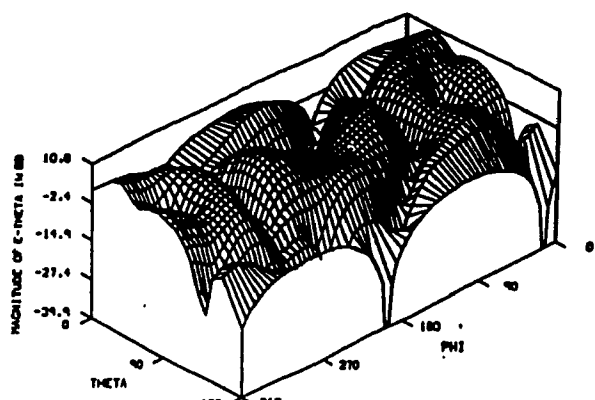
09-AUG-89
H1404,INT



C130 MODALES
1/100 SCALE MODEL
EXCITATION - W4

MAGNITUDE OF E-PHI
MEASURED AT 14,000 PPM
ISOTHERMIC LEVEL AT 50,406 DB

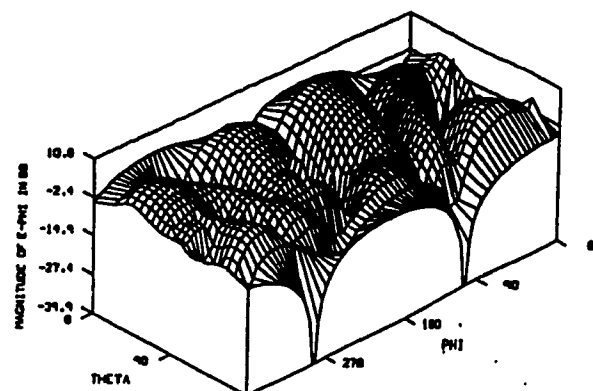
09-AUG-89
H1404,INT



C130 HERCULES
1/100 SCALE MODEL
EXCITATION - HF1

MAGNITUDE OF E-THETA
MEASURED AT 17.000 MHz
ISOTHERMIC LEVEL AT 51.440 dB

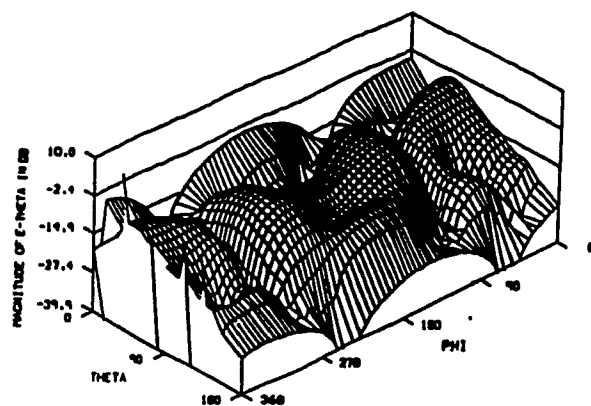
00-445-09
M1701.107



C130 HERCULES
1/100 SCALE MODEL
EXCITATION - HF1

MAGNITUDE OF E-PHI
MEASURED AT 17.000 MHz
ISOTHERMIC LEVEL AT 51.440 dB

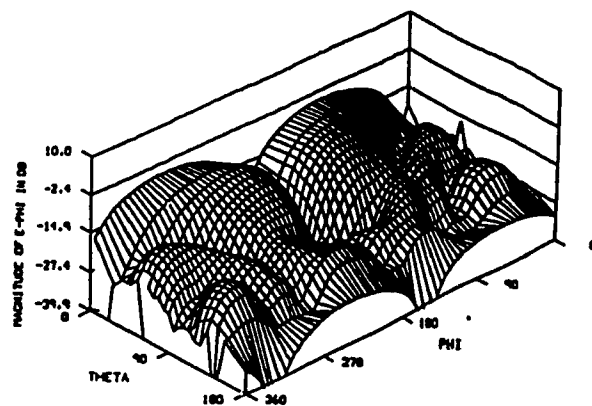
00-445-09
M1701.107



C130 HERCULES
1/100 SCALE MODEL
EXCITATION - HF2

MAGNITUDE OF E-THETA
MEASURED AT 17.000 MHz
ISOTHERMIC LEVEL AT 47.304 dB

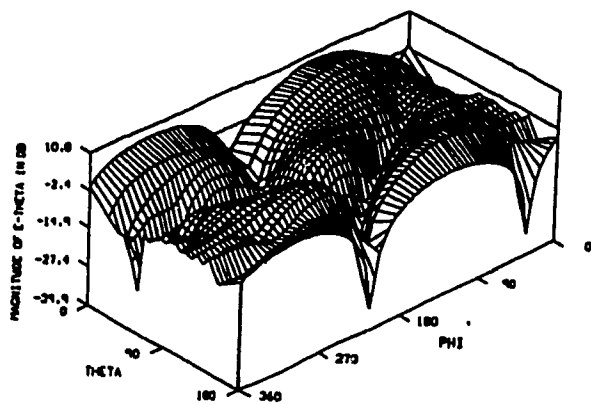
00-445-09
M1700.107



C130 HERCULES
1/100 SCALE MODEL
EXCITATION - HF2

MAGNITUDE OF E-PHI
MEASURED AT 17.000 MHz
ISOTHERMIC LEVEL AT 47.304 dB

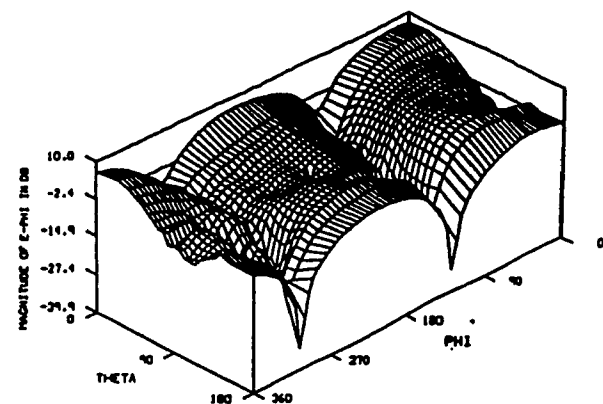
00-445-09
M1700.107



C130 HERCULES
1/100 SCALE MODEL
EXCITATION - HF4

MAGNITUDE OF E-THETA
MEASURED AT 17.000 MHz
ISOTHERMIC LEVEL AT 52.041 dB

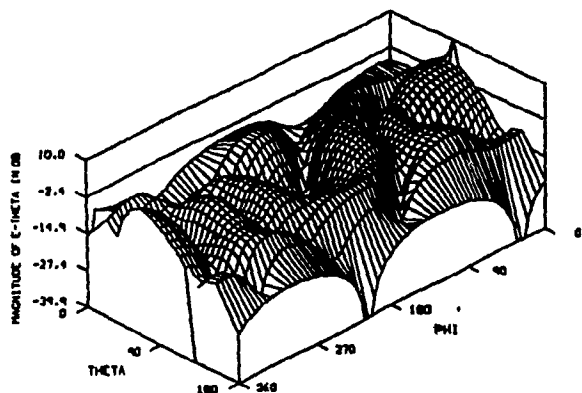
00-445-09
M1704.107



C130 HERCULES
1/100 SCALE MODEL
EXCITATION - HF4

MAGNITUDE OF E-PHI
MEASURED AT 17.000 MHz
ISOTHERMIC LEVEL AT 52.041 dB

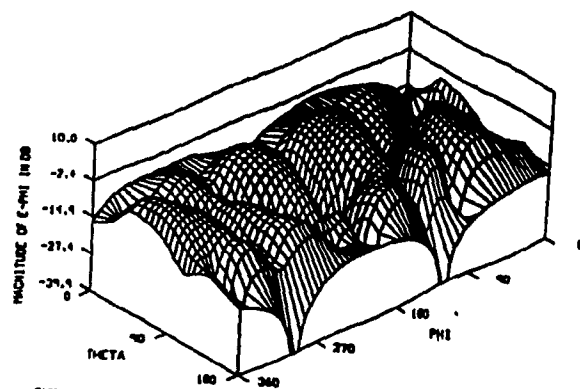
00-445-09
M1704.107



C130 HERCULES
1/100 SCALE MODEL
EXCITATION - HF1

MAGNITUDE OF E-THETA
MEASURED AT 40,000 HZ
ISOTHERMIC LEVEL AT 40,000 DB

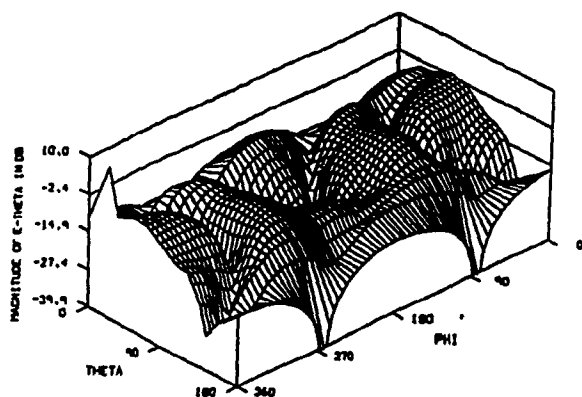
00-AUG-69
NORON,INT



C130 HERCULES
1/100 SCALE MODEL
EXCITATION - HF1

MAGNITUDE OF E-PHI
MEASURED AT 40,000 HZ
ISOTHERMIC LEVEL AT 40,000 DB

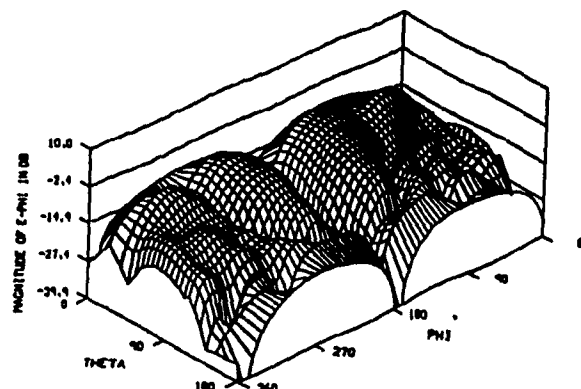
00-AUG-69
NORON,INT



C130 HERCULES
1/100 SCALE MODEL
EXCITATION - HF2

MAGNITUDE OF E-THETA
MEASURED AT 43,107 HZ
ISOTHERMIC LEVEL AT 43,107 DB

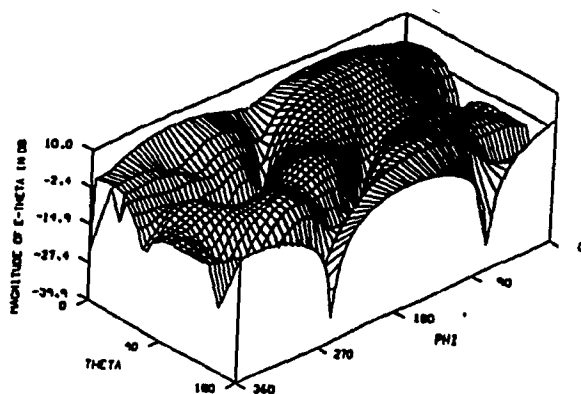
00-AUG-69
NORON,INT



C130 HERCULES
1/100 SCALE MODEL
EXCITATION - HF2

MAGNITUDE OF E-PHI
MEASURED AT 43,107 HZ
ISOTHERMIC LEVEL AT 43,107 DB

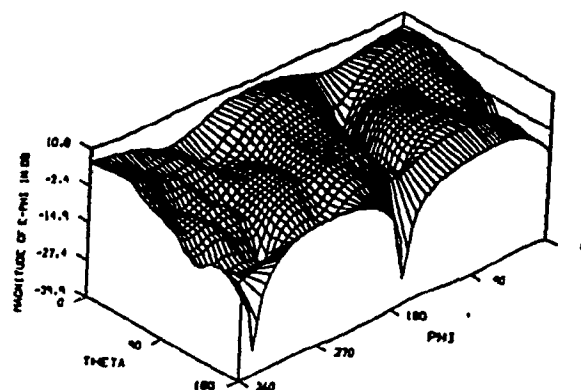
00-AUG-69
NORON,INT



C130 HERCULES
1/100 SCALE MODEL
EXCITATION - HF3

MAGNITUDE OF E-THETA
MEASURED AT 53,006 HZ
ISOTHERMIC LEVEL AT 53,006 DB

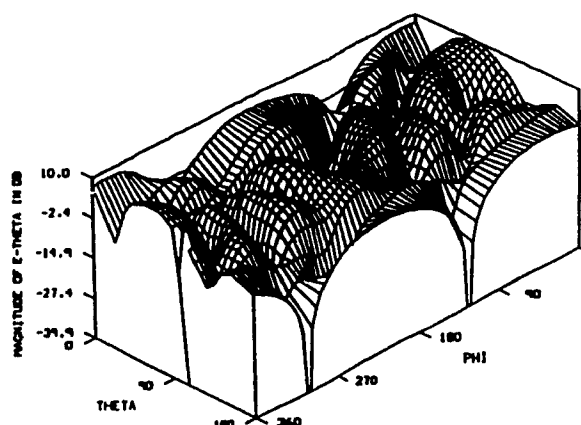
00-AUG-69
NORON,INT



C130 HERCULES
1/100 SCALE MODEL
EXCITATION - HF3

MAGNITUDE OF E-PHI
MEASURED AT 53,006 HZ
ISOTHERMIC LEVEL AT 53,006 DB

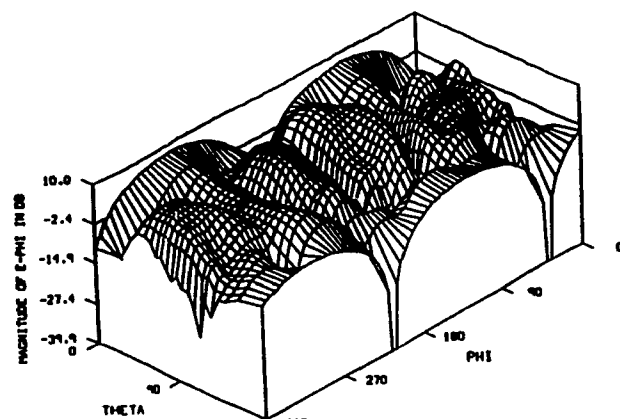
00-AUG-69
NORON,INT



C130 HERCULES
1/100 SCALE MODEL
EXCITATION - W1

HIGHEST PEAK OF E-THETA
MEASURED AT 23.000 MHz
ISOTROPIC LEVEL AT 50.303 dB

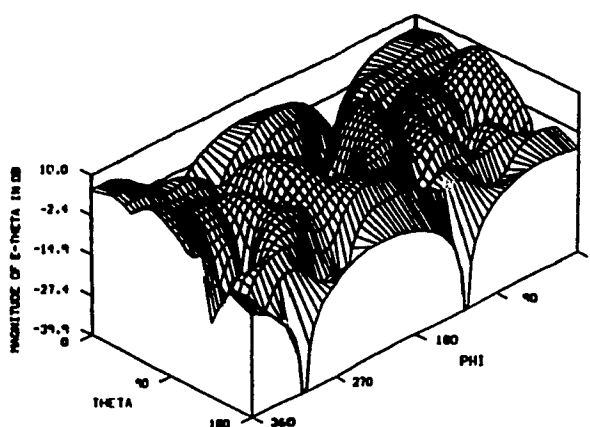
00-AUG-09
V2301.INT



C130 HERCULES
1/100 SCALE MODEL
EXCITATION - W1

HIGHEST PEAK OF E-PHI
MEASURED AT 23.000 MHz
ISOTROPIC LEVEL AT 50.303 dB

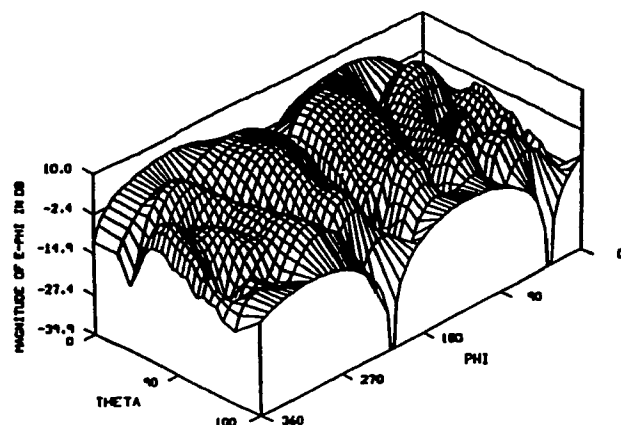
00-AUG-09
V2301.INT



C130 HERCULES
1/100 SCALE MODEL
EXCITATION - W2

HIGHEST PEAK OF E-THETA
MEASURED AT 23.000 MHz
ISOTROPIC LEVEL AT 51.641 dB

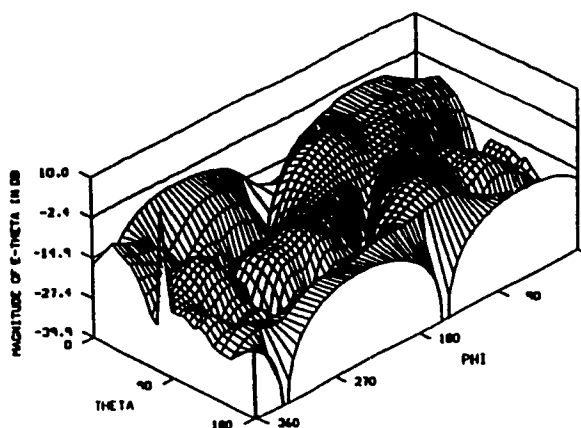
00-AUG-09
V2301.INT



C130 HERCULES
1/100 SCALE MODEL
EXCITATION - W2

HIGHEST PEAK OF E-PHI
MEASURED AT 23.000 MHz
ISOTROPIC LEVEL AT 51.641 dB

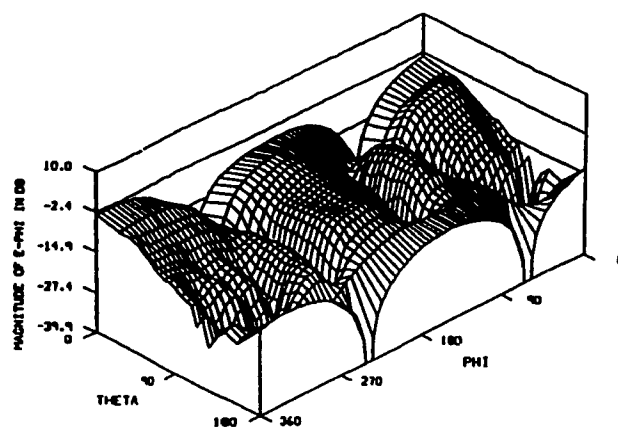
00-AUG-09
V2301.INT



C130 HERCULES
1/100 SCALE MODEL
EXCITATION - W4

HIGHEST PEAK OF E-THETA
MEASURED AT 23.000 MHz
ISOTROPIC LEVEL AT 49.100 dB

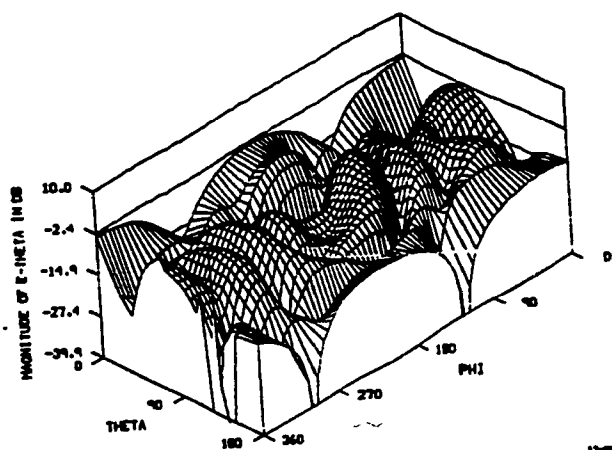
00-AUG-09
V2304.INT



C130 HERCULES
1/100 SCALE MODEL
EXCITATION - W4

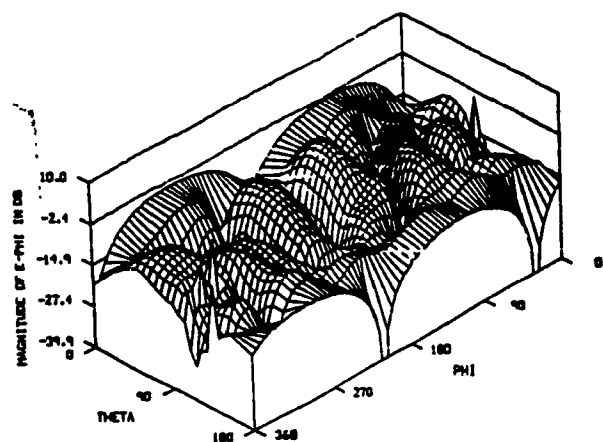
HIGHEST PEAK OF E-PHI
MEASURED AT 23.000 MHz
ISOTROPIC LEVEL AT 49.100 dB

00-AUG-09
V2304.INT



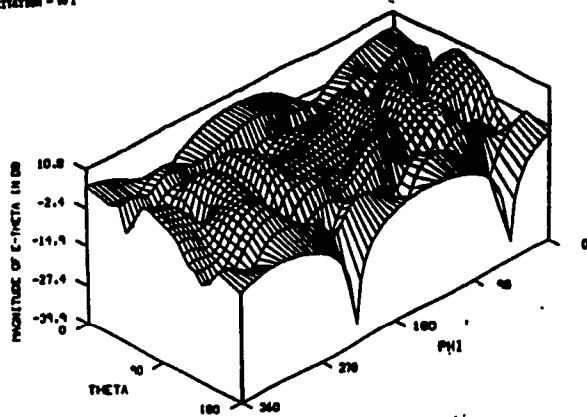
13-100-01
1/100 SCALE MODEL
EXCITATION - HF1

MAGNITUDE OF E-THETA
MEASURED AT 20.000 MHz
ISOTHERMIC LEVEL AT 40.000 dB



13-100-01
1/100 SCALE MODEL
EXCITATION - HF1

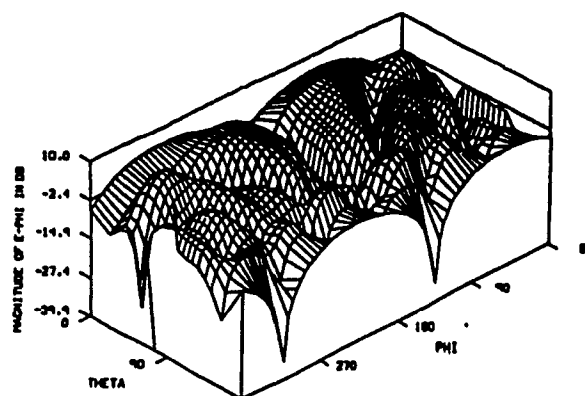
MAGNITUDE OF E-PHI
MEASURED AT 20.000 MHz
ISOTHERMIC LEVEL AT 40.000 dB



07-100-01
1/100 SCALE MODEL
EXCITATION - HF2

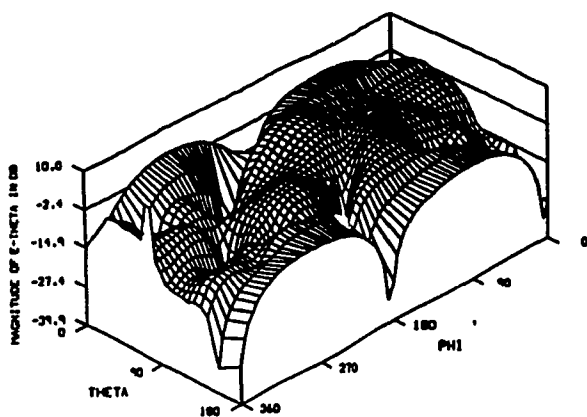
MAGNITUDE OF E-THETA
MEASURED AT 20.000 MHz
ISOTHERMIC LEVEL AT 40.000 dB

07-100-01
1/100 SCALE MODEL
EXCITATION - HF2



07-100-01
1/100 SCALE MODEL
EXCITATION - HF2

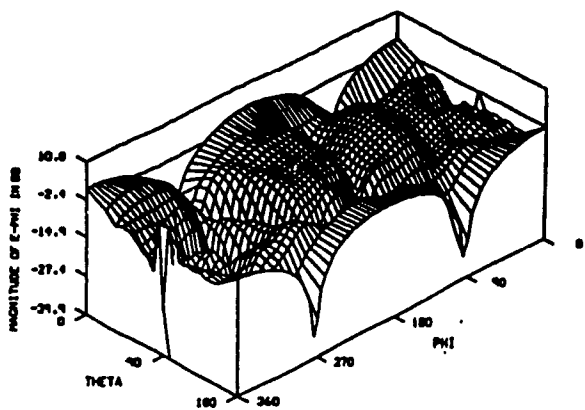
MAGNITUDE OF E-PHI
MEASURED AT 20.000 MHz
ISOTHERMIC LEVEL AT 40.000 dB



07-100-01
1/100 SCALE MODEL
EXCITATION - HF3

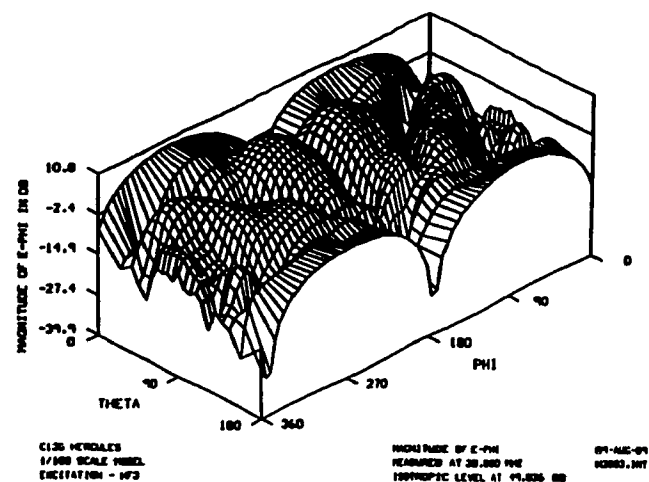
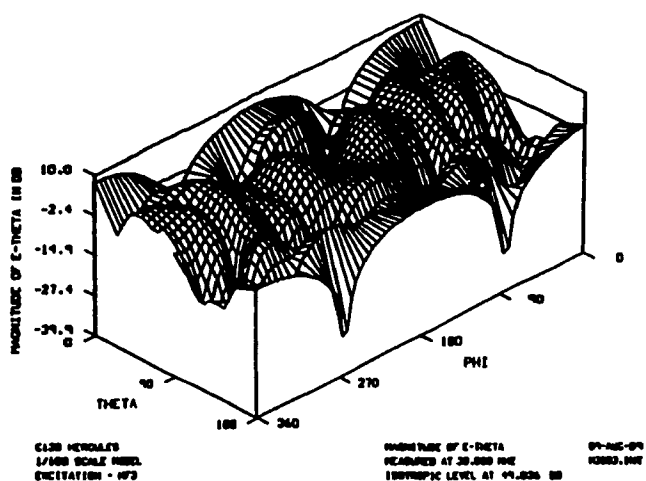
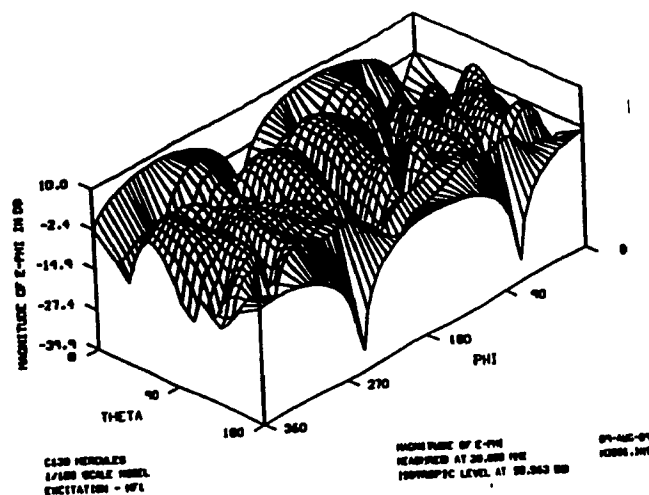
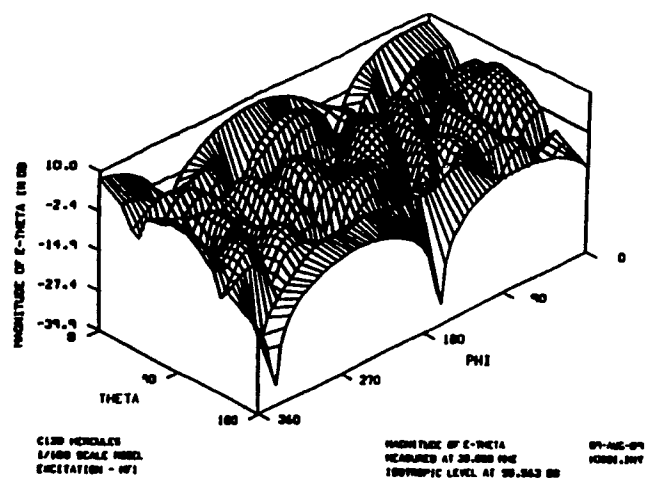
MAGNITUDE OF E-THETA
MEASURED AT 20.000 MHz
ISOTHERMIC LEVEL AT 40.000 dB

07-100-01
1/100 SCALE MODEL
EXCITATION - HF3



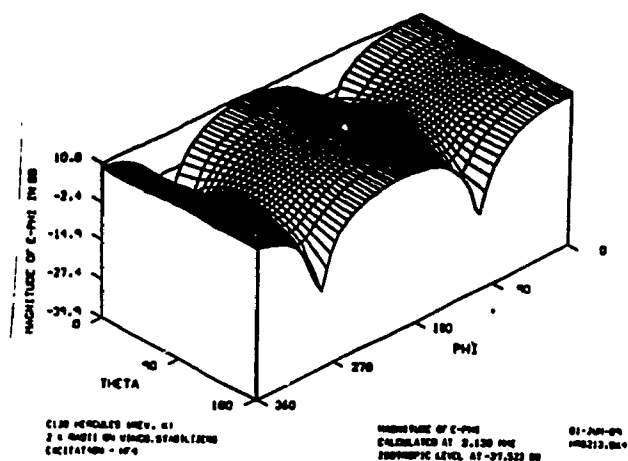
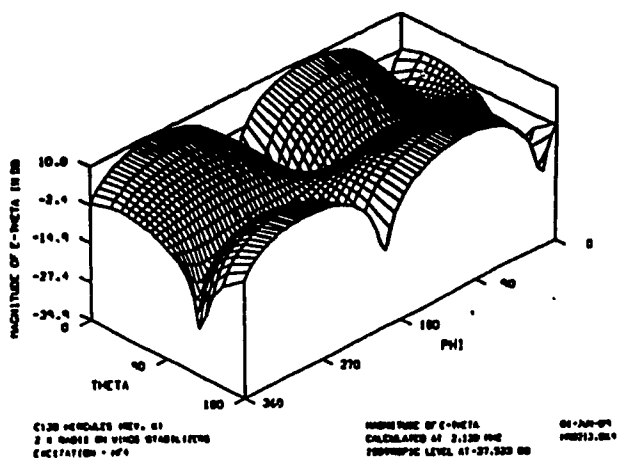
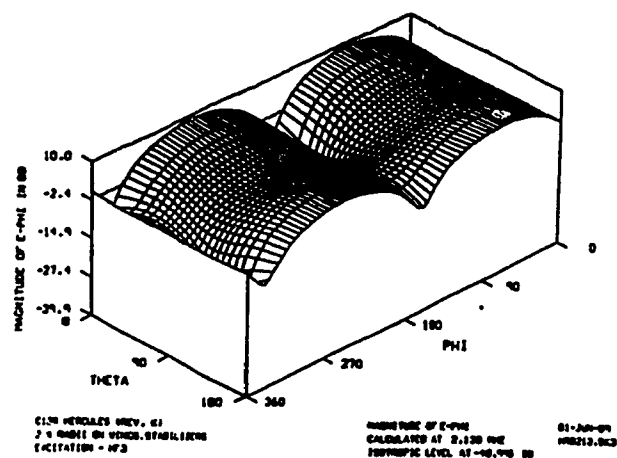
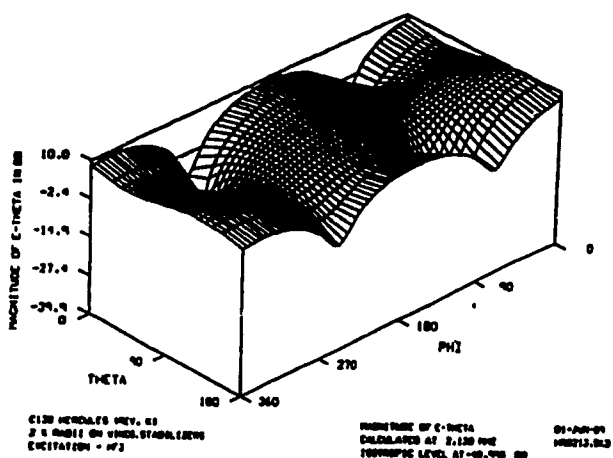
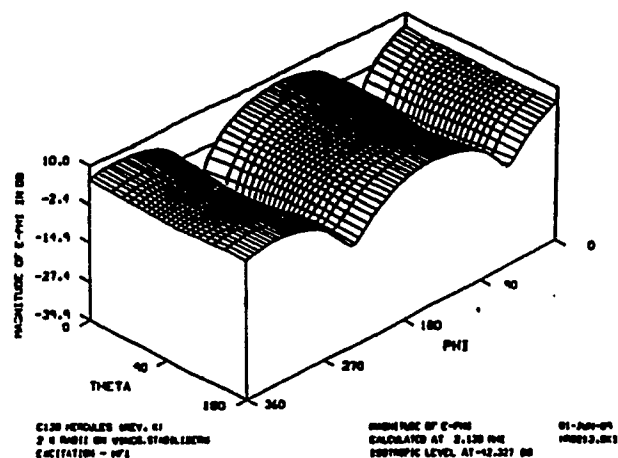
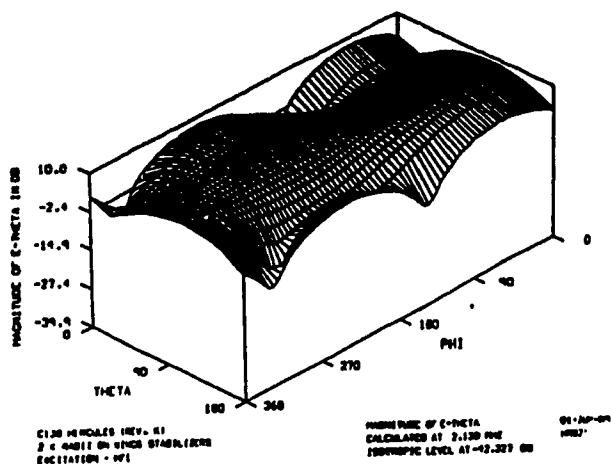
07-100-01
1/100 SCALE MODEL
EXCITATION - HF3

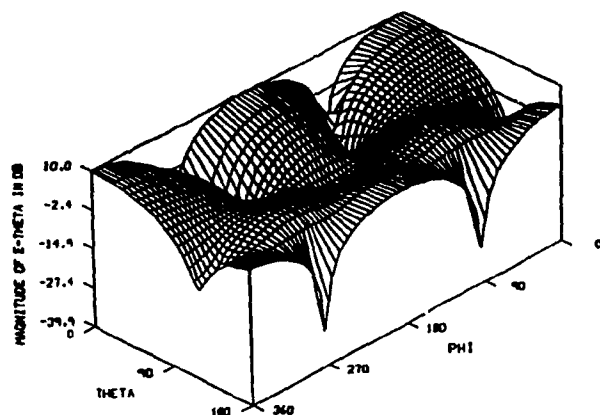
MAGNITUDE OF E-PHI
MEASURED AT 20.000 MHz
ISOTHERMIC LEVEL AT 40.000 dB



APPENDIX C

Appendix C consists of the radiation patterns of antennas HF1, HF3 and HF4 for wire grid model K. The frequency of operation ranges from 2.13 to 30.0 MHz.

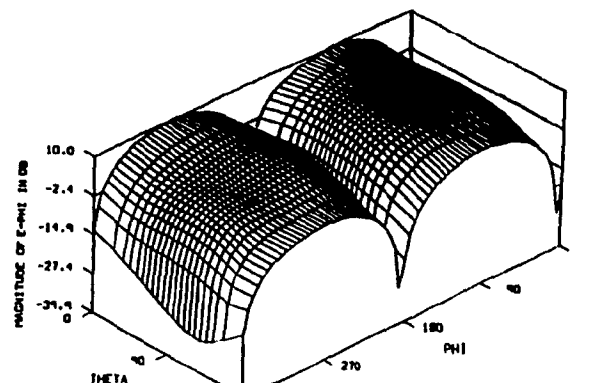




C130 HERCULES MEV. A1
2 H RADI ON VINC. STABILIZER
EXCITATION - HP1

MAGNITUDE OF E-THETA
CALCULATED AT 1.040 MHz
ISOTROPIC LEVEL AT -12.231 dB

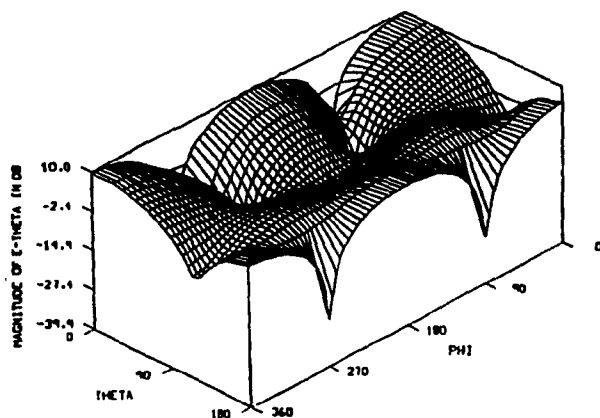
01-JUN-09
H00009,001



C130 HERCULES MEV. A1
2 H RADI ON VINC. STABILIZER
EXCITATION - HP1

MAGNITUDE OF E-PHI
CALCULATED AT 1.040 MHz
ISOTROPIC LEVEL AT 12.231 dB

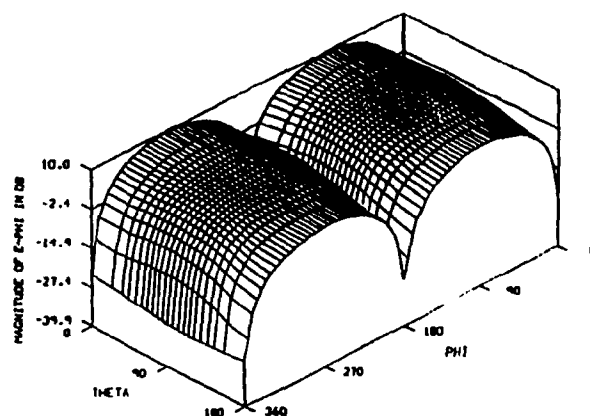
01-JUN-09
H00009,001



C130 HERCULES MEV. A1
2 H RADI ON VINC. STABILIZER
EXCITATION - HP2

MAGNITUDE OF E-THETA
CALCULATED AT 1.040 MHz
ISOTROPIC LEVEL AT -9.977 dB

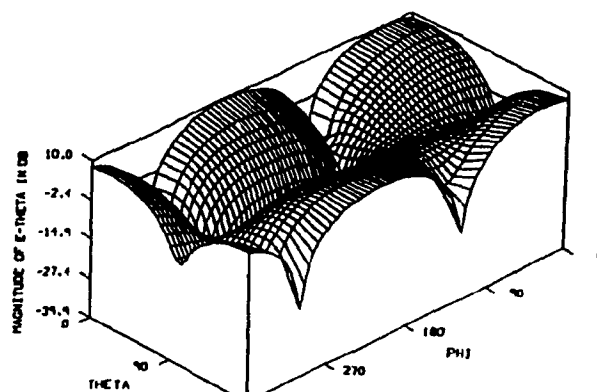
01-JUN-09
H00009,002



C130 HERCULES MEV. A1
2 H RADI ON VINC. STABILIZER
EXCITATION - HP2

MAGNITUDE OF E-PHI
CALCULATED AT 1.040 MHz
ISOTROPIC LEVEL AT 9.977 dB

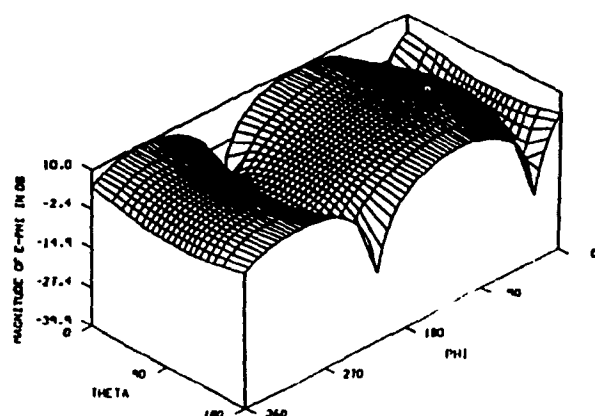
01-JUN-09
H00009,002



C130 HERCULES MEV. A1
2 H RADI ON VINC. STABILIZER
EXCITATION - HP4

MAGNITUDE OF E-THETA
CALCULATED AT 1.040 MHz
ISOTROPIC LEVEL AT -9.422 dB

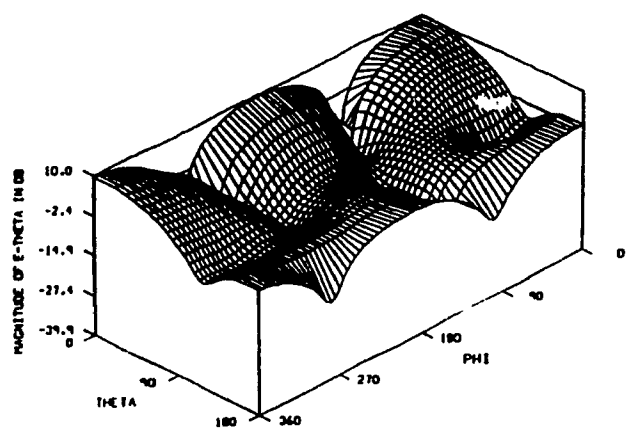
01-JUN-09
H00009,004



C130 HERCULES MEV. A1
2 H RADI ON VINC. STABILIZER
EXCITATION - HP4

MAGNITUDE OF E-PHI
CALCULATED AT 1.040 MHz
ISOTROPIC LEVEL AT 9.422 dB

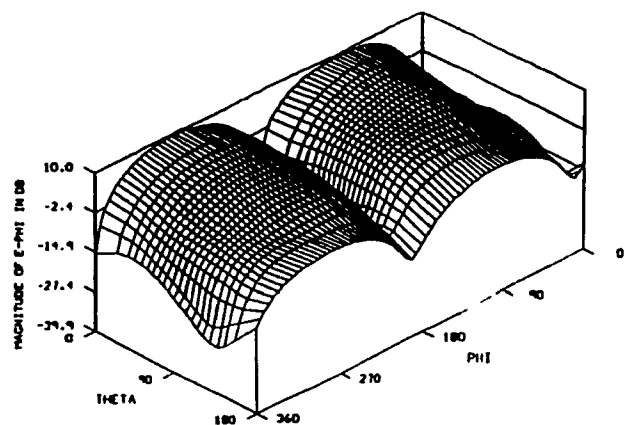
01-JUN-09
H00009,004



C130 HERCULES (REV. K1)
2 X RADII ON VEHIC STABILIZERS
EXCITATION - HP1

MAGNITUDE OF E-THETA
CALCULATED AT 0.000 PNE
ISOTROPIC LEVEL AT -24.304 DB

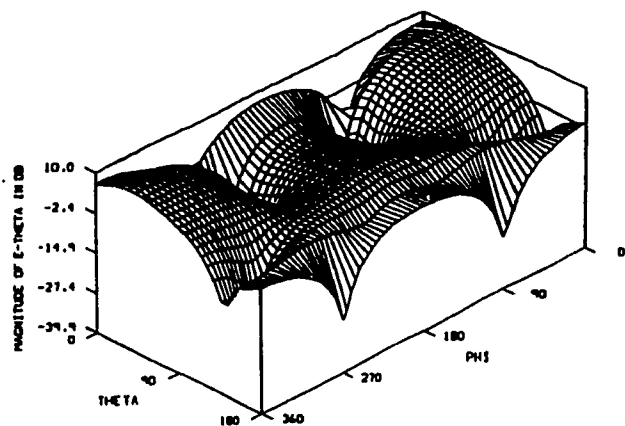
01-JUN-89
H00000,001



C130 HERCULES (REV. K1)
2 X RADII ON VEHIC STABILIZERS
EXCITATION - HP1

MAGNITUDE OF E-PHI
CALCULATED AT 0.000 PNE
ISOTROPIC LEVEL AT -24.304 DB

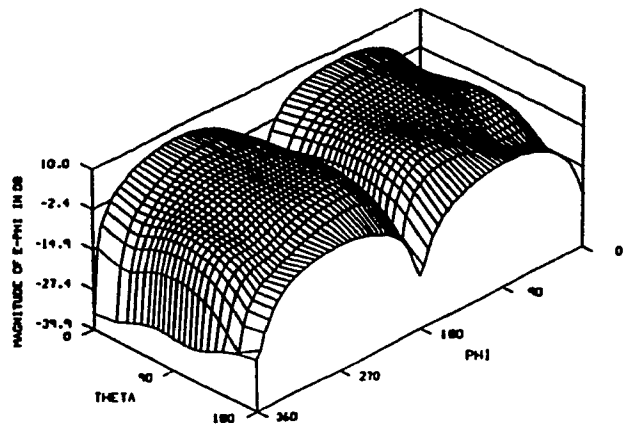
01-JUN-89
H00000,001



C130 HERCULES (REV. K1)
2 X RADII ON VEHIC STABILIZERS
EXCITATION - HP2

MAGNITUDE OF E-THETA
CALCULATED AT 0.000 PNE
ISOTROPIC LEVEL AT -23.125 DB

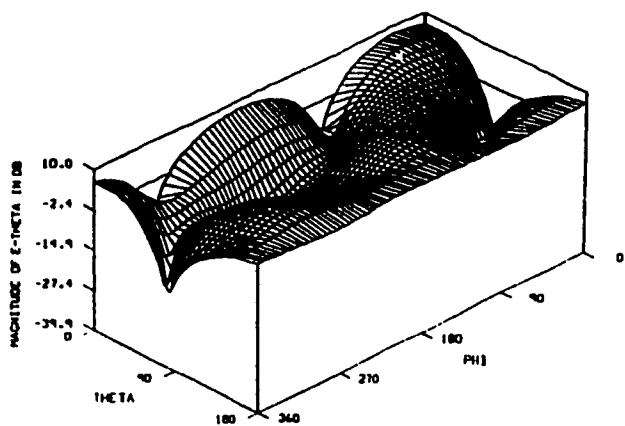
01-JUN-89
H00000,002



C130 HERCULES (REV. K1)
2 X RADII ON VEHIC STABILIZERS
EXCITATION - HP2

MAGNITUDE OF E-PHI
CALCULATED AT 0.000 PNE
ISOTROPIC LEVEL AT -23.125 DB

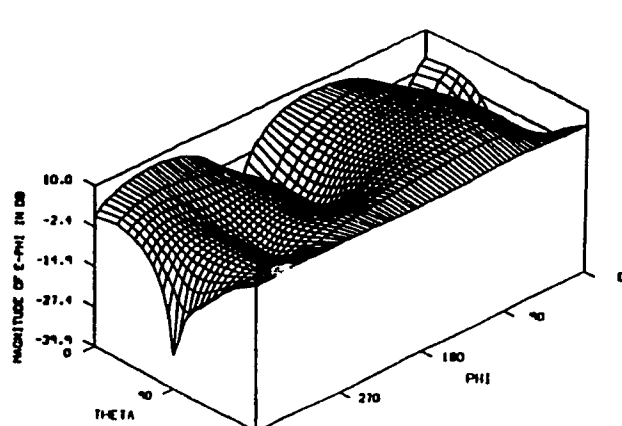
01-JUN-89
H00000,002



C130 HERCULES (REV. K1)
2 X RADII ON VEHIC STABILIZERS
EXCITATION - HP4

MAGNITUDE OF E-THETA
CALCULATED AT 0.000 PNE
ISOTROPIC LEVEL AT -24.110 DB

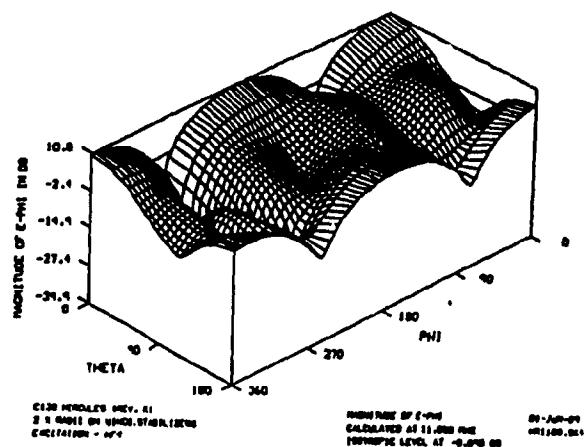
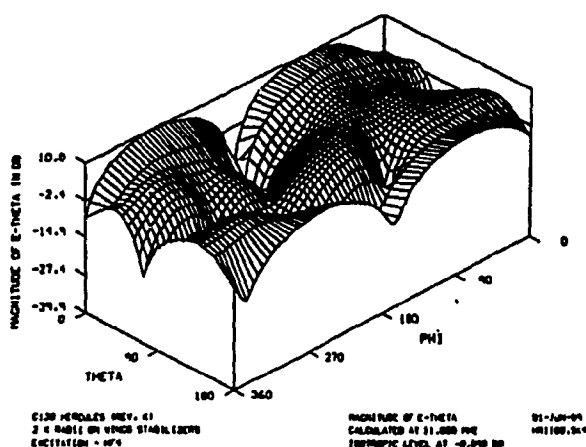
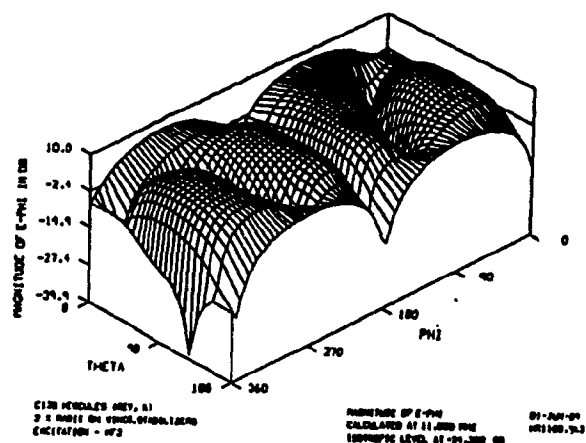
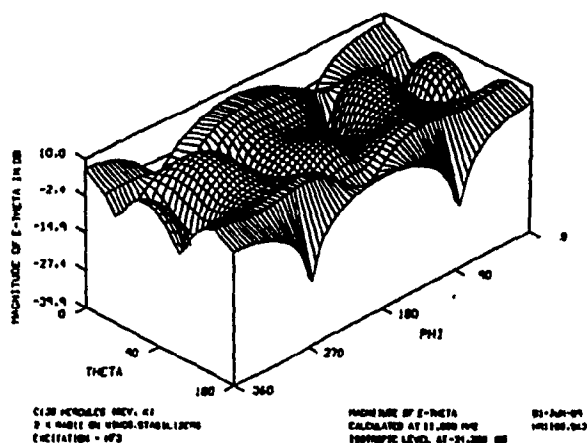
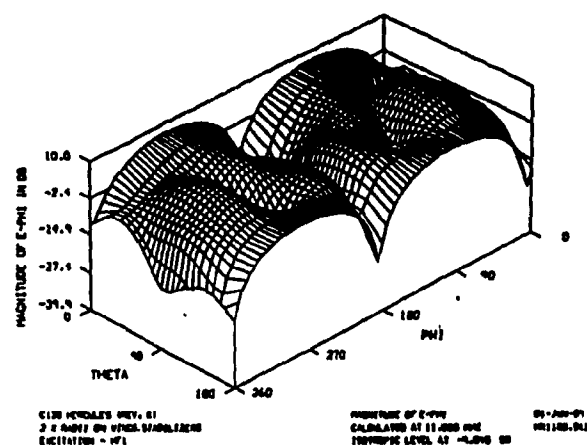
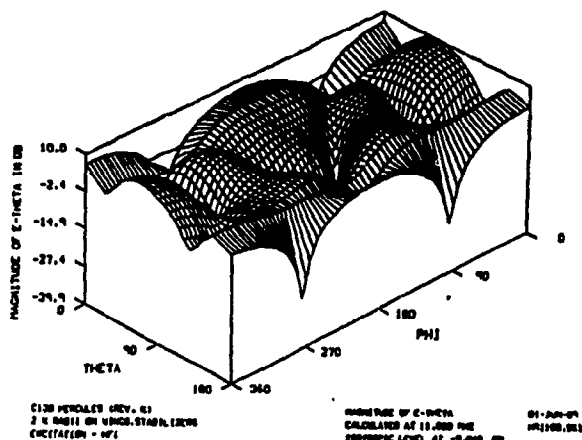
01-JUN-89
H00000,004

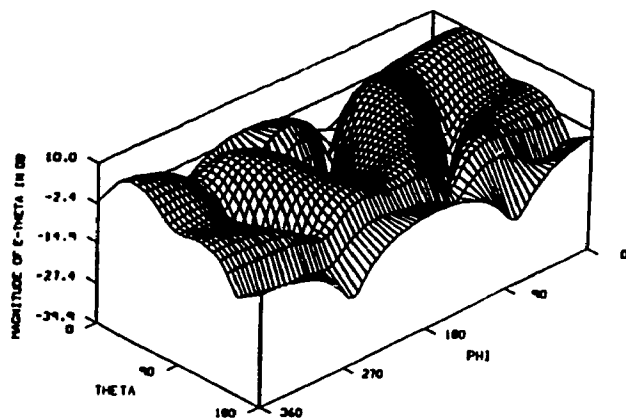


C130 HERCULES (REV. K1)
2 X RADII ON VEHIC STABILIZERS
EXCITATION - HP4

MAGNITUDE OF E-PHI
CALCULATED AT 0.000 PNE
ISOTROPIC LEVEL AT -24.110 DB

01-JUN-89
H00000,004

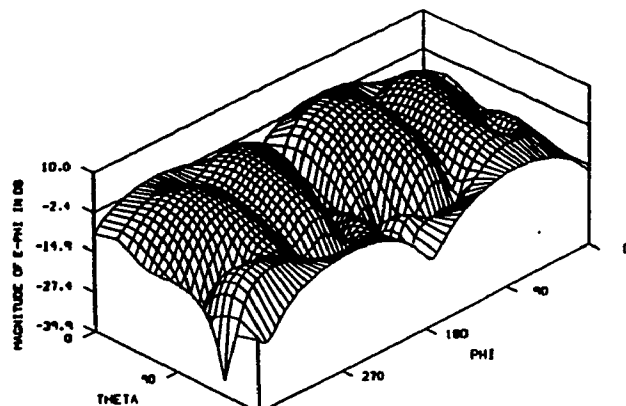




C130 HERCULES MEV. 41
2 X RADII ON VINC. STABILIZERS
EXCITATION - HF1

MAGNITUDE OF e -THETA
CALCULATED AT 14,000 HZ
ISOTROPIC LEVEL AT -10.916 DB

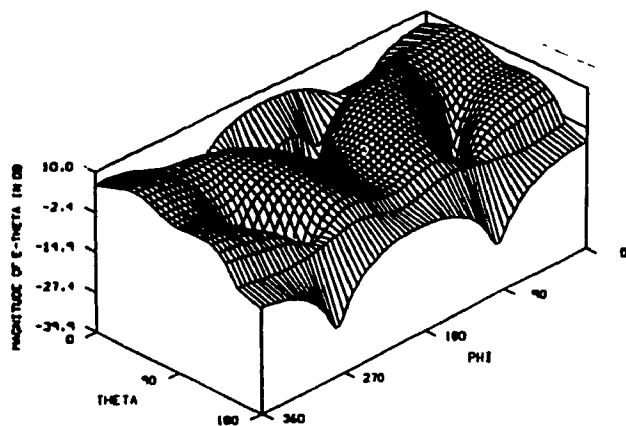
01-JUN-89
HR1400.061



C130 HERCULES MEV. 41
2 X RADII ON VINC. STABILIZERS
EXCITATION - HF1

MAGNITUDE OF e -PHI
CALCULATED AT 14,000 HZ
ISOTROPIC LEVEL AT -10.916 DB

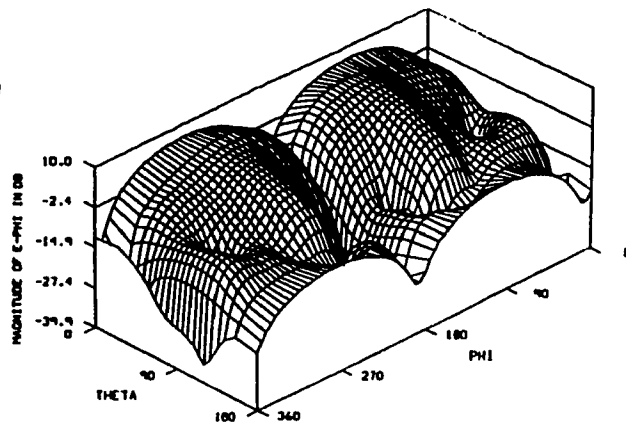
01-JUN-89
HR1400.061



C130 HERCULES MEV. 41
2 X RADII ON VINC. STABILIZERS
EXCITATION - HF3

MAGNITUDE OF e -THETA
CALCULATED AT 3,517 HZ
ISOTROPIC LEVEL AT -3.517 DB

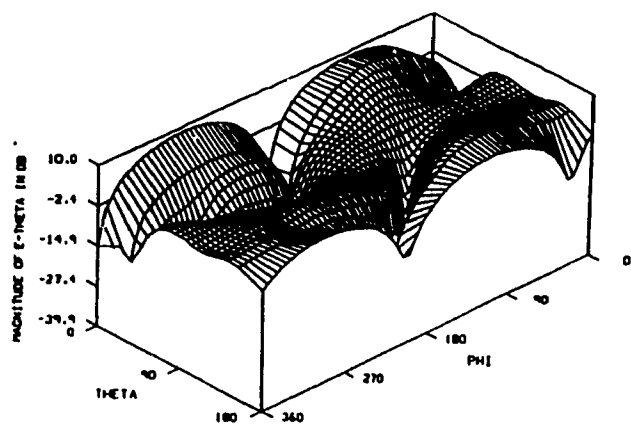
02-JUN-89
HR1400.063



C130 HERCULES MEV. 41
2 X RADII ON VINC. STABILIZERS
EXCITATION - HF3

MAGNITUDE OF e -PHI
CALCULATED AT 3,517 HZ
ISOTROPIC LEVEL AT -3.517 DB

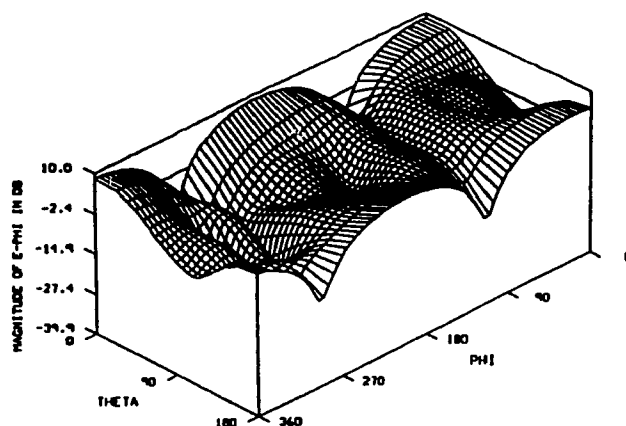
02-JUN-89
HR1400.063



C130 HERCULES MEV. 41
2 X RADII ON VINC. STABILIZERS
EXCITATION - HF4

MAGNITUDE OF e -THETA
CALCULATED AT 12,640 HZ
ISOTROPIC LEVEL AT -12.640 DB

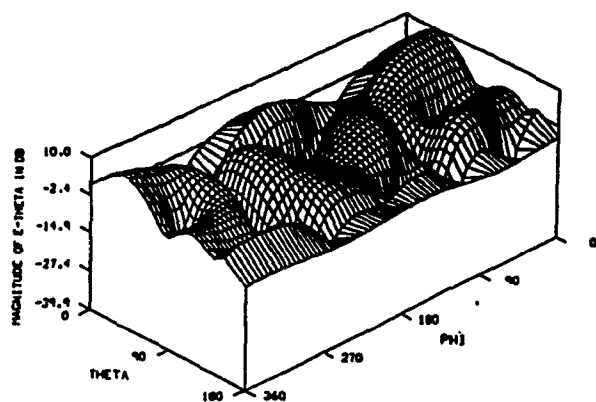
02-JUN-89
HR1400.064



C130 HERCULES MEV. 41
2 X RADII ON VINC. STABILIZERS
EXCITATION - HF4

MAGNITUDE OF e -PHI
CALCULATED AT 12,640 HZ
ISOTROPIC LEVEL AT -12.640 DB

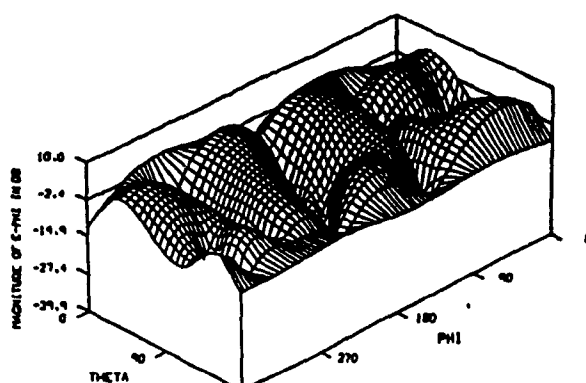
02-JUN-89
HR1400.064



C130 HERCULES MEV. #1
2 H HOLE IN WIND STABILIZER
EXCITATION - W/1

MAGNITUDE OF E-THETA
CALCULATED AT 17,000 RHE
ISOTHERMIC LEVEL AT -12.47% DB

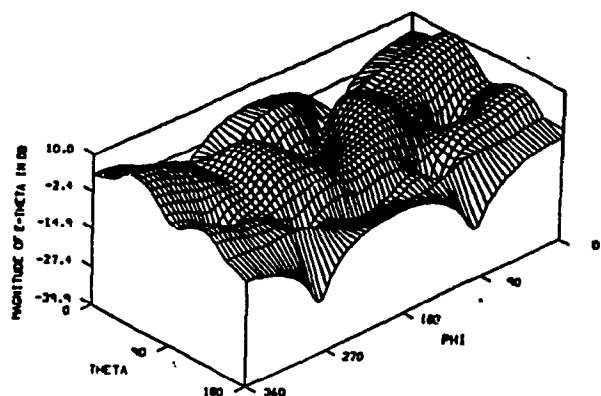
02-JAN-04
H01700,041



C130 HERCULES MEV. #1
2 H HOLE IN WIND STABILIZER
EXCITATION - W/1

MAGNITUDE OF E-PHI
CALCULATED AT 17,000 RHE
ISOTHERMIC LEVEL AT -12.47% DB

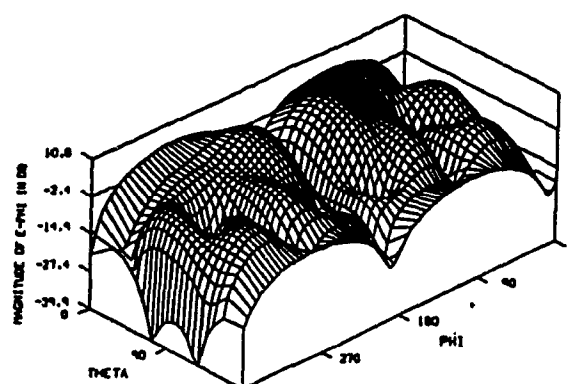
02-JAN-04
H01700,041



C130 HERCULES MEV. #1
2 H HOLE IN WIND STABILIZER
EXCITATION - W/2

MAGNITUDE OF E-THETA
CALCULATED AT 17,000 RHE
ISOTHERMIC LEVEL AT -11.067 DB

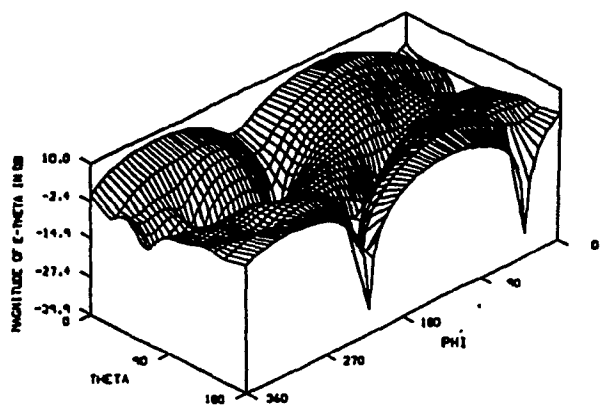
02-JAN-04
H01700,043



C130 HERCULES MEV. #1
2 H HOLE IN WIND STABILIZER
EXCITATION - W/2

MAGNITUDE OF E-PHI
CALCULATED AT 17,000 RHE
ISOTHERMIC LEVEL AT -11.067 DB

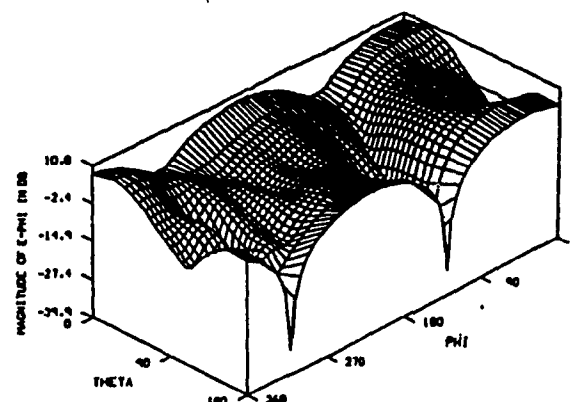
02-JAN-04
H01700,043



C130 HERCULES MEV. #1
2 H HOLE IN WIND STABILIZER
EXCITATION - W/3

MAGNITUDE OF E-THETA
CALCULATED AT 17,000 RHE
ISOTHERMIC LEVEL AT -6.1% DB

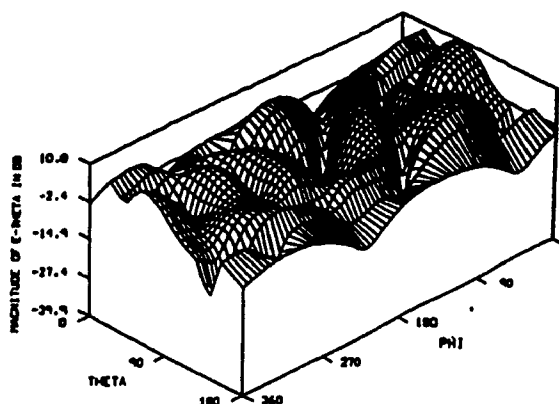
02-JAN-04
H01700,044



C130 HERCULES MEV. #1
2 H HOLE IN WIND STABILIZER
EXCITATION - W/3

MAGNITUDE OF E-PHI
CALCULATED AT 17,000 RHE
ISOTHERMIC LEVEL AT -6.1% DB

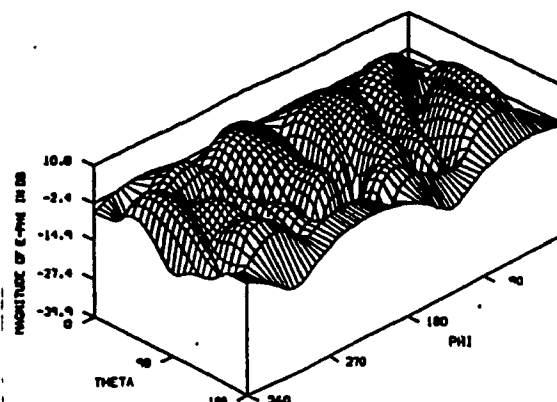
02-JAN-04
H01700,044



C130 HERCULES MEV, 61
2 x HADIS ON VIBRO-STABILIZERS
EXCITATION = HF1

MAGNITUDE OF C-THETA
CALCULATED AT 20,000 PNE
ISOBARIC LEVEL AT -17.504 DB

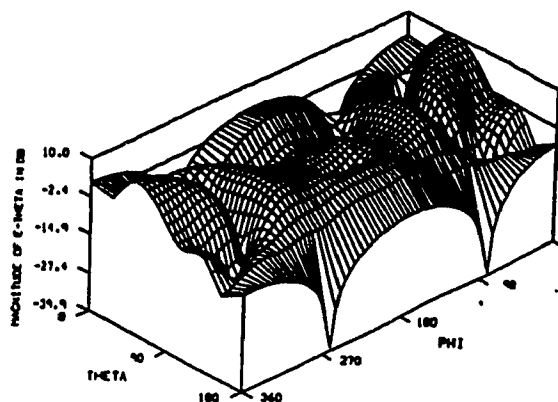
02 JUN 09
NR2000.041



C130 HERCULES MEV, 61
2 x HADIS ON VIBRO-STABILIZERS
EXCITATION = HF1

MAGNITUDE OF C-PHI
CALCULATED AT 20,000 PNE
ISOBARIC LEVEL AT -17.504 DB

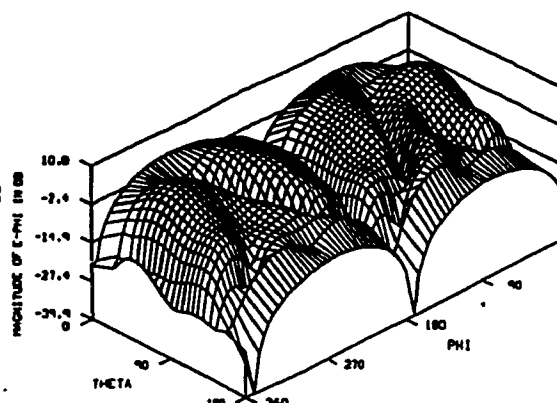
02 JUN 09
NR2000.041



C130 HERCULES MEV, 61
2 x HADIS ON VIBRO-STABILIZERS
EXCITATION = HF2

MAGNITUDE OF C-THETA
CALCULATED AT 20,000 PNE
ISOBARIC LEVEL AT -22.406 DB

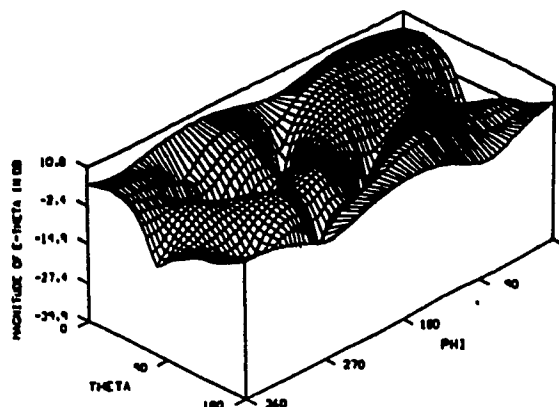
02 JUN 09
NR2000.043



C130 HERCULES MEV, 61
2 x HADIS ON VIBRO-STABILIZERS
EXCITATION = HF2

MAGNITUDE OF C-PHI
CALCULATED AT 20,000 PNE
ISOBARIC LEVEL AT -22.406 DB

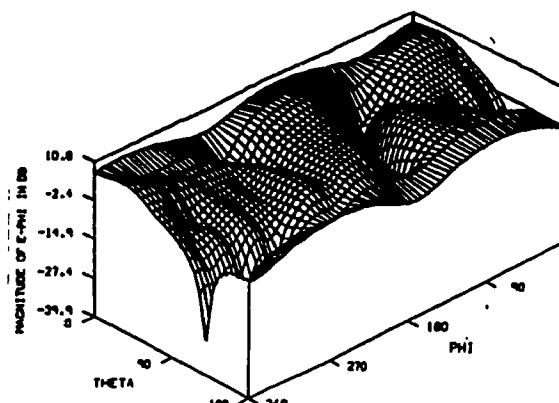
02 JUN 09
NR2000.043



C130 HERCULES MEV, 61
2 x HADIS ON VIBRO-STABILIZERS
EXCITATION = HF4

MAGNITUDE OF C-THETA
CALCULATED AT 20,000 PNE
ISOBARIC LEVEL AT -12.342 DB

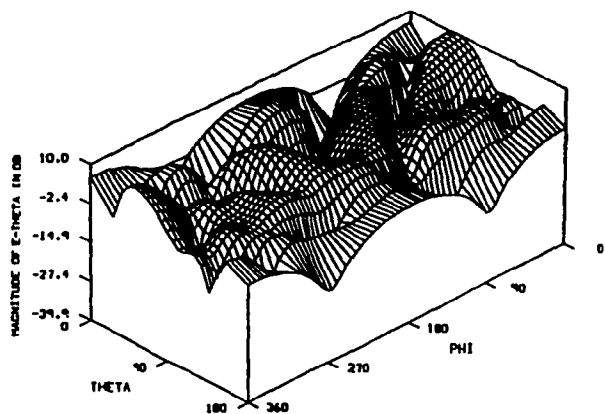
02 JUN 09
NR2000.044



C130 HERCULES MEV, 61
2 x HADIS ON VIBRO-STABILIZERS
EXCITATION = HF4

MAGNITUDE OF C-PHI
CALCULATED AT 20,000 PNE
ISOBARIC LEVEL AT -12.342 DB

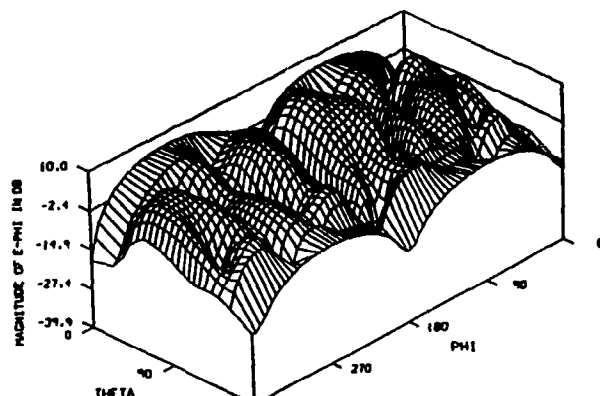
02 JUN 09
NR2000.044



C130 HERCULES (REV. K1)
2 X RADII ON VINC. STABILIZERS
EXCITATION - HP1

MAGNITUDE OF E-THETA
CALCULATED AT 23,000 MHz
ISOTHERMIC LEVEL AT -16.827 dB

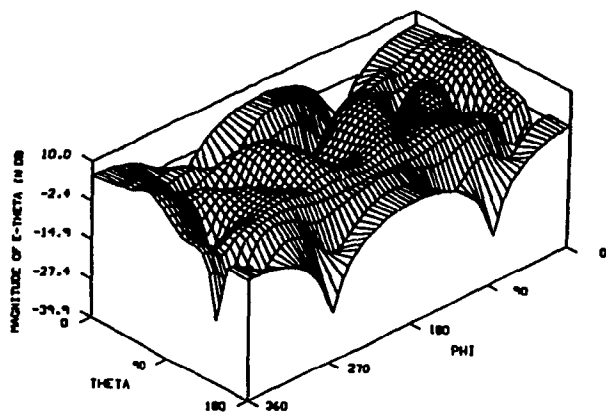
02-JUN-09
HR2300.041



C130 HERCULES (REV. K1)
2 X RADII ON VINC. STABILIZERS
EXCITATION - HP1

MAGNITUDE OF E-PHI
CALCULATED AT 23,000 MHz
ISOTHERMIC LEVEL AT -16.827 dB

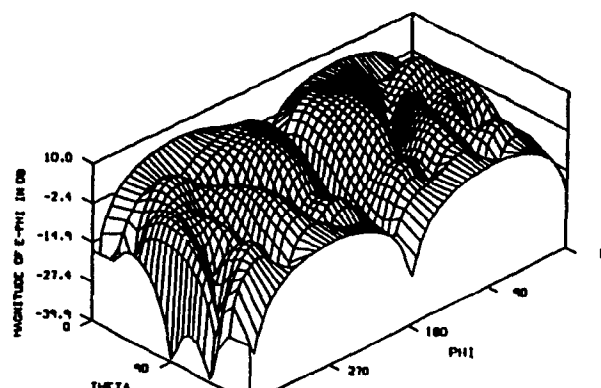
02-JUN-09
HR2300.041



C130 HERCULES (REV. K1)
2 X RADII ON VINC. STABILIZERS
EXCITATION - HP2

MAGNITUDE OF E-THETA
CALCULATED AT 23,000 MHz
ISOTHERMIC LEVEL AT -9.474 dB

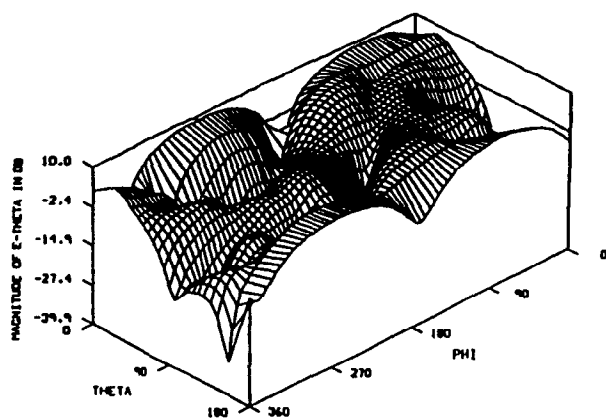
02-JUN-09
HR2300.043



C130 HERCULES (REV. K1)
2 X RADII ON VINC. STABILIZERS
EXCITATION - HP2

MAGNITUDE OF E-PHI
CALCULATED AT 23,000 MHz
ISOTHERMIC LEVEL AT -9.474 dB

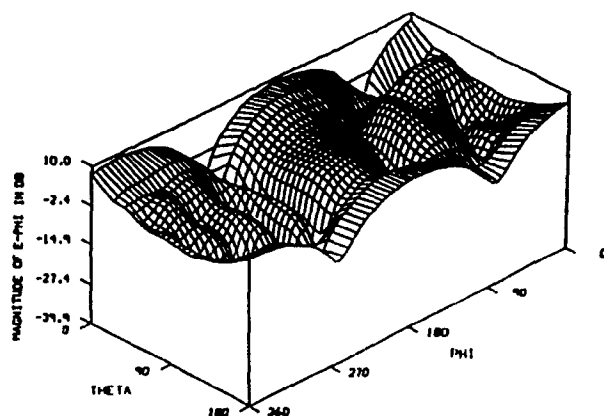
02-JUN-09
HR2300.043



C130 HERCULES (REV. K1)
2 X RADII ON VINC. STABILIZERS
EXCITATION - HP4

MAGNITUDE OF E-THETA
CALCULATED AT 23,000 MHz
ISOTHERMIC LEVEL AT -14.471 dB

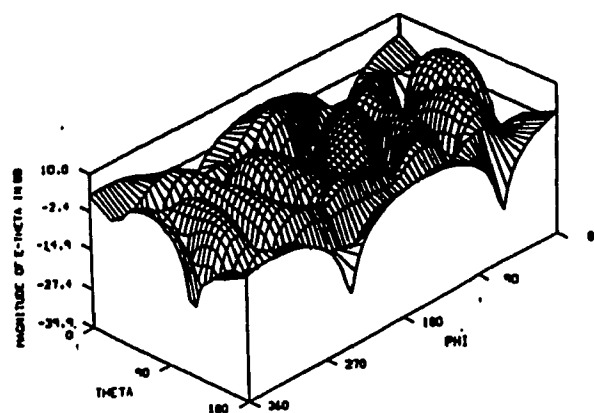
02-JUN-09
HR2300.044



C130 HERCULES (REV. K1)
2 X RADII ON VINC. STABILIZERS
EXCITATION - HP4

MAGNITUDE OF E-PHI
CALCULATED AT 23,000 MHz
ISOTHERMIC LEVEL AT -14.471 dB

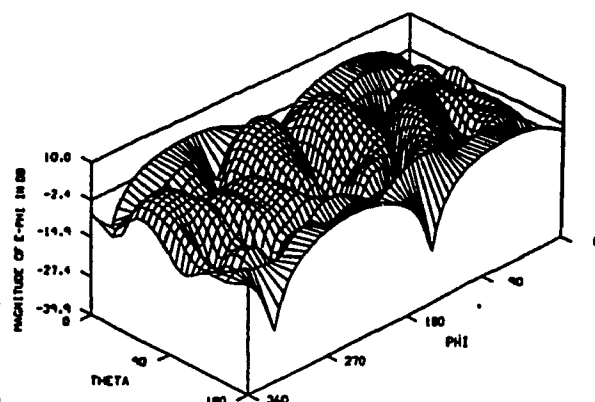
02-JUN-09
HR2300.044



C120 PERCELES MEV. 41
2 H RADII ON VINC. STABILIZING
EXCITATION = 0.1

MAGNITUDE OF E-THETA
CALCULATED AT 25,000 MHz
ISOTHERMIC LEVEL AT -12.101 dB

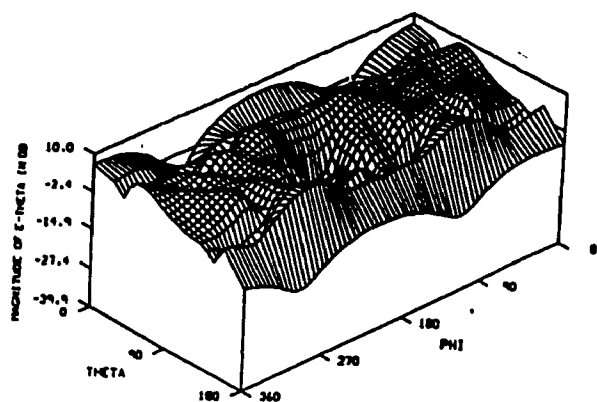
02-JUN-01
102600.001



C120 PERCELES MEV. 41
2 H RADII ON VINC. STABILIZING
EXCITATION = 0.1

MAGNITUDE OF E-PHI
CALCULATED AT 25,000 MHz
ISOTHERMIC LEVEL AT -12.101 dB

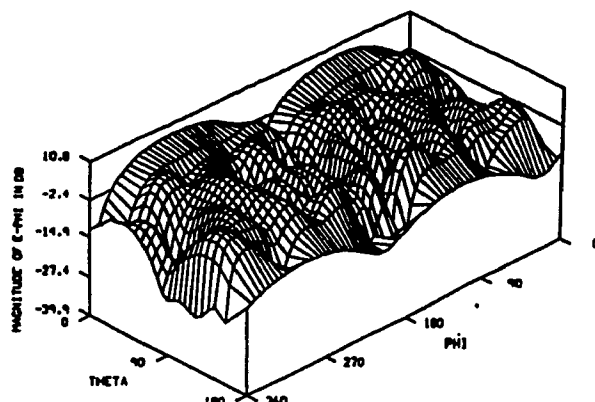
02-JUN-01
102600.001



C120 PERCELES MEV. 41
2 H RADII ON VINC. STABILIZING
EXCITATION = 0.2

MAGNITUDE OF E-THETA
CALCULATED AT 25,000 MHz
ISOTHERMIC LEVEL AT -16.033 dB

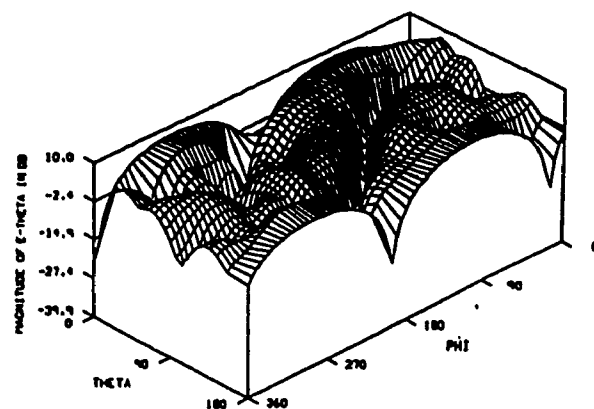
02-JUN-01
102600.002



C120 PERCELES MEV. 41
2 H RADII ON VINC. STABILIZING
EXCITATION = 0.2

MAGNITUDE OF E-PHI
CALCULATED AT 25,000 MHz
ISOTHERMIC LEVEL AT -16.033 dB

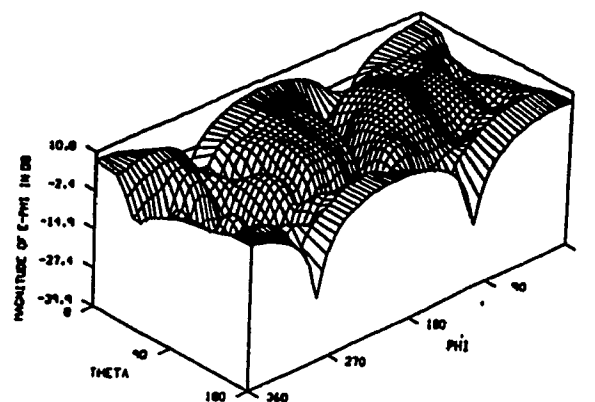
02-JUN-01
102600.002



C120 PERCELES MEV. 41
2 H RADII ON VINC. STABILIZING
EXCITATION = 0.4

MAGNITUDE OF E-THETA
CALCULATED AT 25,000 MHz
ISOTHERMIC LEVEL AT -0.246 dB

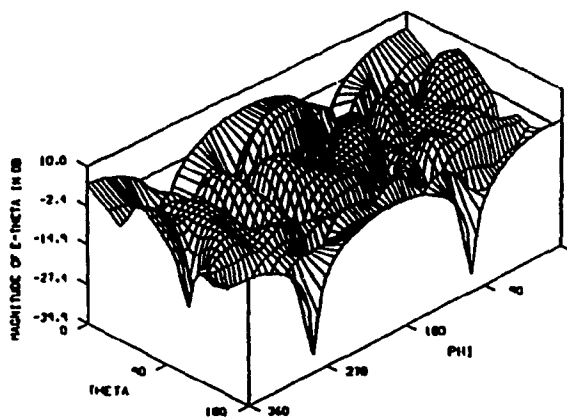
02-JUN-01
102600.004



C120 PERCELES MEV. 41
2 H RADII ON VINC. STABILIZING
EXCITATION = 0.4

MAGNITUDE OF E-PHI
CALCULATED AT 25,000 MHz
ISOTHERMIC LEVEL AT -0.246 dB

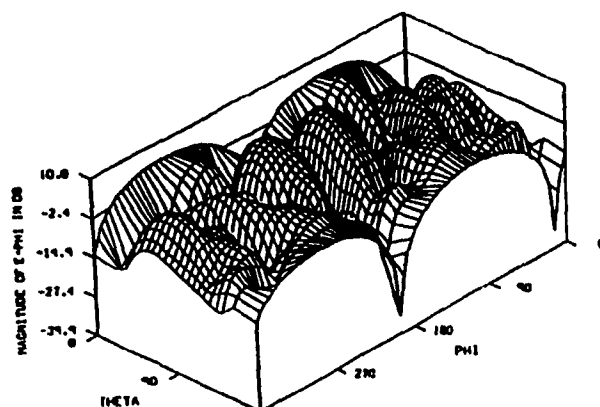
02-JUN-01
102600.004



C130 HERCULES VIEW, #1
2 H RADI ON WINGS STABILIZERS
EXCITATION - #1

MAGNITUDE OF E-THETA
CALCULATED AT 30,000 PNE
ISOTHERMIC LEVEL AT -10.043 DB

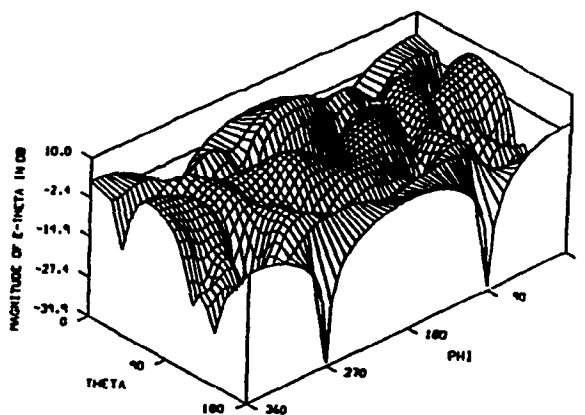
02-JUN-89
H02000,041



C130 HERCULES VIEW, #1
2 H RADI ON WINGS STABILIZERS
EXCITATION - #1

MAGNITUDE OF E-PHI
CALCULATED AT 30,000 PNE
ISOTHERMIC LEVEL AT -10.043 DB

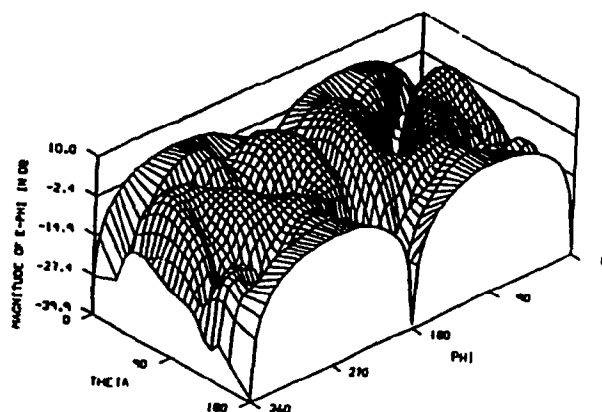
02-JUN-89
H02000,041



C130 HERCULES VIEW, #1
2 H RADI ON WINGS STABILIZERS
EXCITATION - #2

MAGNITUDE OF E-THETA
CALCULATED AT 30,000 PNE
ISOTHERMIC LEVEL AT -10.202 DB

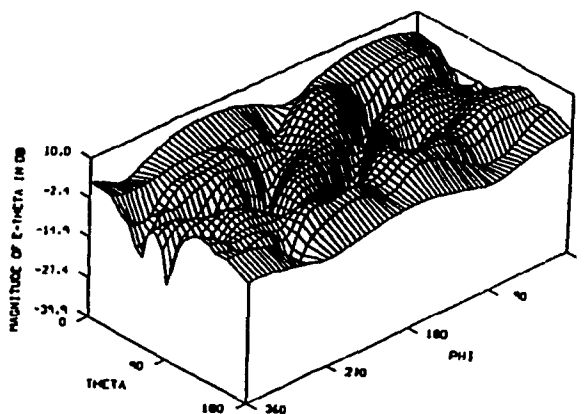
02-JUN-89
H02000,042



C130 HERCULES VIEW, #1
2 H RADI ON WINGS STABILIZERS
EXCITATION - #2

MAGNITUDE OF E-PHI
CALCULATED AT 30,000 PNE
ISOTHERMIC LEVEL AT -10.202 DB

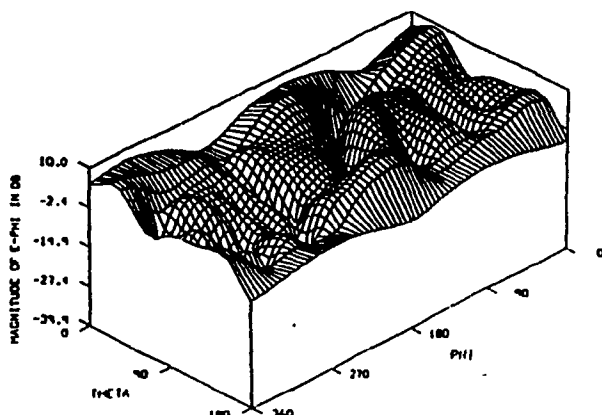
02-JUN-89
H02000,042



C130 HERCULES VIEW, #1
2 H RADI ON WINGS STABILIZERS
EXCITATION - #4

MAGNITUDE OF E-THETA
CALCULATED AT 30,000 PNE
ISOTHERMIC LEVEL AT -0.654 DB

02-JUN-89
H02000,044



C130 HERCULES VIEW, #1
2 H RADI ON WINGS STABILIZERS
EXCITATION - #4

MAGNITUDE OF E-PHI
CALCULATED AT 30,000 PNE
ISOTHERMIC LEVEL AT -0.654 DB

02-JUN-89
H02000,044

LIST OF REFERENCES

- ATLAS Antenna Testing Laboratory
Automated System... The Link to
Better Performance, Naval Air
Test Center SY-81.
- AN/ARC-132 HF Liaison Communication and HF
and VLF/LF Antenna Subsystems,
NAVAIR 01-75GAE-2-8.
- MIL-A-9080 Antennas, Liaison Communications
Equipment, General Specification
for Design of, February 1954.
- NATC Tacamo EC-130 Scale Model HF
Antenna Evaluation. Report No.
SY-11R-84.
- BAHSOUN, Y. Evaluation of an HF Helicopter
Antenna Measurements and
Numerical Techniques. Master's
Thesis, Faculty of Engineering,
Concordia University, March 1982.
- BALANIS, C.A. Advanced Engineering
Electromagnetics. John Wiley and
Sons, New York, 1989.
- BLAKE, L.V. Antennas. Artech House Inc.,
1984.
- BURKE, G.J. and POGGIO, A.J. Numerical
Electromagnetic Code (NEC).
Technical Document 116, Naval
Ocean Systems Center, San Diego,
California, January 1981.
- CARSWELL, I. Current Distribution on Wing-Cap
and Tail-Cap IRE Transactions -
Antennas and Propagation, October
1955, pp.207-214.
- GRANGER, J.V.N. Aircraft Antennas. Proceedings of
the IRE, May 1955, pp.533-549.
- GRANGER, J.V.N. Radio-Frequency Current
Distributions on Aircraft
Structures. Proceedings of the
I.R.E., August 1951, pp.932-938.

- HALLER, G.L. Aircraft Antennas. Proceedings of the I.R.E., August 1942, pp.357-364.
- HARRINGTON, R. F. Field Computation by Moment Methods. The MacMillan Co. New York, 1968.
- HWU, S. and WILTON, D.R. EM Scattering and Radiation by Arbitrary Configuration of Conducting Bodies and Wires, Junction Code, Technical Report Number 87-17, May, 1980.
- JASIK, H. Antenna Engineering Handbook, McGraw Hill Company, New York, 1961.
- KUBINA, S.J. Study of Electromagnetic Analysis Techniques for Aircraft Antennas. Technical Note No. TN-EMC-85-02, Final Report, December 1984.
- KUBINA, S.J. and ROSENZWEIG, B.R. EC-130 HF Antenna Analysis Final Report. Report No. TN-EMC-90-02, April 1990.
- LAROSE, C.L. Advances in Wire-Grid Modelling of Antennas and Auxiliary Computer Graphics Systems with the CP-140 Case Study. Master's Thesis, Faculty of Engineering, Concordia University, July 1986.
- LEE, K.S.H. and MARIN L. Limitations of Wire-Grid Modeling of a Closed Surface. IEEE Transactions on Electromagnetic Compatibility, August 1976, pp.123-129.
- LUDWIG, A.C. Wire Grid Modelling of Surfaces. IEEE Transactions on Antennas and Propagation, September 1987, pp.1045-1048.
- MILLER, E.K. and BURKE G.J. Accuracy-Modeling Guidelines for Integral -Equation Evaluation of Thin-Wire Scattering Structures. IEEE Transactions on Antennas and

- Propagation, July 1971, pp.534-536.
- MILLER, E.K. A Selective Survey of Computational Electromagnetics. IEEE Transactions on Antennas and Propagation, September 1988, pp.1281-1304.
- MITTRA R. Computer Techniques for Electromagnetics. New York, Pergamon, 1973.
- MOORE, J. and PIZER, R. Moment Methods in Electromagnetics. Research Studies Press, England 1984.
- MOORE, E.J. Performance Evaluation of HF Aircraft Antenna Systems. IRE Transactions on Antennas and Propagation, July 1958, pp.254-260.
- NEY, M.M. Method of Moments as Applied to Electromagnetic Problems. IEEE Transactions on Microwave Theory and Techniques, October 1985, pp.972-980.
- Paul, C.R. and NASAR, S.A. Introduction to Electromagnetic Fields. McGraw Hill, 1982.
- RAUTIO, J.C. Reflection Coefficient Analysis of the Effect of Ground Antenna Patterns. IEEE Antennas and Propagation Society Newsletter, February 1987, pp.3-11.
- RICHMOND, J.H. A Wire-Grid Model for Scattering by Conducting Bodies. IEEE Transactions on Antennas and Propagation, November 1966, pp.782-789.
- SESHADRI, S.R. Fundamentals of Transmission Lines and Electromagnetic Fields. Addison-Wesley Publishing Company, Massachusetts, 1971.

- SHARP, E.D. and TANNER R.L.. Scale Modeling of High-Frequency Antennas. IEEE Transactions on Antennas and Propagation, November 1969, pp.810-811.
- SINCLAIR, G. and JORDAN, E.C. Measurement of Aircraft-Antenna Using Models. Proceedings of the I.R.E., December 1947, pp.1451-1462.
- SINCLAIR, G. Theory of Models of Electromagnetic Systems. Proceedings of the I.R.E., November 1948, pp.1364-1370.
- STUTZMAN, W.L. and THIELE, G.A. Antenna Theory and Design. John Wiley and Sons, New York, 1981.
- TANNER, R. L. and ANDREASEN M.G. Numerical Solution of Electromagnetic Problems. IEEE Spectrum, September 1967, pp.53-61.
- TRUEMAN, C.W. Average Field Matching Wire Antenna Moment Method and Aircraft HF Antenna Application. Doctoral Thesis, McGill University, April 1979.
- WILTON, D.R. and BUTLER C.M. Efficient Numerical Techniques for Solving Pocklington's Equation and Their Relationships to Other Methods. IEEE Transactions on Antennas and Propagation, January 1976, pp.83-86.
- WILTON, D.R. and BUTLER C.M. Analysis of Various Numerical Techniques Applied to Thin-Wire Scatterers. IEEE Transactions on Antennas and Propagation, July 1975. pp.534-540.
- WU, T.T. and KING W.P. The Tapered Antenna and Its Application to the Junction Problem for Thin Wires. IEEE Transactions on Antennas and Propagation, January 1976, pp.42-45.